

**Few-cycle microscopy  
of a laser wakefield accelerator**

**Alexander Sävert**

**Dissertation  
zur Erlangung des akademischen Grades  
doctor rerum naturalium (Dr. rer. nat.)**



---

seit 1558

vorgelegt dem Rat der  
Physikalisch-Astronomischen Fakultät  
der Friedrich-Schiller-Universität Jena

eingereicht von Dipl.-Phys. Alexander Sävert  
geboren am 07.09.1981 in Karl-Marx-Stadt

## **Gutachter**

**1. Prof. Dr. Malte C. Kaluza**

Institut für Optik und Quantenelektronik Jena  
Friedrich-Schiller-Universität Jena, Deutschland

**2. Prof. Dr. Stefan Karsch**

Fakultät für Physik  
Ludwigs-Maximilians-Universität München &  
Max-Planck-Institut für Quantenoptik, Deutschland

**3. Prof. Dr. Ulrich Schramm**

Institut für Kern- und Teilchenphysik  
TU Dresden, Deutschland

Tag der öffentlichen Verteidigung: 28.06.2016

*Für meine Familie.*

# Zusammenfassung

Die vorliegende Arbeit beschreibt die Entwicklung und die erste Anwendung einer neuen Diagnostik für einen Laser-Plasma-Beschleuniger. Die Grundlagen der Elektronenbeschleunigung mittels relativistischer Plasmawellen, die von einem hochintensiven Laserpuls angeregt werden sind inzwischen gut bekannt. Darauf aufbauend konnten in den letzten Jahren signifikante Fortschritte bezüglich der Stabilität dieser Beschleuniger hinsichtlich Strahlenergie, Richtungsschwankungen und Ladung erzielt werden. Jedoch unterscheiden sich die Ergebnisse verschiedener Gruppen auf der Welt zum Teil erheblich, obwohl vergleichbare Lasersysteme zum Einsatz kamen. Um ein einheitliches physikalisches Bild zu entwickeln ist ein direkter Einblick in die Beschleunigungsdynamik insbesondere in die Entwicklung der Plasmawelle notwendig. Die kleine räumliche Ausdehnung der Plasmawelle und die sehr kurzen Zeitskalen in der Größenordnung einiger fs haben bisher einen Einblick verwehrt. Der Beschleunigungsvorgang selbst blieb im Dunkeln und konnte nur mit Hilfe aufwändiger Simulationen grob umrissen werden.

In dieser Arbeit wurde ein neuartiges Verfahren zur Untersuchung von Plasmabeschleunigern namens „Einzelzyklenmikroskopie“, (engl. Few-Cycle Microscopy, FCM) entwickelt und zum ersten Mal angewendet. Bei dieser Diagnostik wird ein hochauflösendes optisches Abbildungssystem mit einer ultrakurzen Lichtquelle kombiniert um die Wechselwirkung zwischen dem hoch-intensiven Laserpuls und dem Plasma zu untersuchen. Zur Erzeugung der Probepulse wurde ein kleiner Teil des Pumpstrahls abgetrennt und in einer mit Argon gefüllten Hohlleiter spektral verbreitert. Danach wurden die Pulse mit Hilfe von gechirpten Spiegeln zu einer Pulsdauer von nur zwei optischen Zyklen komprimiert. FCM hat dadurch einen einzigartigen Blick auf die Laser-Plasma-Wechselwirkung ermöglicht. Es konnten hochauflösende Bilder der Plasmawelle in Echtzeit aufgenommen werden. Wesentliche Stufen in der Entwicklung der Plasmawelle, wie z.B. deren Entstehung, das Brechen der Welle und schließlich die Beschleunigung von Elektronen konnten sowohl im Experiment, wie auch in Simulationen beobachtet werden. Die experimentellen Ergebnisse haben gezeigt, dass es notwendig ist den Probestrahl sowie das optische Abbildungssystem in den Simulationen zu berücksichtigen um die Detailfülle in den Schattenbildern zu reproduzieren. Mit Hilfe dieser Diagnostik konnte die Expansion der ersten Plasmawellenperiode, der sogenannten *bubble*, in Zusammenhang mit der Injektion von Elektronen gebracht werden. Damit war erstmalig ein direkter, quantitativer Vergleich zwischen Theorie und Simulation sowie den experimentellen Ergebnissen möglich.

Weiterhin konnte ein neues Beschleunigungsregime unter Verwendung von Wasserstoffgas mit Hilfe der kombinierten Ergebnisse aus FCM Schattenbildern, Interferogrammen und spektral aufgelöster, rückgestreuter Laserstrahlung entdeckt und beschrieben wer-



den. In diesem Regime findet zuerst eine Aufheizung des Plasmas statt, welches die Ausbildung der Plasmawelle unterdrückt. In der zweiten Phase findet die eigentliche Beschleunigung der Elektronen aus dem heißen Hintergrundplasma in der Plasmawelle statt. Dieser zweistufige Mechanismus in Wasserstoff erzeugt Elektronenpulse mit einer höheren Ladung, niedrigeren Divergenz und einer besseren Richtungsstabilität als unter Verwendung von Heliumgas. Das Aufheizen konnte dabei auf die stimulierte Ramanrückwärtsstreuung zurückgeführt werden, welche bisher bei den verwendeten kurzen Laserpulsen ( $\tau_L = 30$  fs) als vernachlässigbar angesehen wurde. Wie jedoch in dieser Arbeit gezeigt werden konnte, bietet das Zusammenspiel des zeitlichen Intensitätskontrastes des Laserpulses 1 ps vor der Spitzenintensität mit einer hinreichend hohen Elektronendichte gute Bedingungen für das Anwachsen dieser Instabilität. Jene ist maßgeblich an der Verbesserung der Elektronenstrahleigenschaften beteiligt.

Die Vielseitigkeit der hier vorgestellten Diagnostik und deren einfache Integration in existierende Hochleistungslasersysteme bietet die Möglichkeit nicht nur lasererzeugte Plasmawellen zu beobachten, sondern auch Elektronenstrahl- und Plasmainstabilitäten. Diese sind insbesondere für die momentan im Aufbau befindlichen elektronenstrahlgetriebenen Plasmabeschleuniger von großem Interesse.

# Abstract

This thesis describes the development and first application of a novel diagnostic for a laser driven wakefield accelerator. The fundamental physics underlying the acceleration of electrons in a relativistic plasma wave excited during the interaction of a high-intensity laser pulse with a plasma is well understood. On this basis, significant progress towards improving the stability of such an accelerator in terms of beam energy, pointing fluctuations and charge has been made during the last decade. However, the results from laboratories around the world still differ quite substantially even though comparable laser systems were used. To develop a comprehensive and detailed physical picture, a direct experimental insight into the acceleration dynamics, in particular the evolution of the plasma wave, would be beneficial. The miniscule spatial dimensions of the plasma wave and ultrashort time scales on the order of a few fs have so far defied a direct observation and the accelerator has remained a black box with rough contours drawn by extensive numerical simulations.

In this thesis, a novel probing diagnostic tool termed Few-Cycle Microscopy (FCM) has been developed and applied for the first time. The diagnostic essentially consists of two parts. The first part is a high-resolution imaging system and the second is an ultrashort light source illuminating the interaction region. To generate these probe pulses, a small part of the pump pulse was split off, spectrally broadened in an argon filled hollow core fiber and temporally compressed by a set of dispersion compensating mirrors down to a duration of two optical cycles. Using FCM has opened a pristine view into the laser-plasma interaction and has allowed the recording of high-resolution images of the plasma wave in real time. Important stages during the wave's evolution such as its formation, its breaking and finally the acceleration of electrons in the associated wake fields were observed in the experiment as well as in simulations. For the latter it was found that it is necessary to include the probe pulses as well as the imaging system into the simulation to reproduce all details of the experimentally recorded shadowgrams. Using this diagnostic, the expansion of the wave's first period, the so-called 'bubble', was identified to be crucial for the injection of electrons into the wave allowing for the first time a quantitative comparison between analytical and numerical models and experimental results.

Furthermore, the shadowgrams taken with FCM in combination with interferograms and backscatter spectra have revealed a new acceleration regime when using hydrogen as the target gas. Here, in the first stage, the plasma is pre-heated, initially suppressing the formation of the plasma wave. In the second stage, the plasma wave is formed and the main acceleration starts. It was found that in this scheme electron pulses are generated with a higher charge, lower divergence and better pointing stability than with helium gas. The underlying pre-heating process could be attributed to stimulated Raman scattering, which

has been thought to be negligible for short ( $\tau_L = 30$  fs) laser pulses. However, as it is shown in this thesis the interplay of the temporal intensity contrast of the laser pulse 1 ps before the peak of the pulse together with a sufficiently high plasma electron density can provide suitable conditions for this instability to grow, resulting in improved electron pulse parameters.

The versatility of FCM and its straightforward implementation into existing high power laser systems will pave the way to not only observe the formation of the plasma wave induced by the laser pulse but to visualize electron beam and plasma instabilities alike, which are also relevant for the upcoming generation of high-energy beam driven plasma accelerators.

# Contents

Contents .....	v
1. Introduction.....	1
2. Theory of high intensity laser-plasma interactions.....	6
2.1 Ionization mechanisms.....	6
2.2 Electron motion in an electromagnetic field.....	8
2.3 Ponderomotive force.....	11
2.4 Laser propagation in underdense plasmas/ nonlinear relativistic optics .....	11
2.5 Nonlinear relativistic optics.....	13
2.6 Temporal compression and photon acceleration .....	15
2.7 Laser plasma instabilities.....	15
2.7.1 Stimulated Raman scattering .....	16
2.7.2 Filamentation .....	18
2.8 Plasma waves and acceleration.....	18
2.8.1 Plasma wave generation .....	18
2.9 Plasma wave phase velocity .....	20
2.10 Maximum achievable electric field and wave breaking .....	20
2.11 Laser wakefield acceleration .....	23
2.11.1 Self-modulated laser wakefield acceleration .....	23
2.11.2 Blowout regime .....	24
2.12 Acceleration limits .....	26
2.13 Scaling laws and matching conditions.....	28
2.13.1 Gordienko Pukhov (GP) scaling .....	29
2.13.2 Lu scaling .....	30
2.14 Electron trapping and injection.....	31
2.14.1 Self-injection and wave breaking .....	32
3. Experimental setup .....	34
3.1 Experimental setup.....	35
3.2 Supersonic gas jet targets.....	36
3.3 Electron beam diagnostics.....	38
3.4 Comparison of plasma imaging techniques .....	39
3.4.1 Interferometry.....	40
3.4.2 Shadowgraphy .....	41

3.5	Probing Laser-Wake-Field-Acceleration at the JETi40.....	42
3.5.1	High energy probe beam line and imaging system .....	42
3.5.2	Few-cycle optical probe beam line and high-resolution imaging .....	44
4.	Laser wakefield acceleration in helium .....	46
4.1	Experimental setup and probing diagnostics .....	46
4.2	Shadowgraphy with few-cycle probe pulses.....	47
4.2.1	Influence of the pump pulse on the plasma wavelength .....	50
4.2.2	Comments on beamloading .....	51
4.3	Measurement of the plasma wavelength and the self-injection threshold.....	51
4.4	Temporal evolution of the plasma wave in the self-injection regime .....	57
4.4.1	Wave breaking radiation .....	60
4.5	Evolution of the first and second oscillation periods .....	61
4.6	Transverse wave breaking and transition to the bubble regime .....	66
4.7	Analysis of the wavefront curvature of the plasma wave.....	67
4.8	3-D PIC simulation including a few-cycle probe pulse.....	69
4.8.1	Formation of the shadowgrams .....	71
4.8.2	Temporal evolution of the plasma wave - bubble expansion .....	74
5.	Dynamics of the target gas in a LWFA.....	77
5.1	Experimental setup.....	77
5.2	Laser wakefield acceleration with helium, hydrogen and deuterium.....	79
5.2.1	Results with high contrast laser pulses .....	79
5.2.2	Results with low contrast laser pulses .....	81
5.2.3	Results from interferometry.....	83
5.3	Backscattered spectra for helium and hydrogen .....	86
5.4	Time-resolved shadowgraphy with helium and hydrogen.....	90
5.5	Stimulated Raman scattering as efficient pre-acceleration and injection mechanism..	92
6.	Conclusion and future applications.....	94
6.1	Complete temporal evolution of the plasma wave in a single shot.....	95
6.2	Extension of ultrafast shadowgraphy to longer wavelengths .....	97
	Bibliography.....	99
	Appendix A .....	115
	Appendix B.....	116
	Appendix C.....	117

# 1. Introduction

Particle accelerators are a cornerstone of modern society. Using the accelerated particles themselves or as a source for secondary radiation, advances in biology, chemistry, material science and physics have been achieved, and with numerous Nobel prizes appreciated [1]. Particle accelerators are built in two distinct geometries, linear and circular. Both designs use radio-frequency (rf) waves in the acceleration cavities to generate alternating fields to accelerate the charged particles. The field strength is thereby limited by the damage threshold of the cavity wall material, e.g., copper, to 10-100 MV/m, and thus the size of the accelerator depends on the desired particle energies. The biggest accelerators are the Large Hadron Collider (LHC) at CERN [2] and the Stanford Linear Accelerator at SLAC [3]. The LHC has a circumference of 27 km and has accelerated proton bunches to energies of 6.5 TeV in each of the counter propagating beams. Discoveries like the Higgs Boson [4, 5] as the last puzzle piece to complete the standard model of physics is one example of the rewards for this effort. The Stanford Linear Accelerator was already built in the 1960s, capable of producing electron and positron beams up to 50 GeV in a 3 km long tunnel. The accelerator was decommissioned, but today houses the Facility for Advanced Accelerator Experimental Tests (FACET) and the Linear Coherent Light Source (LCLS), a 4<sup>th</sup> generation light source offering brilliant x-ray pulses. The next stage for an electron-positron collider is the International Linear Collider (ILC) with a collision energy of 500 GeV [6]. The required accelerator is 35 km in length and the approximate cost of \$20 billion marks the upper limit for what is economically realizable. The main reason for the necessary huge size of these accelerators and the related cost is linked to the maximum achievable acceleration field due to breakdown of the cavity material. Advanced cavity designs based on dielectrics using sapphire instead of metals would allow scientists to reach an even higher field of up to 250 MV/m [7] but so far only lengths on the mm scale have been realized and scalability remains to be seen. In addition, the required wavelength change from radio frequencies to the near infrared to generate the electric fields in the accelerator cavities would require a new class of high power, high repetition rate lasers.

An alternative to rf-accelerators are plasma based accelerators. They do not experience the same drawbacks in terms of material breakdown since all matter is already broken down in the plasma state and huge electric fields can be generated by the separation of the charged constituents (electrons and ions) [8]. At an electron density of  $n_e = 1 \cdot 10^{18} \text{ cm}^{-3}$ , plasmas can support electric fields on the order of 100 GV/m. This is typically 3 to 4 orders of magnitude higher than the field achievable in rf-accelerators. Thus, using a

plasma would allow the miniaturization of particle accelerators and the associated reduction in construction costs could provide more access to a broader scientific community as well as the possibility of generating even higher particle energies.

In the 1970s, Tajima and Dawson proposed an acceleration scheme called the *Plasma Wakefield Accelerator*. In this scheme, a periodic density fluctuation or plasma wave is created in the wake of either an ultra relativistic electron bunch or a high-intensity laser pulse reaching over  $10^{18}$  W/cm<sup>2</sup> propagating through a plasma. Since the plasma wave is co-moving with the exciting pulse, a high energy gain can be achieved in a single stage. At that time, high-power laser development was still in its infancy and so the first tests of this scheme were performed using relativistic electron bunches from conventional accelerators in 1988 [9]. In the last couple of years, particle driven wakefield acceleration has reached some impressive milestones, e.g., the energy doubling of a 42 GeV electron bunch in a less than 1 meter long lithium vapor chamber. Quite recently, the generation of high quality electron [10] and positron beams [11] with energies above 20 GeV was achieved both marking important steps towards a plasma based TeV positron-electron collider [12]. In the near future, 400 GeV proton bunches at CERN will be used to drive wakefields [13], which should be able to accelerate electrons to even higher energies. In the preferred driver-witness scheme, the maximum energy,  $E_{wit}$ , a particle in the witness bunch can receive is limited by the transformer ratio  $E_{wit}/E_{driv} \leq 2$  [14], hence, making it favorable to use proton pulses instead of electron pulses as a driver. Similar to the successes of particle driven plasma accelerators, the development of intense laser pulses required for laser-driven particle acceleration has made considerable progress.

The era of relativistic optics began nearly 30 years ago with the advent of short pulse high power laser systems. The invention of Chirped Pulse Amplification (CPA) [15] and the development of Ti:sapphire laser systems have opened the path to the generation of high power laser pulses at university research laboratories. When focused to intensities exceeding  $2 \cdot 10^{18}$  W/cm<sup>2</sup> these laser pulses can excite plasma waves. The electrons in the plasma are expelled from regions of high intensity by the ponderomotive force of the laser pulse and a pure ion region is formed around and behind the pulse's path. Attracted by the electrostatic force of the ions, the electrons return to the axis setting up a collective oscillation forming an electron density modulation that co-propagates with the driving pulse, i.e., the plasma wave. This generates a favorable environment for electron acceleration since the longitudinal field inside the wave is uniform across the transverse dimension and the transverse, focusing force depends linearly on the radius. Highly energetic electron pulses with a narrow energy spread and good collimation are produced routinely in laboratories all over the world [16-19] and the current record in peak energy being 4.2 GeV [19]. A unique feature of these bunches is their short pulse duration, which is on the order of a couple of fs [20, 21], with a charge in the 10s of pC range comparable to state

of the art rf-accelerators in national laboratories [22]. Furthermore, laser wakefield accelerators (LWFA) not only produce high quality electron bunches but are also a source of brilliant x-ray radiation [23]. The basic principles of the laser-plasma interaction are well understood in theory and much empirical knowledge has been gathered over the last few decades. A lot of optimization of LWFA was performed guided by predictions from numerical simulations as they have provided detailed insight into the laser plasma interaction. However, the laser and plasma parameters in an actual experiment are hard to come by since direct experimental observation has so far been restricted due to the small spatial ( $\sim\mu\text{m}$ ) and temporal scale ( $\sim\text{fs}$ ) of a LWFA.

There are two distinct probing geometries to investigate a LWFA with optical laser pulses. The probe pulse can either co-propagate with the driving pulse or traverse the interaction region perpendicularly. In the first geometry, two temporally delayed probe pulses are typically used. The first pulse precedes the driver pulses and acts as a reference that probes the gas jet. The second probe pulse overlaps with the driver pulse. Both pulses are imaged onto a spectrometer and their phase shift is recorded as a spectral interferogram. By changing the delay between the two probe pulses a periodic structure was observed [24]. Temporal stretching of the second pulse allows recording of the time integrated evolution of the LWFA in a single shot with a technique called Fourier Domain Holography (FDH) [25]. For the rapid and dynamic evolution of the plasma wave that occurs in nonlinear wakefield accelerators, the temporal integration and strong refraction of the probe pulse caused by the steep refractive index gradients in the plasma wave itself defines the limits of this technique [26-28]. To take snapshots of a fast evolving object travelling near the speed of light  $c$ , a transverse probing geometry has to be applied. The duration of the probe pulse (or equivalent its bandwidth) should be  $\tau_{\text{pr}} \leq \frac{\lambda_p}{2c}$ , with  $\lambda_p$  being the characteristic size of the object, e.g., the plasma wavelength. A first experiment was performed utilizing shadowgraphy and polarimetry to study the injection process in real time [21]. However, due to plasma parameters matching the optimal acceleration conditions, the temporal and spatial resolution of the shadowgrams was not high enough to visualize the distinct shape of the plasma wave. For these reasons, a transition to lower plasma densities is necessary, which requires much higher laser peak powers [29]. Such laser pulses are commercially available with pulse durations on the order of 25 fs. Nevertheless, such pulses are not sufficiently short for transverse probing. However, spectral broadening in a hollow core fiber filled with a noble gas has proven to generate stable laser pulses of a few optical cycles [30]. This technique is widely used in laser systems with kHz repetition rate, e.g., for studying the influence of the absolute phase on strong-field ionization [31]. However, such pulses have not been synchronized to multi Terawatt laser pulses so far. The availability of such ultrashort probe pulses would allow an unprecedented view into



the formation and the evolution of the plasma wave and greatly assist in the study of the electron acceleration process. Furthermore, unresolved problems like the stability and the scalability of laser driven plasma acceleration could thus be potentially answered.

### **Structure of this thesis**

*The goal of this thesis was to develop and apply a novel diagnostic technique suitable for the investigation of laser wakefield acceleration of electrons using the JETi 40 laser system. JETi 40 is a 30 TW Ti:sapphire laser system delivering pulses of 800 mJ energy and 27 fs duration at a repetition rate of up to 10 Hz, see Appendix A. When focusing these laser pulses into gas jets electron pulses with tens to hundreds of pC charge [32], up to 200 MeV [33] in energy and few fs duration were generated. A novel few-cycle probe pulse was used to investigate and track the evolution of the plasma wave. At the same time, these detailed images could be used to understand the peculiarities when using hydrogen instead of helium as a target gas.*

*The thesis is structured as follows:*

- *Chapter 2: The theory of high intensity laser-plasma interaction is discussed. From the fundamental description of a laser pulse to the excitation of collective electron density oscillations fundamental relations are derived. The acceleration regimes relevant for the experiments in this thesis are introduced.*
- *Chapter 3: The experimental setup is described in detail. In addition, two imaging techniques, shadowgraphy and interferometry are explained and peculiarities discussed. A few-cycle probe beam line at the JETi40 laser system was built during the Master thesis of Matthew B. Schwab [34]. Based on this, the setup of this probing beam line was further optimized within this thesis. The combination of the few-cycle probe pulse with a high-resolution imaging setup was termed Few-Cycle Microscopy (FCM). Using this worldwide unique tool, allowed high-resolution probing of laser-plasma-interactions at relativistic intensities.*
- *Chapter 4: FCM was applied for the first time and a pristine insight into the interaction of a high intensity laser pulse with an underdense plasma was recorded. The dependence of the plasma wavelength on the electron density and the evolution of the laser driven plasma wave during the propagation through the gas jet are shown using FCM. Details on the evolution of the first and second plasma period could be obtained. It was found that the expansion of the first period is caused by the intensity increase of the driving pulse and this expansion is essential for the injection of electrons into the plasma wave. The results are published in [35]. The*

*experimental results are supported by 3-D PIC simulations, which for the first time include the full description of the probe pulse propagation through the plasma and the imaging setup. Here, special attention was paid to the formation of the shadowgrams and the resultant quantities like the plasma wavelength.*

- *Chapter 5: Results of experiments investigating the influence of the target gas on the LWFA are presented. It was found that with hydrogen as the target gas the generated electron pulses have a higher pointing stability, lower divergence and higher bunch charge than when using helium. These electron pulses were then applied in an experiment to study the in vivo dose response of cancer cells to electron pulses [36]. To investigate the mechanism responsible for the observed differences in electron acceleration depending on the target gas experiments were carried out with varying rise times of the ps contrast of the laser pulse. Here, the combination of different probing diagnostics (shadowgraphy and interferometry) and the detection of backscattered radiation lead to the identification of the Stimulated Raman instability as the cause.*
- *Chapter 6: A summary of this thesis is given and an outlook for the scalability of FCM for future plasma accelerators is provided. Furthermore, a technique suitable for the generation of movies from the interaction in a single shot is proposed.*

## 2. Theory of high intensity laser-plasma interactions

This chapter gives a fundamental overview of the interaction between high intensity laser pulses and an underdense plasma resulting in the excitation of electron oscillations forming a plasma wave. Electrons can be injected into this plasma wave and experience longitudinal electric fields of more than 100 GV/m. Optimal conditions for the acceleration are derived and scaling laws are presented. The focus is then directed to plasma dynamics and the origin of plasma instabilities including their influence on the injection and acceleration process.

### 2.1 Ionization mechanisms

Before the huge electric fields in plasma can be utilized, matter has to be ionized by a high-intensity laser pulse. Considering Ti:sapphire lasers, the energy of a single photon is  $\hbar\omega_0 = 1.55$  eV, with  $\omega_0$  being the laser's angular frequency. This photon energy is smaller than the energy required for the direct ionization of the gases relevant for this thesis, e.g., hydrogen molecules (15.6 eV) and helium (24.6 eV  $\text{He}^+$  and 54.4 eV  $\text{He}^{2+}$ ). Therefore, these gases cannot be directly ionized via the photoelectric effect. However, at sufficiently high intensities, nonlinear effects become relevant and interaction with multiple photons or with the strong laser field itself can lead to the ionization of matter, see Figure 2.1. If the photon number density in the laser focus is comparable to the atomic or molecular number density of the target gas, then the probability that multiple photons can be absorbed by a single atom or molecule becomes non-negligible, see Figure 2.1a. The lifetime of the short-lived virtual electronic states is on the order given by Heisenberg's uncertainty. The process is termed multi-photon ionization (MPI). The electron can actually absorb more photons than required for ionization and leave the atom with a distinct energy. This process is termed above threshold ionization (ATI). The process is termed tunnel ionization (TI). The process is termed barrier suppression ionization (BSI).

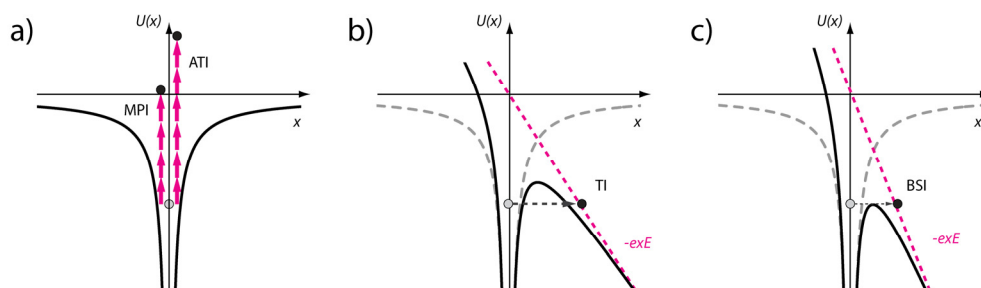


Figure 2.1 | Ionization mechanism in strong electric fields. a) Multi Photon Ionization and Above Threshold Ionization b) Tunnel Ionization c) Barrier Suppression Ionization.

For higher laser intensities, where the electric field of the laser exceeds the binding potential of the electron, the process can no longer be treated with a perturbative approach and is dominated by tunnel ionization (TI). TI can be understood by a Coulomb potential, which is modified by a stationary, homogeneous field. The electron can then tunnel through the finite width of the barrier, see Figure 2.1b. The rate for tunnel ionization was derived by Ammosov, Delone and Krainov [37] and is in reasonable agreement with experimentally deduced ionization rates. The limit between MPI and TI can be estimated by the Keldysh parameter  $\gamma_k$  [38].

$$\gamma_k = \sqrt{\frac{E_{\text{ion}}}{2\Phi_{\text{pond}}}} \quad (2.1)$$

with  $E_{\text{ion}}$  being the ionization potential and  $\Phi_{\text{pond}}$  the ponderomotive potential, i.e., the electron quiver energy averaged over one oscillation period. Clearly, this rate is only valid as long as the laser field is less than the Coulomb field. If the electric field is strong enough, the electron can be freed spontaneously. This is the process of barrier suppression ionization (BSI), a special case of TI, see Figure 2.1c. The threshold laser intensity for BSI is estimated by setting the Coulomb potential equal to the ionization potential.

$$I_L = \frac{\pi^2 \epsilon_0^3 c}{2e^6} \frac{E_{\text{ion}}^4}{Z^2} \quad \text{or} \quad I_L \left[ \frac{\text{W}}{\text{cm}^2} \right] \approx 4.0 \cdot \frac{10^9 (E_{\text{ion}} [\text{eV}])^4}{Z^2} \quad (2.2)$$

Here,  $I_L$  being the laser intensity,  $e$  the electron charge,  $\epsilon_0$  the vacuum permittivity,  $m_e$  the electron rest mass,  $c$  the speed of light and  $Z$  the ionization state after ionization. Typical values for the BSI threshold are given in Table 1.

	H <sub>2</sub>	D <sub>2</sub>	He	He <sup>+</sup>
$E_{\text{ion}}$ (eV)	15.43	15.83	24.59	54.42
$I_L$ (W/cm <sup>2</sup> )	$2.3 \cdot 10^{14}$	$2.5 \cdot 10^{14}$	$1.5 \cdot 10^{15}$	$8.8 \cdot 10^{15}$

Table 1 | Ionization levels and intensity thresholds for barrier suppression ionization for atoms and molecules used in the experiments

For low  $Z$  gases, the BSI model is accurate enough, but the calculation of the exact ionization rates is more complex and has to include the finite pulse duration of the exciting laser pulse as well as the real 3-D shape of the atom or molecule. For molecules such as hydrogen and deuterium, the ionization,  $H_2 \rightarrow H_2^+ + e^-$ , is only the first step and is followed by a possible dissociation into a positively charged ion and neutral atom,  $H_2^+ \rightarrow H^+ + H$ . The required energy for the dissociation ( $E_{\text{diss}, H_2^+} = 4.48$  eV) and the subsequent ionization of

the neutral atom ( $E_{\text{ion},H} = 13.6$  eV) is less than the energy required for the initial ionization of the molecule [39]. As these processes are occurring during the rising edge of the laser pulse hydrogen and deuterium are completely ionized if the intensity for BSI is exceeded.

Depending on the type of gas and the temporal intensity profile of the laser pulse, the gas can be completely ionized about 1 ps before the peak of the laser pulse (see Section 5.1), which can then give rise to a number of laser plasma instabilities like Stimulated Raman backscattering.

## 2.2 Electron motion in an electromagnetic field

The interaction of an intense laser pulse with a plasma can be described on a fundamental level by the motion of the electrons and ions in the plasma due to the electric and magnetic fields,  $\mathbf{E}$  and  $\mathbf{B}$  respectively, of the laser pulse. Both  $\mathbf{E}$  and  $\mathbf{B}$  are described by vector fields; however, their spatial and temporal variables will either be omitted in the following discussion or reduced to a one-dimensional treatment. The laser pulses used in the experiment can be approximated with good accuracy as pulses with a Gaussian envelope in space and time. Although the laser pulses need to be focused to reach the desired intensities, in the focal region the laser pulse can be approximated by a plane wave for many applications.

The relativistic Lorentz equation describes the interaction of an electron with the mass  $m_e$  and charge  $e$  under the influence of an electromagnetic field.

$$\frac{d\mathbf{p}}{dt} = \frac{d}{dt}(m_e\gamma\mathbf{v}) = -e(\mathbf{E} + \mathbf{v} \times \mathbf{B}) \quad (2.3)$$

with  $\gamma$  being the relativistic factor which is connected to the particle's velocity  $\mathbf{v}$  by  $\gamma = 1/\sqrt{1 - \beta^2}$  with  $\beta = |\mathbf{v}|/c$  the normalized velocity. In the relativistic case, the magnetic field in Eq. (2.3) becomes non-negligible and the electron dynamics become nonlinear. Approaching the relativistic regime, a dimensionless parameter is commonly introduced as

$$a_0 = \frac{eE_0}{\omega_0 m_e c} = 1. \quad (2.4)$$

with  $E_0$  being the amplitude of the electric field. For  $a_0 = 1$ , the kinetic energy an electron would acquire in a laser pulse is equal to its rest energy. In terms of the laser intensity  $I_L$ ,  $a_0$  can be expressed as

$$I_L = \frac{a_0^2}{\lambda_0^2} 1.37 \cdot 10^{18} \frac{\text{W}}{\text{cm}^2}. \quad (2.5)$$

with  $\lambda_0$  being the laser wavelength in  $\mu\text{m}$ . For typical Ti:sapphire based laser systems ( $\lambda_0 = 0.8 \mu\text{m}$ ),  $a_0 = 1$  is reached at laser intensities of  $I_L = 2.1 \cdot 10^{18} \text{ W/cm}^2$ .

At this point it makes sense to introduce the vector potential  $\mathbf{A}$  and the scalar potential  $\phi$  to express  $\mathbf{E}$  and  $\mathbf{B}$ .

$$\begin{aligned} \mathbf{E} &= -\frac{\partial \mathbf{A}}{\partial t} - \nabla \phi \\ \mathbf{B} &= \nabla \times \mathbf{A} \end{aligned} \quad (2.6)$$

Using the vector potential  $\mathbf{A}$  and assuming interaction in vacuum ( $\phi = 0$ ) the equation of motion has the form:

$$\frac{d\mathbf{p}}{dt} = \frac{\partial \mathbf{p}}{\partial t} + (\mathbf{v} \cdot \nabla) \mathbf{p} = e \left( \frac{\partial \mathbf{A}}{\partial t} - \mathbf{v} \times \nabla \times \mathbf{A} \right) = e \left( \frac{d\mathbf{A}}{dt} - \nabla(\mathbf{v} \cdot \mathbf{A}) \right) \quad (2.7)$$

In a plane wave, we have  $\frac{\partial}{\partial y}(v_{\perp} A_0) = \frac{\partial}{\partial z}(v_{\perp} A_0) = 0$ . From there it follows  $\frac{dp_{\perp}}{dt} = e \frac{dA}{dt}$  and integration leads to the first invariant of the electron's motion  $C_1$

$$\Rightarrow p_{\perp} - eA = C_1. \quad (2.8)$$

Using Eq. (2.7) to analyze the longitudinal momentum  $p_{\parallel}$  of the electron leads to the second invariant of the electron's motion  $C_2$

$$\begin{aligned} \frac{dp_{\parallel}}{dt} &= -ev_{\perp} B_0 = m_e c \frac{d\gamma}{dt} \\ \Rightarrow \gamma - \frac{p_{\parallel}}{m_e c} &= C_2 \end{aligned} \quad (2.9)$$

For an electron initially at rest, i.e.,  $\mathbf{p} = 0$  at  $t = 0$ , one finds  $C_1 = 0$  and  $C_2 = 1$  and, hence,

$$\begin{aligned} p_{\perp} &= eA \\ E_{\text{kin}} &= m_e c^2 (\gamma - 1) = p_{\parallel} c = \frac{1}{2} \frac{p_{\perp}^2}{m_e c} \end{aligned} \quad (2.10)$$

revealing two conservation laws for the electron motion: the transverse momentum  $p_{\perp}$  and the kinetic energy  $E_{\text{kin}}$ . Using the definition of the normalized vector potential yields the relativistic Lorentz factor for a single electron in the laser field

$$\gamma = 1 + a^2/2. \quad (2.11)$$

All the calculations from above can be used to solve the equation of motion and the trajectory of a single electron in a light field described by,  $\mathbf{a} = a_0 \cos(\omega_0 \tau) \mathbf{e}$ , yields

$$\begin{aligned}
x(\tau) &= \frac{ca_0^2}{8\omega_L} [2\omega_0\tau - \sin(2\omega_0\tau)] \\
y(\tau) &= \frac{c}{\omega_L} a_0 [\sin(\omega_0\tau)] \\
z(\tau) &= 0
\end{aligned} \tag{2.12}$$

with  $\tau = t - \frac{x(\tau)}{c}$ . The transverse  $y$ -motion is an oscillation similar to the classical motion. The longitudinal motion along the  $x$ -axis is a combination of an oscillation at the second harmonic of the light field and a longitudinal drift motion  $x_{\text{drift}} = \frac{a_0^2}{4+a_0^2} ct$ , see Figure 2.2. In the drift frame, this results in a figure-of-8 motion. Only the transverse electric field of

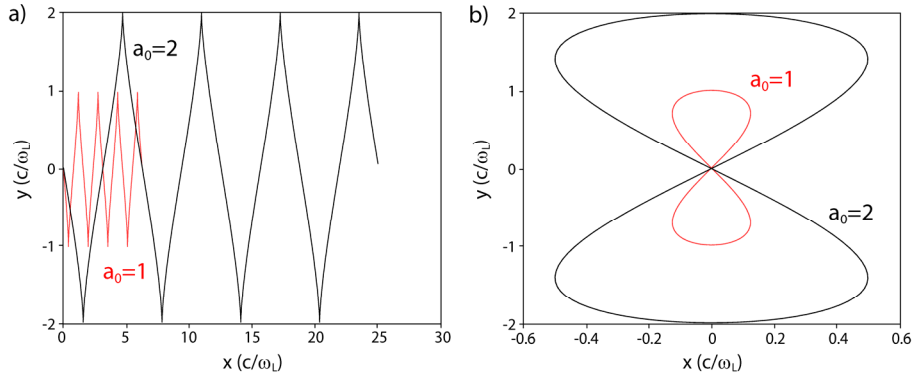


Figure 2.2 | Trajectory of an electron in an intense light field for different  $a_0$ . a) Motion as seen in the laboratory frame. b) Figure-8 motion as seen in the frame co-moving with the electron's drift velocity.

the light field increases the energy of the electron, while for nearly relativistic velocities,  $v \approx c$ , the  $\mathbf{v} \times \mathbf{B}$ -force results in a net shift of this motion in the laser propagation direction. For a laser pulse with an infinite transverse extent, i.e., a plane wave but with finite duration, the electron comes to rest after the pulse has passed and no net energy is transferred. The problem of vacuum acceleration was generalized and has become known as the *Lawson-Woodward theorem* [40, 41]. The main conclusions are that an isolated electron cannot gain a net energy by interacting with an electromagnetic field under the following assumptions:

1. The interaction region is infinite.
2. The electron is highly relativistic along the acceleration path.
3. No boundaries are present.
4. No static electric or magnetic fields.
5. Nonlinear effects are negligible.

If one of the above points is violated then laser driven particle acceleration is possible. However, the net available acceleration field is largely reduced compared to the electric

field of the laser  $E_0$ . For example, laser pulses with  $P = 30$  TW focused down to  $A = 3 \mu\text{m}^2$  with a Strehl-ratio of 0.6 result in an intensity of  $I_L = 3 \cdot 10^{20}$  W/cm<sup>2</sup> and hence  $E_0 \approx 50$  TV/m. In comparison, achievable acceleration fields in a LWFA are currently limited to the 10-100 GV/m range, as will be described later.

## 2.3 Ponderomotive force

As it was mentioned in the previous section, electrons in a plane wave cannot gain any net energy. However, in the high gradients of a focused laser beam the spatial variation of the electric and magnetic fields lead to a net force on the electron. Here, this net force is calculated by including second order terms into the electron's equation of motion. These terms include the spatial dependence of the electric field and the  $\mathbf{v} \times \mathbf{B}$  term. In the limit of low intensity laser pulses,  $a_0 \ll 1$ , the ponderomotive force is obtained by averaging over the fast oscillations of the laser field.

$$\mathbf{F}_{\text{pond}} = \left\langle \frac{d\mathbf{p}}{dt} \right\rangle = -\frac{1}{2} m_e c^2 \nabla \langle a^2 \rangle \quad (2.13)$$

This force is opposed to the gradient of the intensity, i.e., it drives electrons away from regions of high fields. Associated with this force is the so-called ponderomotive potential  $\Phi_{\text{pond}} = \frac{1}{2} m_e c^2 \cdot \langle a^2 \rangle$ , which is also equal to the mean kinetic energy of the electrons in the field. For relativistic pulses ( $a > 1$ ) one would assume to exchange  $m_e \rightarrow \langle \gamma \rangle m_e$ , with  $\langle \gamma \rangle$  being the temporally averaged relativistic factor of the electron. More detailed calculation by Quesnel and Mora [42] showed that this is indeed justified if: a) it can be assumed that the transverse intensity gradient is on a scale larger than the laser wavelength, b) the pulse length is much longer than the wavelength of the laser, and c) the initial motion of the electron in laser propagation direction normalized to  $c$  is small. The result is

$$\left\langle \frac{d\mathbf{p}}{dt} \right\rangle = -\frac{e^2}{2m_e} \nabla \langle A^2 \rangle = -\frac{1}{2} m_e c^2 \frac{1}{\langle \gamma \rangle} \nabla \langle a^2 \rangle. \quad (2.14)$$

## 2.4 Laser propagation in underdense plasmas/ nonlinear relativistic optics

In general, a plasma consists of positively and negatively charged particles. If a test particle is injected into the plasma, its electric field is shielded by the plasma within a distance given by the Debye length  $\lambda_D$ . This distance has to be smaller than the extension of the plasma itself for ionized matter to act like a plasma.

$$\lambda_D = \sqrt{\frac{\epsilon_0 k_B T_e}{e^2 n_e (1 + Z T_e / T_i)}} \quad (2.15)$$



Here,  $k_B$  is the Boltzmann factor,  $T_e$  the electron temperature,  $T_i$  the ion temperature and  $n_e$  the electron density. This equation only holds true if the electrons and the ions are in thermal equilibrium within each species but not necessarily with each other. For the time scales relevant in the experiments described in this thesis, the temperature of the ions,  $T_i$ , can be neglected in comparison to the temperature of the electrons. This is justified as the ions can be assumed to be immobile at the considered intensities and the timescale of the laser pulse's duration is short in comparison to the inverse of the ion plasma frequency.

If the electrons are displaced from the stationary and uniform positive ion background, they experience a force arising from the electric field due to the charge displacement, which drives the particles back to their equilibrium position. However, the electrons will overshoot due to their acquired kinetic energy. As a consequence, the electrons perform a harmonic oscillation with a characteristic frequency, the (angular) plasma frequency, which only depends on the density  $n_e$  of the plasma electrons

$$\omega_p^2 = \frac{n_e e^2}{\epsilon_0 \langle \gamma \rangle m_e} \quad (2.16)$$

with  $\langle \gamma \rangle$  being time- and space-averaged Lorentz factor of the electrons. For an external electromagnetic field with a frequency exceeding the plasma frequency, the external wave can propagate in the plasma. For frequencies smaller than the plasma frequency, the inertia of the electrons is small enough to follow the oscillation of the applied electromagnetic field so that the wave cannot propagate anymore. Such a plasma is labelled *overdense*. A part of the wave is reflected at the vacuum plasma interface while the incident wave is damped inside the plasma. The layer at which the laser pulse is reflected has a density called the *critical density*. For the Ti:sapphire laser system, which was used for the experiments in this thesis, the central wavelength is  $\lambda_0 = 0.8 \mu\text{m}$ , which corresponds to a critical density of  $n_c = 1.74 \cdot 10^{21} \text{ cm}^{-3}$ . The typical electron densities in the experiments described in Chapters 4 and 5 are in the range of  $n_e = (1 \dots 2) \cdot 10^{19} \text{ cm}^{-3}$  and thus  $n_e/n_c \approx 0.01$ . Therefore, the plasma is called *underdense*. The implication of Eq. (2.15) for high intense laser pulses is that an initially overdense plasma can become underdense if the relativistic  $\gamma$ -factor of the plasma electrons becomes large enough allowing the laser pulse to propagate. This scheme is applied in novel ion acceleration mechanisms like radiation pressure acceleration [43]. In Section 4.8, where the simulations of the experiments are discussed, the influence of the relativistic  $\gamma$ -factor on the image formation will be shown in simulations as well as in experiments.

The propagation of electromagnetic waves in an underdense plasma is described by the dispersion relation

$$\omega_0^2 = c^2 k_0^2 + \omega_p^2 \quad (2.17)$$

resulting in the refractive index  $\eta$  of the plasma

$$\eta = \sqrt{1 - \frac{\omega_p^2}{\omega_0^2}} = \sqrt{1 - \frac{n_e}{n_c}}. \quad (2.18)$$

The group velocity and the phase velocity of the electromagnetic wave,  $v_g$  and  $v_\phi$ , in the plasma are given by

$$v_g = \frac{\partial \omega_0}{\partial k_L} = \eta \cdot c \text{ and } v_\phi = \frac{\omega_0}{k_L} = \frac{1}{\eta} \cdot c \quad (2.19)$$

## 2.5 Nonlinear relativistic optics

The strong dependence of the refractive index on the plasma frequency, and therefore the plasma electron's  $\gamma$ -factor gives rise to a number of nonlinear relativistic effects like self-focusing, self-phase modulation and pulse compression. Due to the temporal and spatial profile of a laser pulse,  $I(r, t)$  the refractive index changes accordingly in space and time

$$\eta = \sqrt{1 - \frac{\omega_p^2}{\langle \gamma \rangle \omega_0^2}} = \eta(I(r, t)). \quad (2.20)$$

Each contribution to the refractive index is influenced in a different way. The plasma frequency,  $\omega_p$ , depends on the electron density, which is influenced by ionization. Higher intensities lead to higher electron densities up to the point of a fully ionized plasma, e.g., for hydrogen at an intensity of  $10^{14}$  W/cm<sup>2</sup> or for helium at intensities close to  $10^{15}$  W/cm<sup>2</sup>. The laser beam profile on axis creates a higher on-axis electron density and thus the refractive index is lower, while off-axis the refractive index is higher. The induced wavefront curvature leads to defocusing. On the other hand, the ponderomotive force expels electrons from the regions of highest intensity and thus lowers the electron density there, which gives rise to focusing at intensities above  $10^{18}$  W/cm<sup>2</sup>. The  $\gamma$ -factor of the plasma electrons depends on the local intensity via

$$\gamma = \sqrt{1 + a^2} \quad (2.21)$$

which can be obtained by solving the relativistic equation of motion of the plasma. It differs slightly compared to the solution in vacuum, cf. Eq. (2.11). The modification is caused by the electrostatic force due to the laser induced charge separation, which balances the

ponderomotive force. For small electron density modulations and weakly relativistic pump pulses ( $a_0^2 \ll 1$ ) the index of refraction for linear polarization can be approximated and expanded as [29, 44, 45]

$$\eta = 1 - \frac{1}{2} \frac{\omega_p^2}{\omega_0^2} \left( 1 - \frac{a_0^2}{4} + \frac{\delta n_e}{n_e} - 2 \frac{\delta \omega_0}{\omega_0} \right) \quad (2.22)$$

with  $\delta n_e/n_e$  being the normalized density perturbation. This term is influenced by the transverse ponderomotive force and for  $\delta n_e/n_e < 0$  it is responsible for self-focusing plasma wave guiding and self-modulation of long ( $c\tau_L > \lambda_p$ ) laser pulses. In the case  $\delta n_e/n_e > 0$ , defocusing occurs and the peak intensity is reduced.

This happens mostly during the early stage of ionization. The last term is responsible for self-phase modulation, i.e., photon acceleration and deceleration, and leads to self-compression of the pump pulse. The leading term is the  $a_0^2$ -term, which is related to relativistic self-focusing. The laser pulses are guided by refraction if  $\partial\eta/\partial r < 0$ , which is fulfilled in the case of laser pulses which have their peak intensity on axis,  $\partial a_0^2/\partial r < 0$ . The critical power, which is needed for self-guiding, can be derived from balancing the natural diffraction of the laser pulse with self-focusing. The result for a Gaussian beam is [46]

$$P_{\text{crit}} = 2 \frac{m_e^2 c^5}{e^2} \frac{\omega_0^2}{\omega_p^2} \approx 17.4 \text{ GW} \cdot \frac{\omega_0^2}{\omega_p^2} \quad (2.23)$$

Self-focusing depends on the power and not on the intensity as the vacuum diffraction time is  $\propto w_0^{-2}$ , with  $w_0$  being the focal spot size, while the intensity dependent component of the refractive index is  $\propto w_0^2$  and the effect on the beam radius of these two effects cancels out. For typical LWFA parameters ( $n_e = 1 \cdot 10^{19} \text{ cm}^{-3}$ ) with the JETi40 laser ( $\lambda_0 = 0.81 \text{ } \mu\text{m}$ ),  $P_{\text{crit}} = 3 \text{ TW}$  which is 10 times lower than the peak power of the laser pulses. However, this neglects the density response term  $\delta n_e/n_e$  in the refractive index, e.g., by the ponderomotive force. This term becomes important for short pulses [47],  $c\tau_L < \lambda_p$ , since the index of refraction is modified by the laser pulse on the timescale of the plasma frequency and not on the timescale of the laser frequency. The longitudinal intensity gradient of the laser pulse pushes the electrons in the forward direction. This decreases the refractive index for the front of the pulse and thus nearly cancels the relativistic self-focusing term and so the front of the pulse diffracts even when  $P \cong P_{\text{crit}}$ . However, propagation over several Rayleigh length is still possible as the front of the pulse depletes faster than it diffracts due to plasma wave excitation [48]. Guiding over much larger distances requires an externally generated structure, which can be realized by a heating pulse [18], cluster explosion [49] or electric discharge [50].

## 2.6 Temporal compression and photon acceleration

Similar to the optical Kerr effect, which is responsible for transverse self-focusing and longitudinal pulse compression by self-phase modulation at intensities of the order of  $10^{11}$  W/cm<sup>2</sup> for solids and  $10^{14}$  W/cm<sup>2</sup> for gases, similar nonlinear effects occur in the relativistic regime. A longitudinal variation in the refractive index leads to a variation in the laser pulse's group velocity. The pulse front experiences a lower group velocity since the electron density is higher there, whereas the pulse's trailing edge is situated in the remaining ion channel created by the ponderomotive force, and thus experiences a higher group velocity. This leads to pulse compression. At the same time, such a variation in longitudinal refractive index also leads to a change of the phase velocity of the laser pulse. This changes the instantaneous wavelength across the laser pulse. As the pulse evolves, the ponderomotive force also pushes electrons towards the leading edge of the pulse and thus increases the electron density gradients further. This increases the intensity gradient and leads to a higher plasma wave amplitude. The phase velocity dispersion connected to this process blue-shifts the wavelength of the photons at the leading edge (photon acceleration) and red shifts the photons at the back of the pulse. This effect and subsequent compression of the laser pulse can result in a shortening of the pulse duration from an initial 38 fs to 10-14 fs [51] with a transmission efficiency of ca. 20 %. More sophisticated diagnostics analyzing the amplitude and the phase of the transmitted laser pulse showed the scaling of this effect with interaction length and plasma density [52]. A simple model for the rate of the pulse compression was derived. It is based on the assumption that the front of the laser pulse travels with the group velocity of the laser pulse and the back of the pulse travels in vacuum due to the expelled electrons

$$\tau(l) \approx \tau_0 - \frac{n_e l}{2cn_c} \quad (2.24)$$

with  $l$  being the propagation length. The pulse compression and hence the evolution of the laser pulse can be influenced by the laser pulse's chirp [53]. A positive chirp leads to enhanced pulse compression with an increase of the peak power, which is beneficial for laser pulses in the 10 TW range. For laser pulses with peak powers above 100 TW a negative chirp can be beneficial. It counteracts pulse compression and the pump pulse hardly evolves. This prevents continuous injection of electrons, which form the so called *dark current* [53].

## 2.7 Laser plasma instabilities

In this section, instabilities are discussed which are relevant to the propagation and evolution of the laser pulse and can grow significantly on a timescale shorter than the ion

response time. These laser-plasma instabilities, depending on the initial pump pulse and plasma conditions, can increase the plasma wave amplitude or the peak power of the laser pulse, e.g., by self-modulation. However, their characteristic exponential growth can also limit the laser's propagation distance and hence degrade the performance of a LWFA. As it will turn out, the laser and plasma parameters used in the experiments described in Chapters 4 and 5 are in a regime where a number of instabilities are excited during different stages in the laser pulse's propagation. Few-Cycle Microscopy (Section 3.5.2) will be the key technique to observe and identify these instabilities.

### 2.7.1 Stimulated Raman scattering

Stimulated Raman scattering is a consequence of the interaction of a light wave with an electron plasma wave [54]. In its most basic form, it consists of the decay of the pump laser field, with frequency and wave number  $(\omega_0, \mathbf{k}_0)$ , into an electron plasma wave  $(\omega_e, \mathbf{k}_e)$  and two scattered light waves, namely an anti-Stokes wave  $(\omega_0 + \omega_e, \mathbf{k}_0 + \mathbf{k}_e)$  and a Stokes wave  $(\omega_0 - \omega_e, \mathbf{k}_0 - \mathbf{k}_e)$ , see Figure 2.3. A growing wave has a complex frequency,  $\omega_e \cong \omega_p + i\Gamma$ , where the growth rate  $\Gamma$  is obtained through a standard linear instability analysis taking into account all these interacting waves.

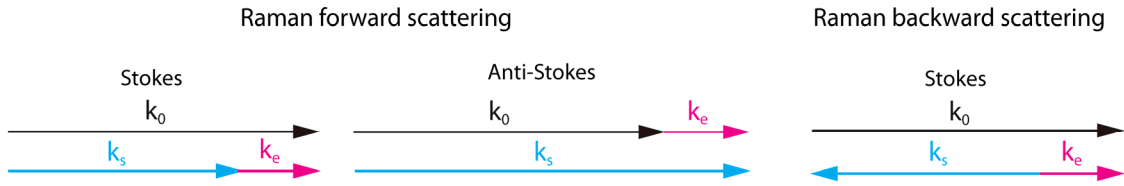


Figure 2.3 | Vector diagrams for Raman scattering.  $k_0$ : pump wave;  $k_e$ : electron plasma wave;  $k_s$ : scattered wave.

#### Stimulated Raman Backscattering (SRS-B)

In Raman backscattering, the pump wave  $(\omega_0, k_0)$  decays into a plasma wave  $(\omega_e, k_e)$  and a backward propagating scattered wave  $(\omega_0 - \omega_e, k_0 - k_e)$ , where  $\omega_e \cong \omega_p$  and  $k_e \cong 2k_0$ . The temporal growth rate for the amplitude of the wave in the limits  $a_0^2 \ll \omega/\omega_0 \ll 1$ , is given by [54],

$$\Gamma = \frac{a_0}{4} (\omega_p \omega_0)^{1/2} \cos(\theta) \quad (2.25)$$

with  $\theta$  being the angle between the scattered mode and the pump wave, which will be referred to as side scattering for  $\theta \neq 0$ . Typically, SRS-B is the instability with the highest growth rate of all Raman scattering instabilities. However, for high pump intensities, the backscattered spectrum broadens and the  $\omega_0 - \omega_p$  peak can no longer be distinguished [55]. The phase velocity of the SRS-B plasma wave is  $v_\phi = \omega_e/k_e = \omega_e/2k_0 \ll c$ . Since  $v_\phi/c \ll 1$ , the plasma wave can trap background thermal electrons and heat the plasma.

The resulting fast electrons can then be subsequently trapped by Raman scattered modes propagating at smaller angles,  $\theta$ , which will accelerate the electrons to even higher energies [56]. Simultaneously, Raman side scattering and backscattering can erode the back of a long pulse,  $c\tau_L > \lambda_p$ , since the instability grows from the front to the back of the pulse and energy is lost due to the scattering [57]. For laser pulses with  $a_0 > 1$ , the growth of SRS-B is suppressed due to the ponderomotive blowout, meaning no electrons are positioned in the back of the laser pulse and the instability has no “medium” in which to grow. However, if the pump pulse is depleted, the instability can grow rapidly again due to a high plasma wave number  $k_p$  at the sharp density spike in the central part of the laser pulse, see Section 5.4. For sufficiently large relativistic plasma wave amplitudes, self-trapping of background electrons can also occur in the absence of SRS-B [58].

### Stimulated Raman forward scattering (SRS-F)

In Raman forward scattering, the scattered wave propagates parallel (or nearly parallel) to the pump wave, and the associated plasma wave has a phase velocity  $v_\phi \cong c$ . Hence, the plasma wave can be used to accelerate electrons to high energies. The SRS-F instability can serve as the basis for a LWFA, in which a single, long ( $c\tau_L > \lambda_p$ ) laser pulse becomes modulated at the plasma frequency via SRS-F and drives a large amplitude plasma wave. An LWFA based on SRS-F can be regarded as the 1-D analog to the self-modulated LWFA. Several regimes of the SRS-F can be identified: such as a four-wave regime, in which both  $\omega_0 \pm \omega_p$  modes are resonant with the pump laser and the plasma wave; a three-wave regime, in which only  $\omega_0 - \omega_p$  is resonant; as well as an intermediate four-wave nonresonant regime. However, the spatio-temporal analysis indicates that as the SRS-F grows, it passes through these various phases. Making the assumption that the SRS-F instability saturates after 5 e-foldings it was derived from PIC simulations that SRS-F dominates if the following inequality is fulfilled [44]:

$$\Gamma_{\text{SRS-F}} = P[\text{TW}]\tau_L[\text{ps}]n_e[10^{19} \text{ cm}^{-3}]^{5/2}\lambda[\mu\text{m}]^4 \geq 3 \quad (2.26)$$

For typical LWFA parameters used in the experiments with the JETi 40 laser system,  $P = 25 \text{ TW}$ ,  $\tau_L = 30 \text{ fs}$ ,  $n_e = 1.6 \cdot 10^{19} \text{ cm}^{-3}$ ,  $\lambda_0 = 0.81 \mu\text{m}$ , this yields  $\Gamma_{\text{RFS}} \approx 1$ , which is an indicator that SRS-F is still present but not dominating. Due to the strong dependence on the electron density, SRS-F is dominant for  $n_e > 2.5 \cdot 10^{19} \text{ cm}^{-3}$ . It is important to note that this inequality (Eq. 2.26) is an energy and not a power threshold.

### Stimulated Raman Scattering in 3-D

It was shown in the previous section that in 1-D the growth rate of the Raman instability has a minimum when the scattered light propagates in forward direction. However, in two

or three dimensions the growth rate can be higher. For a laser pulse with a power higher than  $P_c$  will undergo nonlinear self-focusing. For SRS-F, the scattered electromagnetic wave beats with the co-propagating incident wave and a slowly varying intensity modulation is formed. This leads to a modulation of the electron density because of the varying ponderomotive force. At the density peaks within the modulated beam the self-focusing occurs faster, which increases the modulation further [59]. The growth rate for the self-modulation instability was derived by Mori *et al.* [60]. In the same sense as for the SRS-F instability, the importance of self-modulation can be estimated [44]:

$$\Gamma_{SM} = P[\text{TW}] \tau_L[\text{ps}] n_e [10^{19} \text{ cm}^{-3}]^{5/2} \lambda[\mu\text{m}]^4 \leq 0.4 \quad (2.27)$$

Using the LWFA parameters from the previous section,  $\Gamma_{SM} \approx 1$ , so self modulation is relevant for  $n_e \leq 1 \cdot 10^{19} \text{ cm}^{-3}$ , for a depleted pump, and for large propagation distances. For larger  $a_0$ , the growth of this instability is suppressed due to the relativistic mass increase of the electrons and the decrease in  $\omega_p$ . However, the phase velocity must still be close to  $c$  and so the wavenumber  $k_p$  must decrease.

### 2.7.2 Filamentation

During the propagation of the laser pulse, the pulse can break up into a number of filaments due to the feedback between transverse modulations in the refractive index and transverse modulations in the laser intensity. The instability arises from self-focusing and can therefore occur from ponderomotive or relativistic effects. Filamentation limits the efficiency of laser driven electron acceleration since the splitting of the main beam reduces the energy and therefore reduces the overall acceleration length.

## 2.8 Plasma waves and acceleration

In the subsequent sections, the excitation and propagation of plasma waves are discussed. Reducing the complexity to 1-D in space and modelling the plasma as a cold fluid, equations that govern the excitation of plasma waves are derived. Finally, scaling laws for the maximum electron energy and trapping conditions for self-injection are presented. The following discussion is mainly based on review articles [44, 45, 61].

### 2.8.1 Plasma wave generation

The ponderomotive force of an intense laser pulse pushes the plasma electrons out of the regions of highest intensity. Due to their higher mass-to-charge ratio, the ions remain fixed and the space charge field pulls the electrons back. This leads to an oscillation with  $\omega_p$ . As the laser propagates with its group velocity  $v_g$  through the plasma, it continuously pushes the electrons away from regions of high intensity, which results in a plasma wave

with a relativistic phase velocity  $v_\phi \cong v_g$ . Although a complete description has to be done in 3-D, principal properties of laser generated wake fields can also be derived from an analysis in the 1-D nonlinear regime, which is thoroughly given by Gibbon [62]. It is assumed that the laser driver is non evolving and is only a function of the coordinate  $\xi = x - v_g t$ . The generation of 1-D plasma waves in the cold fluid limit is described by

$$\frac{1}{k_p^2} \frac{\partial^2 \phi}{\partial \xi^2} = \gamma_g^2 \left\{ \beta_g \left[ 1 - \frac{1 + a^2}{\gamma_g^2 (1 + \phi)^2} \right]^{-1/2} - 1 \right\} \quad (2.28)$$

with  $\phi$  and  $a$  the electrostatic wake and vector potential normalized to  $\frac{m_e c^2}{e}$  respectively,  $\gamma_g = (1 - \beta_g^2)^{-1/2}$  and  $\beta_g = \frac{v_g}{c}$ . Eq. (2.28) can be simplified using the quasi-static approximation (QSC) [47]. Using this approximation, it is assumed that the laser pulse is sufficiently short compared to the timescale, in which the laser envelope evolves,  $\tau_e \approx \frac{\omega_0}{\omega_p} \omega_p^{-1}$ . In an underdense plasma,  $\omega_0 \gg \omega_p$ , this condition is fulfilled since this time  $\tau_e$  is long compared to the plasma period. Additionally the diffraction time has to be long compared to  $\tau_e$ , which is satisfied when the laser spot size  $w_0 \gg \lambda_p$ . If the laser group velocity approaches the speed of light,  $\beta_g \rightarrow 1$ , this leads to

$$\frac{1}{k_p^2} \frac{\partial \phi^2}{\partial \xi^2} = \frac{1}{2} \left[ \frac{1 + a^2}{(1 + \phi)^2} - 1 \right]. \quad (2.29)$$

Once this differential equation is solved for the wake potential, the wakefield quantities  $\phi$  and  $n_0$  can be calculated and the longitudinal electric field can be derived. Examples of the solution are given for a low pump amplitude ( $a_0 = 0.5$ , Figure 2.4a) and for a high, relativistic pump amplitude ( $a_0 = 2$ , Figure 2.4b). In the latter, the plasma wave has become strongly nonlinear and characteristic electron density spikes have formed with linear electric fields in between them. At the same time, the period of the wake field has increased. For a square pump pulse Eq. (2.29) was solved by Berezhiani and Murusidze [63] analytically and the following scaling for the potential  $\phi_{\max}$  and the peak electric field  $E_{0,\max}$  were derived.

$$\phi_{\max} \sim a_0^2 \quad \text{and} \quad E_{0,\max} \sim \frac{a_0^2}{\sqrt{1 + a_0^2}} \quad (2.30)$$

To drive the wakefield efficiently not only a high  $a_0$  is required but the pulse duration and temporal shape should be matched as well [64]. As a rule of thumb, resonance is achieved when  $c\tau_L = \lambda_p/2$ , with  $\tau_L$  measured at the full-width half max of the laser intensity [65].



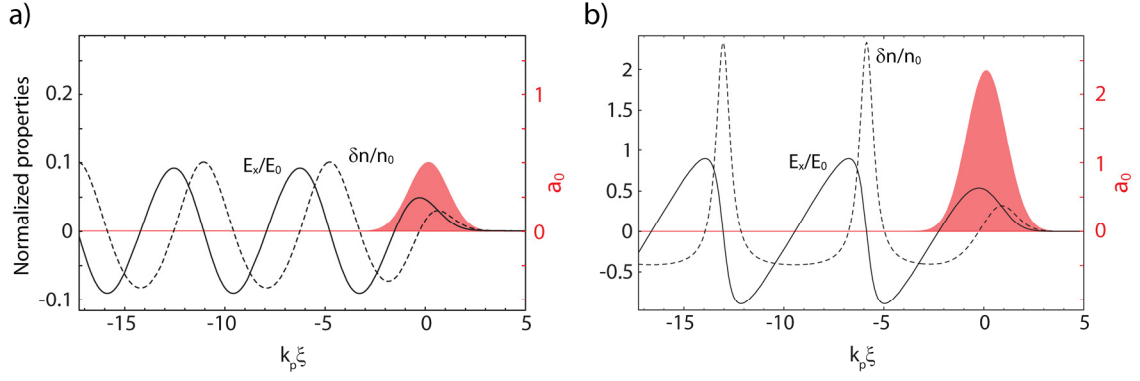


Figure 2.4 | Time- averaged density variation  $\delta n/n_0$  (dashed curve) and axial electric field  $E_x/E_0$  (solid curve) in a LWFA driven by a Gaussian laser pulse (red, pulse is moving to the right, centered at  $k_p \xi = 0$  with rms intensity length  $l_{\text{rms}} = k_p^{-1}$ ) for a)  $a_0 = 0.5$  and b)  $a_0 = 2$ .

## 2.9 Plasma wave phase velocity

As it will be shown in Section 2.12, the phase velocity of the plasma wave determines the minimum injection energy, the maximum energy gain and the dephasing length. For a fixed driver pulse the phase velocity of the plasma wave is almost equal to the group velocity of the laser  $v_\phi = v_g$ . In the 1-D linear regime, the group velocity of a laser pulse in a plasma can be derived from the dispersion relation,  $\omega_0^2 = c^2 k_0^2 + \omega_p^2$ . This leads to  $v_g = c(1 - \omega_p^2/\omega_0^2)^{1/2}$  and the gamma factor of the plasma wave is given by

$$\gamma_\phi = \left(1 - \frac{v_\phi^2}{c^2}\right)^{-1/2} \cong \left(1 - \frac{v_g^2}{c^2}\right)^{-1/2} \cong \frac{\omega_0}{\omega_p} \quad (2.31)$$

Nonlinear corrections performed by Decker and Mori [66] suggest replacing  $\omega_p^2$  with  $\omega_p^2/\gamma$  when transitioning into the relativistic regime .

For an evolving laser pulse, the pulse front is etched away with a velocity  $v_{\text{etch}}$  due to the excitation of the plasma wave. The phase velocity of the plasma wave can be expressed as  $v_\phi = v_g - v_{\text{etch}}$ , where  $v_g$  is the group velocity of the laser pulse in an underdense plasma and hence  $v_\phi \cong c[1 - 3\omega_p^2/(2\omega_0^2)]$  as shown by Decker *et al.* [48]. Consequently, the phase velocity of the wake is smaller than the group velocity of the laser pulse. This changes the gamma factor of the plasma wave including nonlinear corrections to  $\gamma_\phi = \frac{1}{\sqrt{3}} \frac{\omega_0}{\omega_p} \sqrt{\gamma}$ .

## 2.10 Maximum achievable electric field and wave breaking

Plasmas can support large electrostatic waves and their electric fields can be used to accelerate electrons. However, the field cannot reach infinitely large amplitudes. For electron velocities approaching the phase velocity of the plasma wave,  $\gamma_\phi$ , the trajectories of

neighboring charge sheets start to overlap. This process is called longitudinal wave breaking, which results in a collapse of the wakefield structure and sets a limit to the maximum electric field supported by the plasma wave. The non-relativistic cold wave breaking limit is [8]:

$$E_0[\text{V/m}] \approx \frac{m_e \omega_p c}{e} = 96 \sqrt{n_0[\text{cm}^{-3}]} \quad (2.32)$$

The situation changes for relativistic fluid velocities,  $\gamma_\phi \gg 1$ , and a new limit for the wave breaking electric field for a cold relativistic plasma was derived by Akhiezer and Polovin [67]

$$\frac{E_{\text{WB}}}{E_0} = \sqrt{2}(\gamma_\phi - 1)^{\frac{1}{2}} \propto \frac{1}{\sqrt{\omega_p}} \quad (2.33)$$

This limit drops for warm plasmas, because electrons with higher initial velocity can already travel out of the high density spike below the cold wave breaking threshold and be trapped in the plasma wave. Using warm relativistic fluid theories for the thermal wave breaking field amplitude,  $E_{\text{max,th}}$  has been derived by Rosenzweig *et al.* [68] and later unified by Shen and Meyer-ter-Vehn [69] in the form

$$\frac{E_{\text{max,th}}}{E_0} = \left( \frac{4}{27} \frac{m_e c^2}{T_e} \right)^{\frac{1}{4}} \quad (2.34)$$

with  $T_e$  being the electron temperature in eV. Using a plasma temperature of  $T_e = 200$  eV, which can be generated by a combination of ATI heating and collisional heating at high charge states [70],  $n_e = 1 \cdot 10^{19} \text{ cm}^{-3}$  and  $a_0 = 2$  results in the following threshold electric fields for wave breaking:

cold fluid	cold relativistic	warm fluid relativistic
$E_0 = 300 \text{ GV/m}$	$E_{\text{WB}} = 1470 \text{ GV/m}$ $= 4.9 E_0$	$E_{\text{max,th}} = 1320 \text{ GV/m}$ $= 4.4 E_0$

Table 2 | Wave breaking thresholds for different regimes at  $n_e = 1 \cdot 10^{19} \text{ cm}^{-3}$  and  $a_0 = 2$

So far, relativistic effects have increased the wave breaking field and thermal effects have only slightly reduced it. Analyzing Eq. (2.33) shows, that for a plasma temperature,  $T_e \geq 75 \text{ keV}$ , the wave breaking field is actually decreased below the cold limit. This would prohibit the formation of a distinct plasma wave. In Chapter 5, a first experimental glance at this phenomenon is provided.

In comparison to the consideration above, in a 2-D or 3-D geometry transverse effects can lead to wave breaking at lower wave amplitudes. A transverse variation in the plasma

density causes a transverse variation in the plasma wavelength, which was shown by Bulanov *et al.* [71]. These variations are present for plasma guiding channels or for plasma waves driven by relativistic laser pulses. The transverse laser profile causes a variation in the plasma frequency due to a variation of the effective mass of the electrons. This leads to plasma waves with curved phase fronts. In a nonlinear plasma wave the real position of the constant phase surface is shifted from the surface given by the oscillation amplitude  $\varepsilon(y_0)$ , which is assumed to be perpendicular to the parabolic phase front. The position is given by [71]

$$x = \frac{y_0^2}{2\rho} + \frac{\varepsilon(y_0)\rho}{(\rho^2 + y_0^2)^{1/2}} \quad (2.35)$$

$$y = y_0 - \frac{\varepsilon(y_0)y_0}{(\rho^2 + y_0^2)^{1/2}}. \quad (2.36)$$

with  $\rho$  being the radius of curvature of the wavefront. The resulting phase fronts for different values of  $\varepsilon/\rho$  and a displacement, which does not depend on the transverse coordinate  $y$ , is plotted in Figure 2.5a. This rather simple case illustrates how wave breaking can occur in multi-dimensions. When the radius of curvature  $\rho$  grows to be on the order of the electron displacement  $\varepsilon$ , i.e.,  $\varepsilon/\rho \rightarrow 1$ , trajectories will cross. For  $\varepsilon/\rho > 1$  the phase front takes the form of a ‘swallow tail’. If the amplitude of the oscillation varies along the transverse coordinate, e.g., following the Gaussian laser intensity profile of the pump pulse, trajectory crossing takes on a different form, see Figure 2.5b. A small ‘loop’ is formed in front of the plasma wave. Now a small fraction of the sheath electrons is in the accelerating part of the plasma wave and can be accelerated.

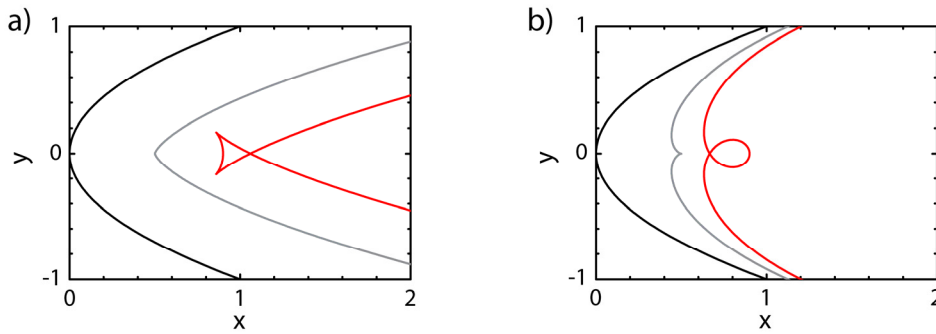


Figure 2.5 | Development of the plasma wave’s phase fronts. Curves of constant phase for  $\rho = 0.5$  and a) for constant  $\varepsilon(y) = \xi_0$ , undisturbed phase front (black line);  $\varepsilon/\rho = 1$  (grey line);  $\varepsilon/\rho = 1.8$  (red line). b) for  $\varepsilon(y) = \varepsilon_0 e^{-2y^2}$ , undisturbed phase front (black line);  $\varepsilon/\rho = 1$  (grey line);  $\varepsilon/\rho = 1.8$  (red line).

Summarizing the discussion from above, relativistic effects increase the field for longitudinal wave breaking but at the same time transverse effects start to play an important role too. In particular, the wavefront curvature depends on the focusing of the laser pulses

and an initial parabolic electron density profile in a plasma channel can lower the wave breaking threshold even further.

## 2.11 Laser wakefield acceleration

Tajima and Dawson have already shown [65], that the ponderomotive force of a strongly focused electromagnetic wave can excite a plasma wave which travels with a relativistic phase velocity. Optimal wave excitation is achieved if  $c\tau_L \approx \lambda_p/2$ . To get into the efficient, hence highly desirable, blowout regime, a laser pulse with  $a_0 > 1$  is required and the focal spot radius has to match the blowout radius, which should also be on the order of  $\lambda_p/2$ . While the spatial requirements can be met by adjusting the size of the focal spot via a focusing optic with an appropriate F-number, temporal matching is more experimentally demanding. The shortest pulse duration determines the necessary plasma density and hence the laser energy or peak power to reach the blowout. To get into this matched regime, where all of the above mentioned conditions are fulfilled, laser pulses with  $\tau_L \approx 30$  fs, need at least a peak power of 60 TW. The JETi40 laser system used in the experiments presented in Chapter 4 and 5 has a maximum peak power of  $P = 25$  TW at a pulse duration of  $\tau_L \approx 30$  fs. Therefore, LWFA for these experiments takes place in an intermediate regime where the first stage is dominated by self-modulated laser wakefield acceleration (SM-LWFA) and is then followed by the blowout regime. The second stage is reached by a transversal and longitudinal compression of the pump pulse, which was directly observed for the first time and will be discussed in Chapter 4.

### 2.11.1 Self-modulated laser wakefield acceleration

If the pulse duration of the laser pulse is longer than one oscillation period of the plasma wave then the wave excitation is not at maximum efficiency. However, if the laser pulse's power is above a critical value, which is equivalent to the power for relativistic self-focusing, cf. Eq. (2.23), an instability can lead to a modulation in the pulse's longitudinal intensity profile. The instability is stimulated Raman forward scattering, which was discussed in Section 2.7. The SRS-F starts from noise in the electron density, which is most prominent at the plasma frequency. These ripples can periodically change the group velocity of the laser pulse leading to a modulation in the intensity profile. This give rise to a longitudinal variation in the ponderomotive force, which pushes the electrons out of regions of high intensity and further increases the amplitude of the longitudinal density modulation in the plasma. The modulation of the laser's intensity profile leads to the growth of spectral side bands  $\omega_0 + n \cdot \omega_p$ ,  $\omega_0 - n \cdot \omega_p$ , with  $n$  being an integer, as the laser pulse is scattered at the plasma wave. Eventually an initially long laser pulse is transformed into a pulse train with individual pulses separated by  $\lambda_p$ , which now can efficiently excite a plasma wave.

This acceleration regime was extensively investigated in the past [58, 72, 73] but is still relevant if the laser pulses are not matched to the plasma density, which is usually the case for sub 60 TW Ti:sapphire laser pulses without external guiding schemes. In the case of slightly unmatched laser pulses,  $c\tau_L \geq \lambda_p$ , SRS-F plays a distinct role in the early stages of the laser pulse's evolution and could lead to pulse splitting into two pulses separated by  $\lambda_p$  [52].

### 2.11.2 Blowout regime

So far, the interaction of the short laser pulse with an underdense plasma was treated with a simple fluid model that is valid as long as the particle trajectories do not cross. However, such crossings will occur as soon as nonlinearities can no longer be neglected and in particular for multi-dimensional plasma oscillations. Even very weak nonlinearities can cause trajectory crossing as they induce shifts in the electron's oscillation frequencies that are dependent on initial position, which in turn results in out of phase oscillations of the particles relative to each other. Consequently, the cold fluid model can only be valid for a limited spatial region or alternatively for a finite time. This can be fulfilled for weak drivers, i.e., the driver causes only small density perturbations compared to the ambient density, and for short drivers for regions in proximity to the driver. If the trajectory crossing occurs close to the driver then the model breaks down and a new model that includes the blowout is necessary. In the quasi-static approximation (Section 2.8.1, [47]), the fields in the wake only depend on the longitudinal variable  $\xi \equiv ct - x$ , while the phase velocity of the wake is *essentially*  $c$ . This is justified by the different time scales of the involved processes and valid as long as  $\frac{\omega_0}{\omega_p} \gg 1$ , and as long as the laser spot size  $w_0$  is on the order of the plasma skin depth  $c/\omega_p$ . The three distinct time scales in the blowout regime are: (a) the plasma wakefield oscillation  $\omega_p^{-1}$ , (b) the high frequency laser oscillation  $\omega_0^{-1}$  and (c) the laser envelope evolution  $\frac{\omega_0}{\omega_p} \omega_p^{-1}$  [29, 47].

In the case of the high intensity limit ( $a_0^2 \geq 1$ ), the wakefield structure can differ significantly from the sinusoidal form in the weakly relativistic limit, cf. Figure 2.4a. In addition to wave steepening and period lengthening, which occur in the 1-D limit as well, cf. Figure 2.4b, the radial structure of the wave can be further modified due to additional nonlinear effects. One of the results is that the wave fronts of the plasma wave can be curved, as it can be seen in Figure 2.6. The farther the distance behind the driver, the more pronounced the curvature becomes, as a result of the plasma frequency being lower on-axis than off-axis. The increase in wavelength due to the relativistic mass increase of the plasma electrons averaged over one laser period can be approximated by  $\lambda_{\text{NLP}} = \sqrt{\gamma} \lambda_p = (1 + a_0^2/2)^{1/2} \lambda_p$ . This is in good agreement with the results from the simulation and the experiment in Chapter 4.

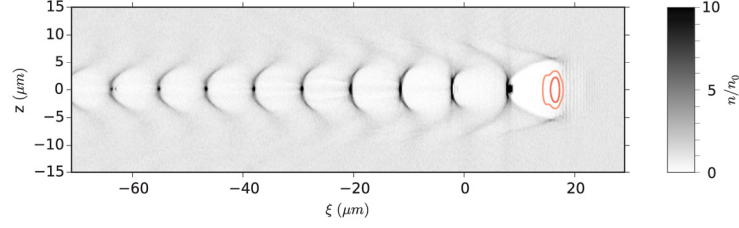


Figure 2.6 | Snap shot of the electron density distribution (grey scale) and laser intensity (red isocontours) from 3-D PIC simulation with  $n_e = 1.7 \cdot 10^{19} \text{ cm}^{-3}$ ,  $w_0 = 9.5 \text{ } \mu\text{m}$ ,  $a_0 \approx 1.1$ . Details are given in Sec. 4.8.

This high-intensity 3-D regime has been referred to as the *blowout*, *bubble*, or *cavitation* regime. In addition to electron cavitation, a fraction of the plasma electrons can become self-trapped in the ion cavity and can be accelerated to high energies. This regime of complete expulsion of the plasma electrons from a region centered around the axis has been studied for a laser driver by Sun [46] and later using 3-D PIC simulations by Pukhov and Meyer-ter-Vehn [74]. The blowout region of the wake is characterized by a longitudinal accelerating field, which does not vary radially but only linearly as a function of distance behind the driver, and a transverse focusing field that increases linearly with the radial distance. This regime can have beneficial accelerating properties: the normalized emittance of an accelerated electron bunch will be preserved when it experiences such a focusing field with linear radial dependence.

To reach the blowout-regime, the laser spot size has to be matched to the laser power  $P$  and the plasma density  $n_e$ . At this point, it is important that the ponderomotive force only extends out to the boundary of the laser pulse. If the laser is focused to a spot smaller than the matched spot size, the electrons near the axis are blown out too quickly while the outer electrons hardly experience the ponderomotive force at all. This generates a very wide sheath and due to the small spot size, the laser pulse will not be guided. However, if the spot size is much larger than the matched size, the electron expulsion will not be complete due to the reduced intensity. Still, relativistic self-focusing will occur and the back of the pulse will be focused. To obtain the matched spot size, the ponderomotive force of the laser pulse  $k_p \nabla a_0^2 / \gamma \sim a_0 / (k_p r_b)$  has to balance the electrostatic force of the ion channel  $E_r \sim k_p r_b$  [46]. This is achieved when the laser spot size matches the blowout radius  $r_b$ . This condition leads to

$$k_p r_b \cong k_p w_0 \sim 2\sqrt{a_0}, \quad (2.37)$$

which was verified by PIC simulations [29] by adding 2 as a correction factor. For laser drivers, the blowout regime can be reached in several ways, including the long pulse self-modulated regime [73] and the short-pulse LWFA regime [16-18].

## 2.12 Acceleration limits

The maximum field that can be supported by a laser driven plasma wave has been discussed in the previous chapter. However, current laser plasma accelerators cannot be extended infinitely. The final electron energy is determined by the interplay between the accelerating field and the distance over which this field can be sustained.

### Diffraction

A first limiting effect is the diffraction of the laser pulse. High laser intensities are required to generate high electric fields in the plasma wave. Outside the Rayleigh range  $Z_R = \pi w_0^2 / \lambda_0$ , the laser spot size increases quickly, which reduces the laser intensity. Self-focusing (Section 2.5) can increase this length but only up to several  $Z_R$ . In an experiment, the acceleration length can be extended by external guiding structures using a preformed plasma channel, e.g., formed by a longitudinal discharge fired through a gas nanoseconds before the arrival of the main laser pulse [75].

### Laser depletion length

A significant fraction of the laser pulse's energy is required to form and to sustain the plasma wave. Here, the laser's front interacts with the plasma electrons while the back of the pulse resides within the ion channel where the electron density is much lower, hardly influencing this part of the laser pulse. The interaction of the laser with the plasma wave changes the pulse envelope, *etching* away the pulse starting from its front with a velocity  $v_{\text{etch}} = c\omega_p^2 / \omega_0^2$  [48]. Therefore, the laser pulse will be depleted after a length

$$L_{\text{deph}} = \left( \frac{\omega_0}{\omega_p} \right)^2 \frac{c\tau_L}{a_0^2} \quad \text{for } a_0 < 1 \text{ [45]} \quad (2.38)$$

$$L_{\text{depl}} = L_{\text{etch}} = \frac{c}{v_{\text{etch}}} c\tau_L = \left( \frac{\omega_0}{\omega_p} \right)^2 c\tau_L \quad \text{for } a_0 > 1 \text{ [29]} \quad (2.39)$$

while the front of the laser pulse moves back due to the etching. It is noteworthy that the etching velocity is independent from  $a_0$ . When the laser has lost a substantial fraction of its energy, the plasma wave amplitude will decrease and the acceleration process is terminated. The point of depletion can be characterized by the sharp front of the laser pulse and the formation of a density spike. This will be shown in more detail in Chapter 4 by simulations as well as in experimental shadowgrams.

## Dephasing length

Electrons can be accelerated by the plasma wave to velocities very close to the vacuum speed of light. The plasma wave, however, still propagates with the group velocity of the laser, which is slightly, but significantly, less than  $c$  for typical laser and plasma parameters. Thus, the electrons will be faster than the plasma wave after the first part of the acceleration and eventually enter the decelerating part of the plasma wave. This process of dephasing in the blow out regime can be calculated by estimating the distance it takes the electrons in the lab frame to advance  $r_b = \lambda_p/2$  with respect to the plasma wave.

$$L_{\text{deph}} = \frac{\lambda_p^3}{\lambda_0^2} \quad \text{for } a_0 < 1 \text{ [45]} \quad (2.40)$$

$$L_{\text{deph}} \cong \frac{c}{c - v_\phi} r_b \cong \frac{4 \omega_0^2 \sqrt{a_0}}{3 \omega_p^2 k_p} = \frac{2 \lambda_p^3}{3\pi \lambda_0^2} \sqrt{a_0} \quad \text{for } a_0 > 1 \text{ [29]} \quad (2.41)$$

Hence, the dephasing length is longer for a lower plasma density. Thus, lower densities are needed to reach the highest electron energies. A comparison of depletion and dephasing for different regimes is shown in Figure 2.7. For  $a_0 \geq 5$  and matched beam parameters the depletion and dephasing length are equal, while for smaller intensities the energy gain is limited by dephasing. In principle, dephasing can reduce the energy spread of an accelerated electron bunch, which has been injected over a longer period [29]. For a high conversion efficiency,  $\eta_{\text{wf}}$ , from laser pulse to plasma wave, the depletion length should match the dephasing length. However, it needs to be taken into account that injection only occurs after a certain propagation distance of the plasma wave, not immediately, hence,  $L_{\text{depl}} > L_{\text{deph}}$  is advised. Nevertheless, the efficiency reveals the scaling in the blow out regime for optimal conditions for  $1 \leq a_0 \leq 5$

$$\eta_{\text{wf}} = \frac{L_{\text{deph}}}{L_{\text{depl}}} \cong \frac{4}{3\pi} \sqrt{a_0}. \quad (2.42)$$

## Maximum energy gain

The maximum energy gain,  $\Delta E$ , of the electrons in the wakefield is determined by the acceleration length and the electric field. Since  $L_{\text{deph}} \leq L_{\text{depl}}$  for typical parameters ( $a_0 \approx 1 - 2$ ),  $\Delta E$  is given by Esarey *et al.* [45] in practical units

$$\Delta E = eE_{\text{acc}} L_{\text{deph}} \approx 400 \frac{I [\text{W/cm}^2]}{n_e [\text{cm}^{-3}]} \quad (2.43)$$



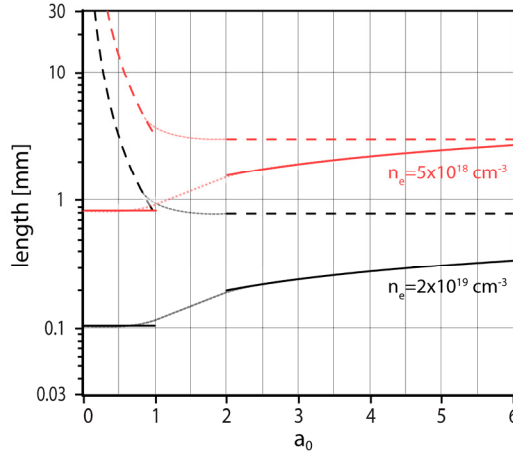


Figure 2.7 | Dephasing length (solid lines) and depletion length (dashed lines) for different densities using Eq. (2.38) and Eq. (2.40) in the low intensity ( $a_0 < 1$ ) limit and Eq (2.39) and Eq. (2.41) for  $a_0 > 2$ . The dotted curves are interpolated values for the intermediate regime.

## Beamloading

So far, the effect of the electrons loaded into the plasma wave on the wave's electric field distribution has been neglected. The maximum energy gain derived above is true only if a small number of electrons are injected into the plasma wave. However, if the injected charge is significant, which is of course desirable for an accelerator, the longitudinal electric field of the plasma wave will be modified. This effect has been studied in the blowout regime with great detail in theory [76] and in experiments [77]. Generally, electrons that are accelerated in the plasma wave will be out of phase with the electrons that constitute the plasma wave. Thus, their electric field will counteract the fields of the plasma wave and reduce the accelerating field. The threshold charge was given by Tzoufras *et al.* [76]:

$$Q_{\text{tr}}[\text{nC}] \times E_0[\text{GV/m}] \cong 0.456 \cdot (k_p r_b)^4. \quad (2.44)$$

For the laser and plasma parameters considered here ( $n_e = 1.65 \cdot 10^{19} \text{ cm}^{-3}$ ,  $E_0 = 510 \text{ GV/m}$ ,  $r_b = w_0 = 5 \mu\text{m}$ ) the beamloading threshold is 200 pC; therefore, the energy distribution of the accelerated electrons broadens proportionally to the total charge above this value.

## 2.13 Scaling laws and matching conditions

As seen from the considerations above, analytical expressions for important plasma wake-field quantities have been derived in the 1-D limit. However, the transition to realistic 3-D geometries can change these expressions significantly. In recent years, particle-in-cell simulations have been used to understand and interpret experimental results. Based on

such simulations, various groups have derived scaling laws to predict the optimum acceleration conditions and the accelerator's output for given parameters. From various scaling theories, two have proven to be exceptionally useful. They have both come to the conclusion that the acceleration is optimized when the focal spot radius,  $w_0$ , and the duration  $\tau_L$  of the driving laser pulse obey  $c\tau_L \leq w_0$  and when the focal spot size is related to the plasma density and normalized vector potential via  $k_p w_0 \approx \sqrt{a_0}$ . However, the final scaling laws differ significantly.

### 2.13.1 Gordienko Pukhov (GP) scaling

The scaling theory developed by Gordienko and Pukhov [78] is based on similarity theory. They introduced a similarity parameter  $S = \frac{n_e}{a_0 n_c}$ , assuming  $S \ll 1$  and  $a_0 \gg 1$ . These rather extreme parameters lead to a complete cavitation of the first plasma wave oscillation and form a perfectly spherical bubble. All subsequent plasma oscillations are suppressed due to wave breaking after the first plasma oscillation. The electron acceleration is then limited by depletion of the laser pulse only,  $L_{\text{depl}} = a_0 \frac{\omega_0^2}{\omega_p^2} c\tau_L$  and high conversion efficiencies from laser to electron energy of  $\eta = 20\%$  can be achieved. Expressions for the peak electron energy  $E_{\text{mono}}$  and accelerated charge  $Q$  are given by

$$E_{\text{mono}} \approx 0.65 m_e c^2 \sqrt{\frac{P}{P_R} \frac{c\tau_L}{\lambda_0}} \quad (2.45)$$

$$Q [\text{nC}] \approx 1.4 \frac{\lambda_0 [\mu\text{m}]}{0.8} \sqrt{\frac{P [\text{TW}]}{100}} \quad (2.46)$$

Here,  $P_R = 8.5$  GW and  $P$  is the power of the laser pulse. To reach this so called *bubble*-regime a threshold power has to be surpassed.

$$P > P_{\text{bubble}} = \left( \frac{\tau_L [\text{fs}]}{\lambda_0 [\mu\text{m}]} \right)^2 30 \text{ GW}. \quad (2.47)$$

Solving these equations for JETi 40 parameters using  $\tau_L = 30$  fs, a power of  $P = 41$  TW would be required, which is higher than the typically available power of 25 TW. However, this scaling does not predict the outcome for arbitrary laser and plasma parameters but rather predict how the output parameters can be scaled once a stable regime has been found. Current LWFA experiments are far away from the derived efficiency of 20 % and the highest efficiency is only achieved if electron bunches with a very broad energy distribution are generated. While numerical simulations often overestimate the obtained

charge of LWFA experiments, this discrepancy could also be due to the fact that the numerical prefactors in the above equations were obtained for  $a_0 \geq 10$  while LWFA experiments have only been carried out up to  $a_0 = 4$ , which is already difficult to reach with state-of-the-art laser systems and adequate focusing.

### 2.13.2 Lu scaling

A different and quite successful scaling theory, which is also valid for  $2 \leq a_0 \leq 4$ , was presented by Lu *et al.* [29]. Here, a more phenomenological approach based on the basic underlying processes, i.e., wake excitation, laser pulse evolution/depletion, dephasing, and beamloading, was used. In their theory,  $L_{\text{deph}}$  and  $L_{\text{depl}}$  are matched, see Figure 2.7, which is beneficial for the final electron energy spread as already mentioned before. The maximum electron energy and charge derived by this scaling theory are given by

$$\Delta E \approx \frac{2}{3} m_e c^2 \left( \frac{\omega_0}{\omega_p} \right)^2 a_0 \quad (2.48)$$

$$Q[\text{nC}] \approx 0.4 \frac{\lambda_0[\mu\text{m}]}{0.8} \sqrt{\frac{P[\text{TW}]}{100}} \quad (2.49)$$

respectively. To derive these scaling laws,  $a_0 \geq 2$  was assumed as well as  $c\tau_L \leq w_0 \cong 2\sqrt{a_0}c/\omega_p$ , which can be realized in most experiments today. Applying Lu's scaling to the parameters of the experiments described in Chapter 4 and 5, we find about  $\Delta E \approx 60$  MeV for  $a_0 = 1.7$  and  $n_e = 1.65 \cdot 10^{19} \text{ cm}^{-3}$ . This result from Lu's scaling underestimates the experimental results presented in Chapter 4.

An analysis by Mangles [79] has shown that for various experiments the maximum energy seemed not to be dependent on  $a_0$  and the best match between experimental data and the model is given for  $a_0 = 3$ . One possible explanation is that in experiments  $a_0$  is commonly calculated from the laser pulse's energy, pulse duration and focal spot size in vacuum; however, the laser pulse can evolve significantly in a plasma due to self-focusing, self-compression and photon acceleration, cf. Section 2.5 and 2.6. Since in an actual experiment the electron density is optimized for given laser pulse parameters,  $a_0 = 3$  seems to be a threshold for electron trapping.

Comparing these two scaling laws for higher laser powers for which they were derived, the results differ drastically. For the JETi200 laser system with  $P = 230$  TW and  $\tau_L = 17$  fs the preconditions for both scaling laws are met. On one hand, Lu's scaling predicts a total charge of only one third when compared to GP's scaling. On the other hand, the peak

energy is five times higher,  $E_{\text{Lu}} \approx 1.0$  GeV, while  $E_{\text{mono,GP}} \approx 350$  MeV. Considering external guiding the discrepancy in the peak energy becomes even more severe. Optimal guiding would require a channel depth  $\Delta n_c/n_e = 4/\left(\frac{k_p}{w_0}\right)^2 \cong \frac{1}{a_0}$  [29]. A laser power just slightly above the critical power for self-focusing will result in an energy gain on the order of  $\Delta E = 6$  GeV.

It should also be noted that these two theories were developed for the self-injection regime (see Section 2.14.1). However, from an experimental viewpoint this regime is rather unstable. Improving the energy stability or the possibility to actively control the electron energy was so far only achieved at the expense of the accelerated bunch charge [80, 81].

## 2.14 Electron trapping and injection

To conclude the discussion about the characteristics of the plasma wakefield accelerator it is obvious that they are favorable to be used as an electron accelerator. The outstanding feature of a LWFA is its compactness. This, however, makes it challenging to inject the electrons into the correct phase-space volume of the wakefield. External injection turns out to be extremely challenging since the small spatial, temporal and velocity acceptance of a plasma wave already calls for electron pulses with a duration on the order of a few fs, which need to be focused down to micrometer size to get efficient coupling. Such electron pulses are available from test accelerators only and have sub pC charge [82]. An alternative route, which circumvents this challenging synchronization, is to use internal injection mechanisms triggered by the driving laser pulse itself. Using long laser pulses ( $> 300$  fs) to form a SM-LWFA, the SRS-F instability was used to enhance the plasma wave amplitude up to the point of wave breaking and to generate electron bunches with a broad spectrum ( $\Delta E/E = 100\%$ ), i.e., a nearly thermal distribution [58]. Using short laser pulses with  $c\tau_l \approx \lambda_p/2$  drives the plasma wave to a much higher amplitude since plasma heating is much weaker in this regime. This leads to higher electric fields approaching the cold wave breaking limit and consequently higher accelerated electron energies [83]. However, the electron spectrum still shows a thermal distribution and temperature dependent divergence. To produce electron bunches with a narrow energy spread and good collimation, it is important to reach the blowout/bubble regime. As described in the previous sections this requires matched conditions between the focal spot size of the laser pulse, its duration and the plasma density. Achieving these conditions has led to the first generation of quasi-monoenergetic electron bunches self-injected into the plasma wave and accelerated to energies in excess of 100 MeV [16-18]. To improve the quality of the electron bunch it is favorable to make the injection independent from the driver beam. This can be done by either using a secondary laser beam in a colliding pulse scheme [80] or by using a sharp density transition [81] to inject electrons at a well-defined position in

space for a very short time resulting in well collimated and narrow energy spread ( $\Delta E/E = 1\%$ ) electron beams. For the laser parameters used in the experiments described in Chapters 4 and 5, self-injection is the most favorable process and will be described in the following section in more detail.

### 2.14.1 Self-injection and wave breaking

In 2002, by using simulations it was shown that LWFA are capable of producing monoenergetic electron bunches [74]. Here, an ultra relativistic laser pulse with  $a_0 \gg 1$  propagates through a homogeneous plasma and drives a high amplitude plasma wave. The ponderomotive force of the laser expels all electrons from its path while the ions remain stationary. The initially expelled electrons are attracted by the positively charged region behind the driving laser pulse. These electrons move on trajectories forming a spherical bubble with the diameter,  $d_b = 2r_b$ , and the plasma wave breaks already after one oscillation for laser pulses described in [74]. Such high power laser pulses are still not available and experiments are typically carried out with  $a_0 = 1 \dots 4$ . In this case, the plasma wave does not fully break after the first period, but rather is trailed by a number of plasma wave periods with reduced amplitude [21]. The shape of the bubble depends on the intensity of the laser and for  $a_0 > 2$  it is almost spherical with a thin electron sheath surrounding it. In the center of the bubble, the electric potential achieves its maximum value while it is at a minimum in the sheath, especially at the back of the bubble.

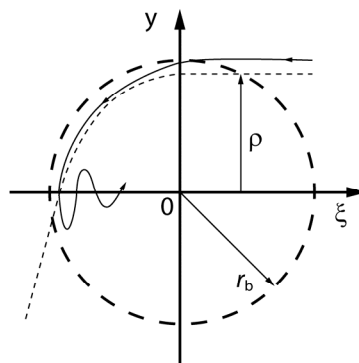


Figure 2.8 | Trajectory of a trapped electron (solid line) and untrapped electron (dashed line) and the border of the bubble (long dash line).

Depending on the electron's initial distance  $\rho$  from the laser axis before the laser pulse passes, background electrons are either expelled, for  $\rho < r_b$ , or not sufficiently attracted, for  $\rho > r_b$ , see Figure 2.8.

They can be trapped for  $\rho = r_b$  where the electrons move along the bubble's boundary, where they experience a strong electric field attracting them towards the center of the bubble. Yet they do not have the correct velocity, which has to match the phase velocity of the bubble to get injected. However, via scattering at the dense sheath at the back of

the bubble some electrons can gain enough energy to reach a sufficiently high forward velocity to catch up with the bubble. The electrons are trapped, if the following inequality derived by Kostyukov *et al.* [84] is fulfilled:

$$\frac{\gamma_\phi}{R} \leq 1/\sqrt{2} \quad (2.50)$$

with  $R = k_p r_b$  the normalized bubble radius and  $\gamma_\phi \approx \sqrt{n_c/3n_e}$  [48] being the phase velocity of the plasma wave. For the laser pulses and focusing geometries relevant in this thesis, the phase velocity of the plasma wave is too high and the bubble radius too small; therefore, no electrons should be self-injected.

A very similar model was developed by Thomas [85] and applied by Mangles *et al.* [86]. In this model, electrons are trapped if the bubble radius is larger than

$$k_p r_p > 2\sqrt{\ln(2\gamma_\phi^2) - 1}. \quad (2.51)$$

This radius is smaller than the one predicted by Kostyukov *et al.* and should lead to injection for the experimental parameters used here. The critical power required for self-injection can be derived if the equation for pulse compression Eq. (2.24) is used and the interaction length is only limited by the pulse depletion length:

$$\frac{\alpha P}{P_c} > \frac{1}{16} \left[ \ln\left(\frac{2n_c}{3n_e}\right) - 1 \right]^3 \quad (2.52)$$

with  $\alpha$  being the ratio of the pulse energy within the focal spot to the total energy.

Beside the different outcomes of the two models, both have considered a static bubble; however, simulations have shown that the bubble can also undergo longitudinal [87] and transverse [88] expansion or shortening and thus trigger injection. If the bubble expands sufficiently fast as the electrons travel around it, they are exposed to the strong fields at the back of the bubble for longer times, which increases the probability of injection.

### 3. Experimental setup

In this chapter, the basic setup for the experiments described in Chapter 4 and 5 is presented. A high intensity laser pulse is required to produce large amplitude plasma waves that support high electric fields. These were utilized to accelerate electron bunches to energies up to 200 MeV [32, 33, 89]. To gather insight into the interaction, a probe pulse backlights the laser plasma interaction from the side, while the interaction region is imaged onto a CCD sensor. Measuring the phase shift imprinted on the probe beam by means of optical interferometry allows one to deduce the electron density profile inside the plasma. To ultimately take snap shots of the laser plasma accelerator, very high temporal and spatial resolutions are required simultaneously. To meet these demands, a new probe beam line was installed at the JETi 40 laser system generating sub-6 fs probe pulses, which are synchronized to the pump pulse.

For the experiments discussed in this work, which use underdense plasmas created either from helium or hydrogen gas, the temporal intensity contrast of the pump pulse plays a critical role. For the JETi40 laser system the normalized intensity contrast is depicted in Figure 3.1. The three important quantities are (i) ps- pre-pulses, (ii) ASE background and (iii) the coherent contrast a few ps before the main pulse. Pre-pulses have to be of sufficiently low intensity in order to not ionize the gas. For the used pump pulse intensities of up to  $I_L \approx 1 \cdot 10^{19} \text{ W/cm}^2$  this implies a relative pre-pulse intensity below  $I_{pre} < 10^{-5}$  for

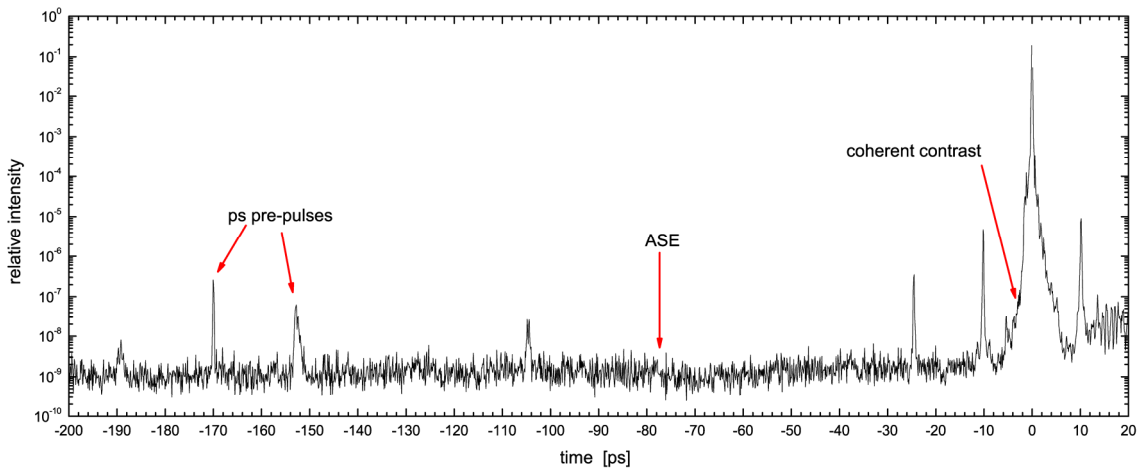


Figure 3.1 | Temporal intensity contrast of the JETi 40 laser. The measurement was done without pumping the final amplifier stage. It shows three distinct features covering the ns to fs range: ASE background, several short pre- and post pulses on a ps timescale and the coherent contrast, which forms a pedestal before the main pulse.

hydrogen and total energy of the ASE below a few  $\mu\text{J}$  to not trigger pre-ionization of the target gas and thus give rise to fluctuations in the electron beam pointing [90]. Finally, the

coherent contrast can have the strongest influence, since the ionization dynamic and a rather long duration ( $\sim 1$  ps) at high intensity ( $\sim 10^{15}$  W/cm<sup>2</sup>) can give rise to plasma instabilities, e.g., stimulated Raman scattering, as will be discussed in Chapter 5.

### 3.1 Experimental setup

The experimental results described in this thesis were obtained during several campaigns at the JETi 40 laser system. The laser parameters were kept constant with 750 mJ energy on target with a pulse duration of around  $30 \pm 3$  fs (FWHM) as measured by the SPIDER technique [91] and a central wavelength of  $\lambda_0 = 810$  nm. However, as it will be demonstrated in Section 5.2, the coherent contrast plays an important role in the ionization dynamics as well as in the injection process. Consequently, the temporal intensity contrast was carefully characterized during different experimental campaigns.

The basic setup of a LWFA experiment is shown in Figure 3.2. The pump pulses are focused by a  $f = 640$  mm (F/12) silver coated off-axis parabolic (OAP) mirror. The FWHM focal spot area was minimized to  $A = 90 \dots 130$   $\mu\text{m}^2$  containing 27 % of the total energy, thus yielding FWHM intensities of  $I_L = (4 \dots 6) \cdot 10^{18}$  W/cm<sup>2</sup> corresponding to a normalized vector potential of  $a_0 = 1.4 \dots 1.7$ . These different sizes and qualities of the focal spots can be attributed to the optical quality of various optical elements, which had to be exchanged during the campaigns, e.g., beam line mirrors, likely affecting the flatness of the wavefront.

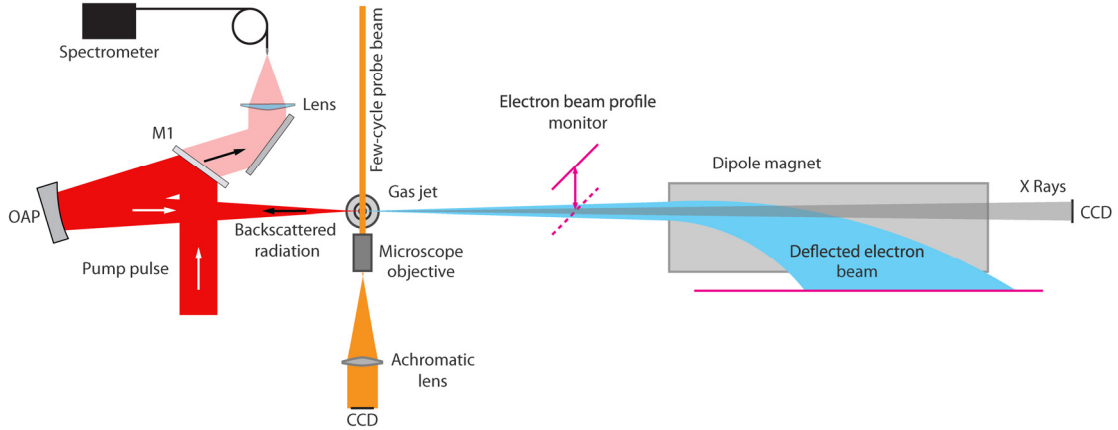


Figure 3.2 | Schematic for LWFA experiments. M1: mirror with high transmission for  $\lambda = (740 \dots 850)$  nm; OAP: silver coated off-axis parabolic mirror, Lens to focus the backscattered light into the fiber attach to the spectrometer.

Nevertheless, the matching conditions required to reach the blowout regime,  $k_p w_0 \cong k_p r_b = 2\sqrt{a_0}$ , are met at an electron density of  $n_e \approx 1.6 \cdot 10^{19}$  cm<sup>-3</sup>. Unfortunately, the laser pulse does not excite the plasma wave efficiently as  $c\tau_L \approx 10$   $\mu\text{m} > \lambda_p/2 = 4.2$   $\mu\text{m}$ . The low atomic number,  $Z$ , of the used gases ensures complete ionization



already by the rising edge of the laser pulse; thus the peak intensity interacts with a nearly homogeneous plasma in the longitudinal direction. The gas flow and gas density produced by the nozzle was analyzed before the experiments and optimum operating conditions like opening time of the valve and backing pressure were determined. The region above the nozzle, where the interaction with the main pulse occurs, was imaged onto CCD sensors. Applying two or three channel setups allows for taking interferometry and shadowgraphy or polarimetry data in a single shot. The images recorded contain both time-resolved and time-integrated information, which will be discussed in Chapter 4 and 5. For time-resolved measurements, a newly developed few-cycle probe beam line was used successfully for the first time to take detailed images of the plasma wave. The evolution of the pump pulse was characterized by recording the spectrum of the back scattered laser light. To do this, the back-reflected light leaking through the last mirror before the OAP was focused into a fiber coupled spectrometer (Ocean Optics HR4000), cf. Figure 3.2. The steering mirrors, cf. (M1), have a high reflectivity of  $> 99.5\%$  in the range of  $\lambda = 740 \dots 850$  nm, hence, only red or blue shifted radiation outside this region could be detected. Accelerated electron bunches were characterized by their pointing and divergence with a scintillating screen. The scintillating screen could also be removed allowing an electron spectrometer to characterize the energy distribution of the accelerated electrons. The spectrometer consists of a set of dipoles and was already characterized [92] to cover an energy range of 10 MeV – 240 MeV. In the second campaign, another newly developed spectrometer was used. It features a high spectral resolution of  $\Delta E/E < 2\%$  over the whole energy range from 3 MeV up to 1 GeV. The imprints of the electron bunches on the scintillation screens are imaged onto CCD sensors. The intensity signals taken by the imaging systems are absolutely calibrated, which allowed one to derive the charge of the electron bunches when using absolutely characterized scintillation screens (Kodak Bio-max, [93]). A CCD detected the accompanying X-ray radiation from the electrons carrying out wiggling motion in the transverse wakefields. The characterization of this so called *betatron radiation*, especially its spectrum, source size and polarization state can reveal information about injection mechanisms and the electron trajectories inside the plasma. Although these measurements were carried out during the same experimental campaigns as described in this thesis, they are not discussed here. A more detailed analysis of the results from these measurements is given in the PhD thesis by M. Schnell [94].

## 3.2 Supersonic gas jet targets

To utilize the repetition rate of 10 Hz of the JETi laser system a replenishable target is required. This was realized by using a solenoid valve (series 99, Parker Inc.) producing a pulsed helium gas jet as a target. The opening time was selected to be 4 ms since the flow

reaches a steady state just after 2 ms. Longer opening times reduce the effective repetition rate below 1 Hz as the vacuum system of the target chamber is not capable of keeping the pressure below  $10^{-3}$  mbar. Conical nozzles with an exit diameter of 2.7 mm and 3 mm made from brass were used based on designs theoretically studied [95] and used successfully in other laboratories, cf. Figure 3.3a. Steep density gradients at the edge of the density distribution are characteristic for this type of supersonic nozzle, which are easier to manufacture than de Laval type nozzles but provide a similar density profile. The gradients are largest directly above the nozzle exit and then get smoother farther away. The laser pulse produces a hot plasma during the interaction, which leads to etching of the nozzle and thus changes the density profile considerably. To avoid this etching, a shot height of 1.25 mm above the nozzle was chosen, which allowed reproducible conditions for more than 10000 shots. Applying a backing pressure of 25 bar at the nozzle resulted in a neutral density of  $n_{\text{He}} = (8.3 \pm 0.3) \cdot 10^{18} \text{ cm}^{-3}$  for helium gas, see Figure 3.3b. The gas density was measured via tomography [96] in a setup, which was built during the master thesis of B. Landgraf [97]. The gas jet was rotated in  $4^\circ$  steps to a total range of  $180^\circ$ . The 45 recorded projections allowed the calculation of the density profile without assuming any kind of rotational symmetry. In the experiments described here, hydrogen and deuterium were also used. Assuming full ionization, all three gases should yield the same number of electrons; however, taking the hydrodynamic gas flow into account, the electron density will be slightly different for each gas. The sound velocity, which is characteristic for the velocity in the nozzle's throat, is higher for hydrogen ( $v_{\text{S,H}_2} = 1280 \text{ m/s}$ ) than for helium ( $v_{\text{S,He}} = 981 \text{ m/s}$ ) and deuterium ( $v_{\text{S,D}_2} = 890 \text{ m/s}$ ). Hence the effective neutral density and hereby the electron density should be reduced by the ratio of the velocities to  $v_{\text{S,H}_2}/v_{\text{S,He}} = 1.3$  and  $v_{\text{S,H}_2}/v_{\text{S,He}} = 1.44$  at the same backing pressure and nozzle diameter. This requires a higher backing pressure for hydrogen to reach the same electron densities as helium or

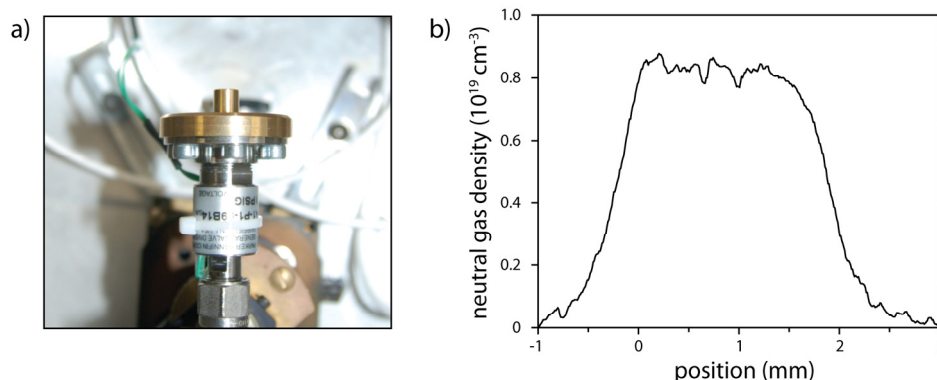


Figure 3.3 | Supersonic gas jet targets. a) Valve (Parker Series 99) with custom made brass nozzle. b) Retrieved neutral gas density profile with helium gas from a tomographic measurement at a background pressure of 25 bar, 1.25 mm above the nozzle exit (image courtesy of Björn Landgraf).

deuterium. At the same time, the pumping rate for hydrogen is less due to its lightness, which causes a higher pressure in the target chamber assuming a constant shot rate. Due to the turbulent nature of supersonic flows and depending on the backing pressure, supersonic shocks can be generated inside the nozzle. These shocks can arise from imperfections in the manufacturing process of the nozzle, where sharp edges can remain. Depending on the position where these instabilities occur, they can lead either to disintegration of the plasma wave or to injection of electrons into the wakefield. Using razor blades to generate these shock fronts in a controlled manner has led to a controlled point of injection thus tuning the energy of the accelerated electron bunch [81]. Unfortunately the spatial resolution of the tomography setup is not high enough to resolve these shocks and any appearance can only be detected in the LWFA experiment itself, e.g., by shadowgraphy.

### 3.3 Electron beam diagnostics

The accelerated electron bunches are detected by means of scintillating screens (Kodak Biomax). These screens are inserted into the electron beam to measure the electron beam profile at high repetition rates. From there, secondary properties of these bunches like the divergence and pointing can be calculated. Up to four layers of aluminum foil, each 15  $\mu\text{m}$  thick, are used to shield the screen from incoming laser radiation. The electron bunch suffers small-angle scattering when passing through the foil but the profile does not change significantly after the very short drifting distance of  $\ll 1$  mm between the foil and the scintillator screen. The backside of the screen was imaged using an F/1.4, 50 mm objective onto a CCD (Allied Vision, Pike F-421). Depending on the brightness of the emission, the aperture was reduced to F/8 or to F/16. Due to the aberrations of the imaging objective and the geometry of the scintillator screen, the recorded images are distorted. Before the beam profiles were analyzed, all images were post processed and corrected for distortions. Removing the scintillation screen allowed the electron bunches to enter the dipole spectrometer, described in the master thesis of F. Budde [92]. However, the relative energy resolution  $\Delta E/E$  in the range from 60 MeV to 240 MeV was quite poor and even when using a two millimeter wide slit in front of the spectrometer, it was still 30% at the maximum energy. Additionally, as the electrons pass through unshielded fringe fields when entering the spectrometer, a focusing force was exerted on the electron bunch and so the profile in the transverse direction is altered.

As it will be demonstrated in Chapters 4 and 5, the combination of the short pulse duration of the upgraded JETi 40 and the use of longer focal length OAPs have increased the maximum achievable energy beyond 200 MeV, which is the radiation safety limit for the JETi 40 laboratory. Thus, the length of the gas jet was limited to stay below this boundary. To overcome the drawbacks of the above mentioned spectrometer, a new spectrometer

was designed by M. Leier. It covers an energy range from 3 MeV to 1 GeV with a spectral resolution of  $\Delta E/E \leq 2\%$  over the full range, see Figure 3.4. Both spectrometers were absolutely calibrated using the results from Buck *et. al* [93] and the calibrated Kodax Bio-max scintillator screens. Calibrating the sensitivity of the imaging system by taking into account the aberrations of the imaging system, e.g., vignetting and the directional emission characteristic of the scintillator screen, allows one to calculate the total accelerated charge from the recorded brightness on the CCD.

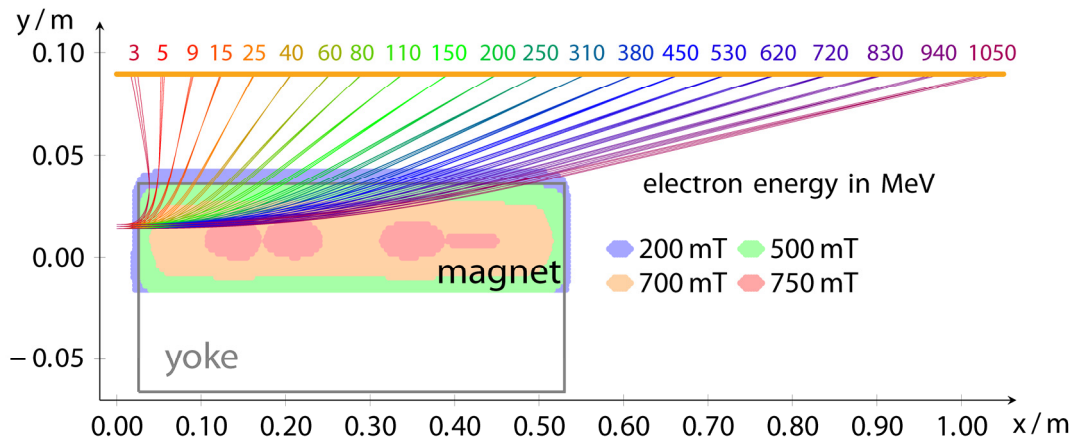


Figure 3.4 | Design of the high-resolution electron spectrometer. Energy dispersion for different energies. Images courtesy of Maria Leier.

### 3.4 Comparison of plasma imaging techniques

In the following section, imaging techniques commonly used for laser plasma diagnostics, i.e., interferometry and shadowgraphy, are discussed. An aspect shared by the two techniques is that they generate projection data, namely information that is integrated along the direction of propagation of the probe beam. Thus, this data is ray-averaged over the length  $l$  of the gas jet. However, in the case of shadowgraphically imaging (see below) the plasma wave, the small depth of field of the imaging setup and the fact that the image is predominantly formed by strong density gradients, which are only present in the very center of the interaction, reduce this length to only a few micrometers. To derive the electron density distribution, interferometry offers the most direct information and the interferograms are straightforward to analyze for true phase objects. Shadowgraphy reveals regions of high electron density gradients in the form of increased brightness modulations. To deduce the local electron density from the modulations, a solution of a Poisson equation with suitable boundary conditions is required [98].

### 3.4.1 Interferometry

In a typical interferometry setup, a laser beam is split into two parts. One traverses the phase object under investigation and the second beam acts as a reference. Depending on the used interferometer type the beam is split before the interaction into a probe beam and a reference beam or a shearing method is used and undisturbed parts of the beam after the interaction are used as a reference, e.g., in a Nomarski type interferometer [99]. In a Nomarski interferometer, one of the beams is tilted with respect to the other by a small angle before the beams are recombined, which introduces a phase difference that linearly increases in the direction of the tilt and results in a characteristic uniform fringe pattern. The investigated object imprints an additional phase shift on the probe beam, which results in a deformation of the fringe pattern. Using either Fourier methods [100] or wavelet analysis [101] gives the distribution of the phase  $\delta\phi(z, x)$  introduced by the object in the probe beam's path. It is common to assume a rotational symmetry to calculate the three dimensional distribution by means of an inverse Abel transformation. As most of the recorded phase shifts do not fulfil the symmetry requirement a more generalized approach was applied here [102]. For either the symmetrical or general case, the phase map is separated by the best symmetry axis  $z_0$  into two half-space phase maps  $\delta\phi^+(\zeta, x) = \delta\phi(z - z_0, x); z > z_0$  and  $\delta\phi^-(\zeta, x) = \delta\phi(z_0 - z, x); z < z_0$ . In the case of axial symmetry around the laser propagation axis  $x$ ,  $\delta\phi^+ = \delta\phi^-$ , the electron density distribution  $n_e(r, x)$  is computed as

$$n_e(r, x) = -n_c \frac{\lambda_{\text{pr}}}{\pi^2} \int_r^\infty d\zeta \frac{1}{\sqrt{\zeta^2 - r^2}} \frac{\partial}{\partial \zeta} \delta\phi^\pm(\zeta, x) \quad (3.1)$$

with  $\lambda_{\text{pr}}$  being the probe wavelength and  $n_c$  the critical density at this wavelength. In the case of significant deviations from axial symmetry the Abel inversion applied to an artificial profile obtained by symmetrization of either  $\delta\phi^+$  or  $\delta\phi^-$ , can lead to significant errors in the reconstruction of the density distribution. This also occurs when considering the average of the phase distributions  $\delta\phi_s = \frac{1}{2}(\delta\phi^+ + \delta\phi^-)$ . In this thesis a generalization of the Abel inversion algorithm was used, which can be applied to asymmetric interferograms with a phase difference up to  $\pi$ . The algorithm is based on a Legendre polynomial expansion of  $n(r, x, \theta)$  in the angular variable alone. In the case of well behaved angular dependence, e.g., no abrupt changes in  $n_e$ ,  $n_e$  can be expanded into a series of orthonormal Legendre polynomials and truncated after the second term:

$$n(r, x, \theta) = n_0(r, x) + n_1(r, x) \cos(\theta) \quad (3.2)$$

Defining a symmetric and anti-symmetric component of  $\delta\phi$  as  $\delta\phi_s \equiv \frac{1}{2}(\delta\phi^+(\zeta) + \delta\phi^-(\zeta))$  and  $\delta\phi_a \equiv \frac{1}{2}(\delta\phi^+(\zeta) - \delta\phi^-(\zeta))$ , respectively, results in the coefficients of the generalized Abel inversion:

$$n_0(r, x) = -n_c \frac{\lambda_{\text{pr}}}{\pi^2} \int_r^\infty d\zeta \frac{1}{\sqrt{\zeta^2 - r^2}} \frac{\partial}{\partial \zeta} \delta\phi_s(\zeta, x), \quad (3.3)$$

$$n_1(r, x) = -n_c \frac{\lambda_{\text{pr}}}{\pi^2} \int_r^\infty d\zeta \frac{1}{\sqrt{\zeta^2 - r^2}} \frac{\partial}{\partial \zeta} \left( \frac{\delta\phi_a(\zeta, x)}{\zeta} \right). \quad (3.4)$$

Although the computational effort is significantly higher for this method so is the physical insight, which will be presented in Section 5.2.3.

### 3.4.2 Shadowgraphy

Shadowgraphy is a technique used in experimental fluid mechanics and heat transfer as a tool for the visualization of flow. When a collimated beam traverses a field of varying refractive index, individual light rays are refracted and bent out of their original path. This leads to a spatial modulation of the light-intensity distribution with respect to the original intensity distribution on the detector. The resulting transverse intensity distribution  $I(x, z)$  in the plane of the detector at a distance  $l$  from the object is a shadow of the refractive index field. Assuming negligible diffraction effects, a small angle deflection and a thickness of the sample  $\Delta y \ll l$ , the transverse variation of the refractive index relates to the intensity distribution in the shadowgram as [103]:

$$-\frac{1}{l} \frac{I(x, z) - I_0}{I_0} = \left( \frac{\partial^2}{\partial x^2} + \frac{\partial^2}{\partial z^2} \right) \int_0^{\Delta y} \eta(x, y, z) dy \quad (3.5)$$

with  $\eta(x, y, z)$  being the refractive index distribution of the phase object. This governing differential equation of the shadowgraph process is a Poisson equation. With the exact knowledge of the boundary conditions, this equation can be solved and the refractive index field retrieved. However, in this thesis the focus is put on the imaged shadows of the plasma wave. The formation of the shadowgrams is more complicated as the phase object itself is moving across the object plane with nearly the speed of light, has internal structures with dimensions  $< 1 \mu\text{m}$  as well as a local  $\gamma$ -factor  $> 1$  for the associated electrons. It turned out that only a 3-D PIC simulation can provide a comprehensive view on the formation of the shadowgrams, which will be presented in Section 4.8.

## 3.5 Probing Laser-Wake-Field-Acceleration at the JETi40

Probing the laser plasma interaction of a LWFA gives insight into the acceleration process. Important plasma parameters such as the electron density distribution  $n_e$  in front of the pump pulse's peak are crucial for the interpretation of the results and are inevitably for any kind of simulation. In Section 3.2, the neutral gas density of the supersonic gas jets was measured; however, during the laser-plasma-interaction, the intensity evolution of the laser pulse and the ionization levels of the used gases determine the momentary electron density until eventually the gas is fully ionized. This temporal influence is important as the time at which the gas is ionized can either aid or hinder the acceleration process. Since the generated and heated plasma has different times to expand the pump pulse can either be guided in a waveguide structure [49], or the plasma has already expanded too much leading to a plasma density that is too low for an efficient electron acceleration. Therefore, it is necessary to measure the electron density distribution during the interaction via interferometry with a high temporal and spatial resolution. Small transient structures like the plasma wave are very challenging to detect with interferometry, since the relative phase shift of the plasma wave is too small. On the other hand, using shadowgraphy, it is possible to visualize these structures because the strong gradients in the plasma refract and deflect the probe beam and generate intensity modulations in the probe beam's profile, which is then imaged onto a CCD. The temporal changes of these phenomena at a fixed position in the gas jet are typically at or below the pulse duration of the pump pulse, hence a very high temporal resolution is required.

At the JETi40 laser system a number of probe beam lines are available. In this work, the focus is put on two in particular. The first uses probe pulses, which are stretched to  $\tau_{pr} = 80$  fs due to dispersion of a beam splitter and a beam line exit window. The pulses also have a central wavelength of  $\lambda_0 = 800$  nm with an energy up to several mJ [104]. The second beam line generates probe pulses with  $\tau_{pr} \leq 6$  fs at a central wavelength of  $\lambda_0 = 750$  nm and an energy up to 200  $\mu$ J [105]. Both take a fraction of the main pulse transmitted by a 99 : 1 beam splitter but shape the pulses differently as is described in the following section.

### 3.5.1 High energy probe beam line and imaging system

Using interferometry to record the phase shift of the probe beam requires a high-energy probe pulse to outshine any self-emission from the plasma channel, which has a negative impact on phase retrieval algorithms. Due to this considerations, the full beam after the beam splitter was used and its diameter was reduced by means of an reflective telescope. This leads to probe pulses with an energy of  $E_{pr} = 4$  mJ and a diameter of  $d = 8$  mm. The following optional dispersion compensating mirrors (DCM, Thorlabs, DCMP 175) allow

recompression of the probe pulses from 80 fs to a transform limited duration of 30 fs. A linear delay stage with a travel range of 300 mm allows variation of the relative delay between the pump and probe pulse within a window of 2ns. The smallest step size is 5  $\mu\text{m}$  corresponding to an effective delay step of  $\Delta\tau = 33$  fs. The interaction region, back-lighted with these probe pulses, is imaged onto a CCD using an achromatic F/2 objective with a long working distance, see Figure 3.5a. A two channel imaging system was built where channel 1 recorded a shadowgram and channel 2 recorded a Nomarski type interferogram [99], which was used to determine the electron density distribution. A magnification of 4.35 was chosen leading to a resolution of 1.7  $\mu\text{m}/\text{pixel}$  on the CCDs (basler pilot piA1900-32gm) in both channels, covering the whole interaction length of the pump pulse with the 3 mm long gas jet in a single shot. Exemplary images with helium gas for the two channels after 1 mm of laser propagation into the gas jet are shown in Figure 3.5. The intensity modulation in the left part of the shadowgram shown in Figure 3.5b is caused by ionized helium gas and refraction of the probe beam.

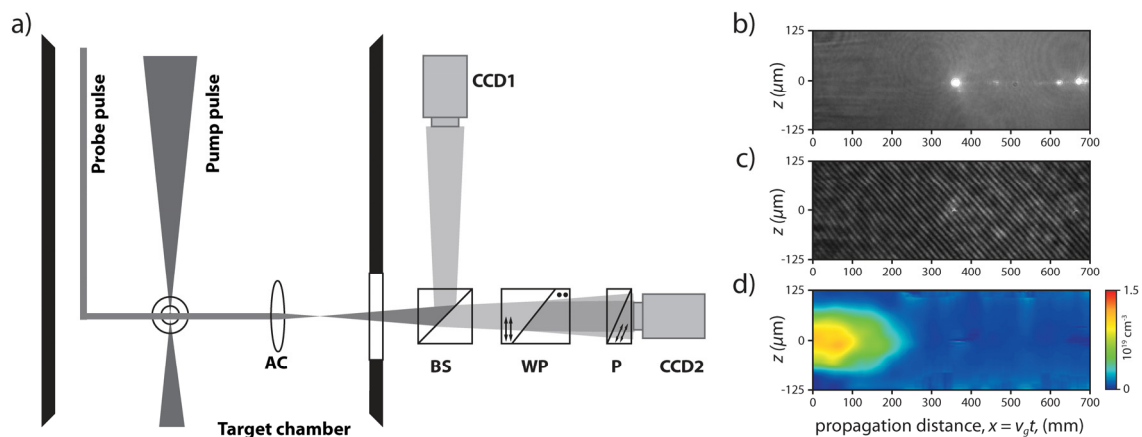


Figure 3.5 | Imaging setup for the 80 fs probe pulses. a) Setup: AC: achromatic lens; BS: beamsplitter; WP: Wollaston prism; P: polarizer; b) Shadowgram recorded by CCD1. c) Interferogram recorded by CCD2. The laser pulse is propagating from left to right in these images. d) Electron density distribution retrieved from c).

The pump pulse is propagating at the  $z = 0$  axis from left to right. Between  $x = 350 \mu\text{m}$  and  $x = 700 \mu\text{m}$  bright spots are visible. These localized sources of radiation can be attributed to scattered pump light at high-density gradients inside the plasma. The simultaneously recorded interferogram is shown in Figure 3.5c and the calculated electron density distribution in Figure 3.5d. Despite the short duration of the probe pulses used here, the temporal resolution is not high enough to resolve transient structures like the plasma wave generated by the pump pulse, even if they were recompressed to the initial pump duration of 30 fs. The plasma oscillation period associated with the electron density in Figure 3.5b is 28 fs, so a probe pulse of at least half the duration would be required to resolve the plasma wave.



### 3.5.2 Few-cycle optical probe beam line and high-resolution imaging

To efficiently excite plasma wakefields the duration of the pump pulse should be matched to the plasma density, i.e.,  $c\tau_L \approx \lambda_p/2$ . This would require a sufficiently high peak power to not only excite a plasma wave but also to inject electrons by wave breaking. Unfortunately, the peak power of JETi 40 is not sufficient. Therefore, a higher plasma density was chosen to reach wave breaking after a nonlinear evolution of the pump pulse. A typical length of the plasma wave's period, for the set of parameters used in the following experiments, is  $\lambda_p = 10 \mu\text{m}$ . As it is moving nearly with the speed of light, a short integration time of the camera or a short flash of light in the order of  $\tau_{\text{pr}} < \lambda_p/2c \approx 14 \text{ fs}$  would be necessary to get a sharp image. Even when using DCMs to compensate for the dispersion of the refractive optics, the pulses can only be compressed to the original pulse duration of about 30 fs due to the limited spectral bandwidth. In order to overcome this limitation, a few-cycle probe beam line was installed at the JETi40 laser system together with a high-resolution imaging system. The technique combining these two components was given the name *few-cycle microscopy* (FCM). For the generation of the probe pulses, the same 99:1 beam splitter was used and the transmitted pulse afterwards was reduced in size by means of a reverse bull's eye apodizing aperture, see Figure 3.6. By using only the central part of the laser beam, the overall beam quality was improved and pointing fluctuations reduced. The laser pulses were compressed by a set of DCMs to 30 fs and subsequently focused into a hollow core fiber filled with argon, a common technique at fs-laser systems

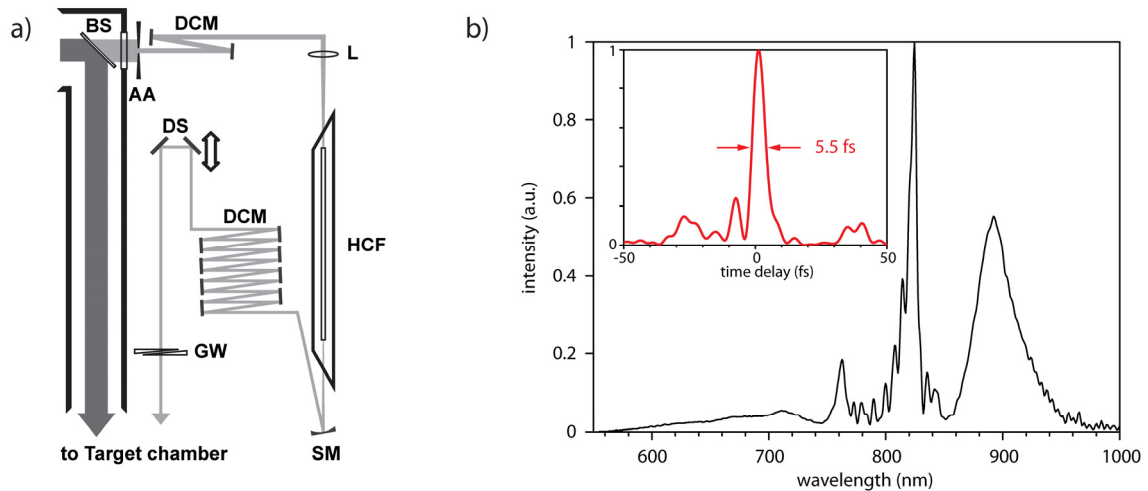


Figure 3.6 | Setup of the few-cycle probe beamline. a) BS: beam splitter, AA: apodizing aperture, DCM: dispersion compensating mirrors, L: lens, HCF: hollow core fiber filled with argon gas, SM: spherical mirror, DS: delay stage. b) Spectrum of the probe pulses (black) and pulse duration (inset, red).

with kHz repetition rates [30]. The energy before the fiber was 700  $\mu\text{J}$  with an overall transmission through the fiber of 60 %. The self-phase modulation (SPM) in the gas gen-

erated a white light spectrum spanning over more than one octave. Finally, DCMs supporting a bandwidth of more than 300 nm (FEMTOLASERS) were used to pre-compensate the dispersion of all following transmitting optics and propagation through air. Optimizing the dispersion with a set of fused silica glass wedges resulted in a pulse duration as short as  $\tau_{pr} = 5.5$  fs with a transform limit of 4.4 fs as measured with a few-cycle SPIDER (APE GmbH), cf. inset in Figure 3.6b. In Figure 3.7, the FCM setup for ultra-fast probing is shown. Because of the very broad spectrum of the probe pulses ( $\Delta\lambda > 300$  nm), the imaging setup required good chromatic compensation. The FCM setup consists of a long distance microscope objective (Mitutoyo infinity corrected, 10x M PLAN NIR,  $NA = 0.26$ ,  $f = 20$  mm,  $1.5 \mu\text{m}$  resolution at  $\lambda = 750$  nm) and an achromatic field lens (Thorlabs,  $f = 250$  mm,  $d = 50$  mm). The microscope objective was shielded from plasma debris with a neutral density filter, which also reduced the intensity on the optics. The distance between objective and lens was set to 270 mm, which resulted in a magnification of 12.8 for the imaging system. After the field lens, a non-polarizing beam splitter was placed in the beam. This allows imaging of the same region with different cameras equipped, e.g., with different spectral or polarization filters. The Basler A102f cameras, which were used in the experiment, have a pixel size of  $6.45 \mu\text{m}$  leading to a resolution of  $0.504 \mu\text{m}/\text{pixel}$ . Hence, the pixel resolution is higher than the spatial resolution, which allows for sub pixel analysis.

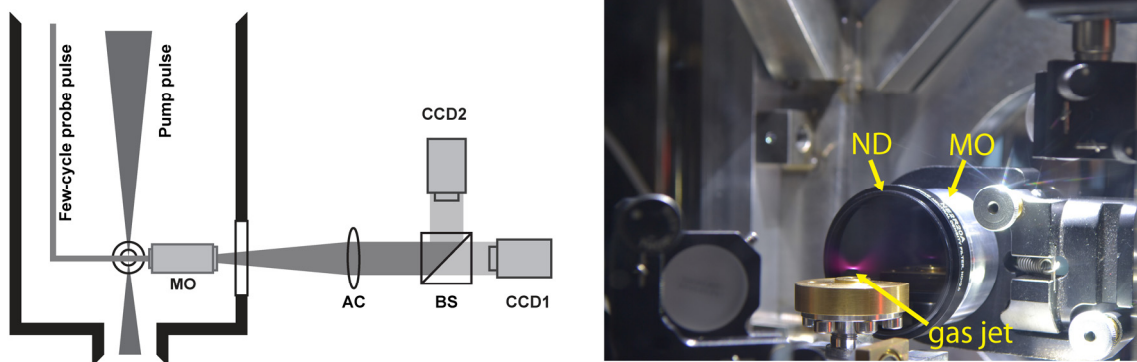


Figure 3.7 | Left: Schematics of the FCM probing setup. MO: microscope objective; AC: achromatic lens; BS: beamsplitter. The second probing channel is optional. Right: Gas jet in the target chamber and imaging optics. The neutral density filter (ND) protects the microscope objective from plasma debris and lowers the intensity of the probe beam to prevent nonlinearities inside the optics.

To overcome the limited field of view, the microscope objective was moved parallel to the propagation of the pump pulse to image the complete interaction on subsequent shots. The absolute position was then determined by the applied delay of the probe pulse and cross checked with the pump pulse's position in the images.

## 4. Laser wakefield acceleration in helium

This chapter is dedicated to showing the immense potential of probing with few-cycle laser pulses and a high-resolution imaging system. This setup and technique will be called few-cycle microscopy (FCM). First, the experimental parameters are discussed and an overview is given over all the laser-plasma features, which can be detected by FCM. Secondly, it is described how this system was used to measure the wavelength of the generated plasma wave at a fixed position in the plasma for various background pressures of the gas jet. Here, a critical density for self-injection was found. Furthermore, the temporal evolution of the plasma at a fixed background density was recorded. For the first time, the evolution of size and shape of the first oscillation period, i.e., the bubble, is shown. Finally, 3-D PIC simulations, which describe the full interaction including the probe beam, are used to support the experimental results. Particular attention is paid to the formation of the images taken by FCM and which important quantities can be derived directly from the shadowgrams.

### 4.1 Experimental setup and probing diagnostics

The experiments described below utilized the few-cycle probe beam for the first time. The experiments were carried out with  $E_L = 750$  mJ of energy and horizontal polarization on target. A conical nozzle with an exit diameter of  $d_{\text{crit}} = 2.7$  mm and helium gas were used. Assuming complete ionization, the resulting electron density distribution 1.25 mm above the nozzle is shown in Figure 4.1a. The focal spot was optimized with an F/12 off-axis-parabolic mirror, but still an elliptical profile remained with a FWHM major axis length of  $a = 12.8$   $\mu\text{m}$  and minor axis length of  $b = 8.8$   $\mu\text{m}$ , see Figure 4.1b. The FWHM area is  $A_{\text{FWHM}} = 91$   $\mu\text{m}^2$  with  $\alpha = 0.23$  of the total energy included within the FWHM focal area. The resulting vacuum FWHM intensity was estimated to  $I_{\text{FWHM}} = 6.3 \cdot 10^{18}$  W/cm<sup>2</sup> corresponding to a normalized vector potential of  $a_0 = 1.7$  in the absence of chromatic and temporal aberrations. The focal spot position was set to the center of the gas jet in transverse direction ( $y$ -axis). In propagation direction ( $x$ -axis) the position was optimized to have high energy ( $> 100$  MeV) electron bunches with a narrow energy spread, see Figure 4.1a. Once optimized, this position remained unchanged during the experiment. The emitted electron bunches were recorded with the setup shown in Section 3.1 using the high-resolution electron spectrometer. The pulse duration of the probe beam was measured prior to the experimental campaign. It was found that once the dispersion was compensated it is sufficient to check the broadening of the spectrum in the hollow core fiber and to adapt the argon pressure to the input energy on a day-to-day basis to ensure a short

pulse duration. As the overall dispersion from the fiber exit to the target chamber remains fixed, the pulse duration of the probe does not change. Because of limited bandwidth (300 nm) of the dispersion compensating mirrors, part of the probe pulse's broadened spectrum emitted from the fiber are leaks through the mirrors and was used to align the fiber

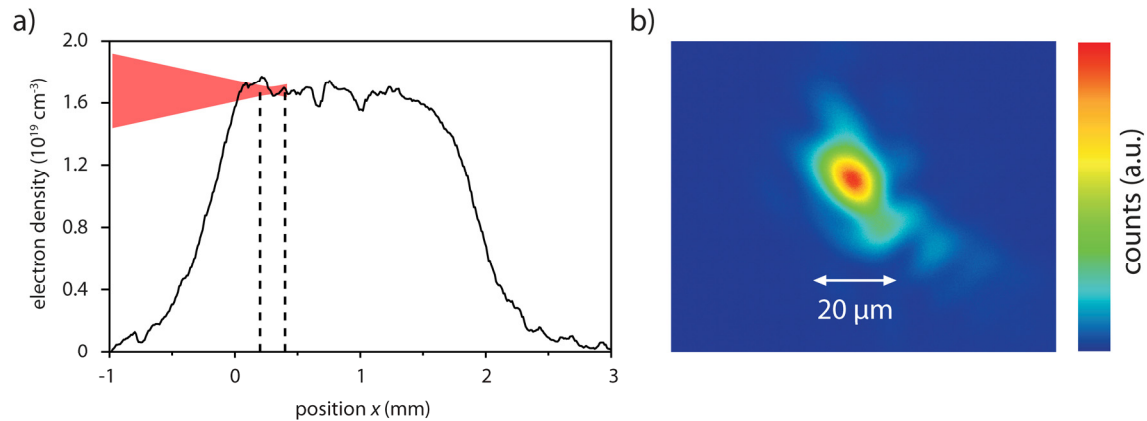


Figure 4.1 | Experimental target conditions and focal spot properties. a) Longitudinal electron density profile derived from the measurement in Section 3.2 with 25 bar helium back pressure. The focal spot position is also indicated. The point of origin of the  $x$ -axis shown here is used as a reference throughout the whole chapter. b) Focal spot in vacuum at lower peak power.

and achieve a Gaussian TEM 00 mode, see Figure 4.2. The very good beam quality exiting the fiber resulted in a uniform brightness distribution at the interaction zone. For the experiments described here, it was essential that the probe pulse had a flat spectral phase before its spectrum was broadened by SPM. Since the probe pulse was split off the pump pulse after the compressor, the dispersion compensation with the DAZZLER could only be done either for the pump pulse or for the probe pulse. Hence, it was not possible to ensure the shortest pulse duration for both pulses, resulting in the pump pulse duration being slightly longer ( $\tau_L = 35$  fs) than its optimum.

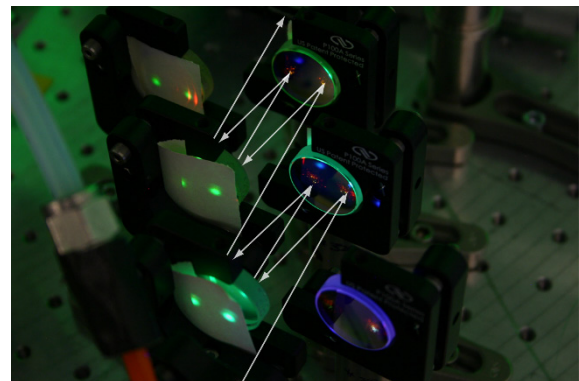


Figure 4.2 | Beam path through the dispersion compensating mirrors and leaking light for spatial mode optimization.

## 4.2 Shadowgraphy with few-cycle probe pulses

The temporal resolution of a shadowgram is determined by the pulse duration of the probe beam, which backlights the interaction. The probe pulses had a duration of  $\tau_{pr} \approx 6$  fs while the camera itself has a shutter time of several milliseconds. This means that the

image, which was recorded by the CCD, contains information on different time scales. On the one hand, information with a resolution of the probe pulse's duration can be acquired, which reveals transient structures like plasma waves and is only visible when the probe is turned on. On the other hand, there is a second timescale that is set by the shutter time of the camera during which the camera integrates over all the collected light. This includes all sources of scattering, e.g. Thomson scattering either linear or nonlinear [106], Raman side scattered laser light [107] or broad band emission from wave breaking [108], thermal plasma emission, or just stray light from the laboratory. In Figure 4.3, an exemplary image is shown including all of the above mentioned effects. The high temporal and spatial resolution reveals the features associated with the plasma wave (a), the position of the main pulse's peak intensity and, hence, information about the temporal intensity contrast, which is characterized by the distance from the pulse's peak to the ionization front (b), cf. Section 5.2.3. Plasma filamentary structures are visualized in the image formed by Fresnel diffraction of the probe rays in the plasma due to a limited depth of field and are visible as dark and bright horizontal lines (c). A similar structure (d) but appearing at an angle to the optical axis is attributed to stimulated Raman side scattering (SRS-S), which also contains information about the local plasma frequency [107]. There are various sources of scattered light, which can also be seen without the probe beam. First, there is Thomson scattered light on the laser axis (e). Its intensity will increase at higher plasma densities

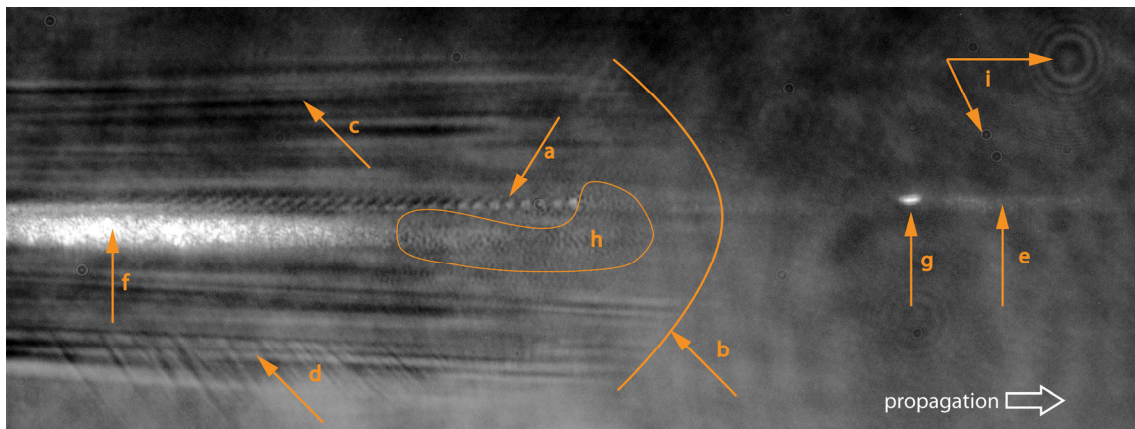


Figure 4.3| Laser wake field acceleration under the microscope, raw data from the CCD. a) Plasma wave driven by the pump, b) ionization front, c) filamentary structure in background plasma, d) channels generated by Raman side scattering, e) Thomson scattered pump light, f) Raman side scatter in observation direction, g) wave-breaking radiation, h) high spatial noise, i) Dust on CCD chip, ND filter or imaging lenses.

and for circular or vertically polarized pump pulses it eventually outshines the probe light, thus obscuring the central part of the image. The saturation of Thomson scattered light in the image can partially be compensated by increasing the intensity of the probe light but it is limited to the damage threshold of the delicate probe beam optics. It becomes an

even greater challenge when laser plasma interactions with solid targets are investigated.<sup>1</sup> In Figure 4.3, a second source of bright radiation is visible (f). It is also attributed to SRS-S, but here the light is scattered into the direction of the camera. The origin for this kind of radiation is likely the spatial and temporal asymmetries of the laser focal spot that can trigger this instability. Bright spots of radiation on the optical axis were identified as wave breaking radiation (g) and mark the injection point of electrons into the plasma wave by transverse wave breaking, as is will be discussed in Section 4.4. In the rare case of multiple injection, the distance between the injection points and the energy difference after the acceleration give quantitative information about the acceleration field in the plasma. The last feature (h), whose origin is still not fully understood, is the appearance of speckles or high-frequency noise around the main pulse. It can be detected in regions with near relativistic laser intensities, as derived from the focal spot profile. Finally, dust particles on the CCD chip itself or on optics in the probe beam path diffract the probe light (i) and form distinct diffraction rings. From the variety of features, which can be seen in the shadowgraph above, this chapter focuses primarily on the measurement of the plasma wavelength of the first and second plasma wave periods in relation to the position of wave breaking and, hence, electron injection.

A high-resolution snap shot of a laser wake field accelerator is shown in Figure 4.4. For better visibility, this image and all following (if not mentioned otherwise) images were post processed and the relative intensity modulation calculated as described in Appendix B. This snap shot was taken after  $x = 1.1$  mm of pump pulse propagation into the gas jet

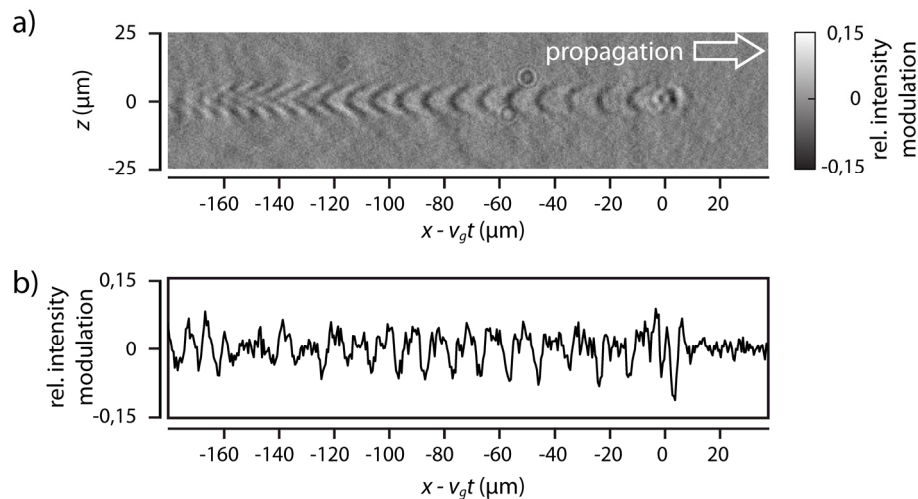


Figure 4.4 | High-resolution probing of the plasma wave. a) Shadowgraphy image after  $x = 1.1$  mm of propagation into the plasma at a density  $n_e = 1.6 \cdot 10^{19} \text{ cm}^{-3}$  and b) profile of a) along  $z = 0$ .

<sup>1</sup> Even when a ND filter is used in front of the objective to reduce the overall brightness, one has to consider that the intensity of the probe pulse is sufficient for nonlinear effects, e.g. bleaching. The filter would now act as a saturable absorber with a higher overall transmission.

at an electron density of  $n_e = 1.65 \cdot 10^{19} \text{ cm}^{-3}$ . The plasma wave has developed a structure with clearly curved wave fronts, which is a result of its nonlinear evolution. The relativistic oscillating electrons constituting the plasma wave cause  $\omega_p$  on axis to decrease by  $\sqrt{\gamma}$  relative to its off-axis value [71], thus curving the wavefront which is analyzed in more detail in Section 4.7. At the same time, the brightness modulation is far from a sinusoidal form, which would be characteristic for a linear plasma wave excitation, and instead exhibits a more saw tooth like shape. This is characteristic for the blowout regime, see Figure 4.4b. In this regime, the plasma electrons are fully expelled from the first oscillation period, i.e., the bubble, and subsequent periods. The wave front curvature is nearly constant for more than 10 oscillation periods and between the 11<sup>th</sup> and 14<sup>th</sup> period the shape changes. An apex is formed on axis and the phase fronts start to overlap. The front section of the bubble reveals some more detailed structure, which is unintuitive and will be explained later with the help of simulations in Section 4.8.1. As the image seems to resemble the electron density distribution from the simulation, it is important to discuss how these shadowgrams are formed and how to derive important quantities such as the plasma period. In Section 4.8.1, it will be shown that the plasma wavelength is equivalent to the distance between two intensity minima along the wave's propagation direction. These intensity minima could be identified as density peaks in the plasma .

#### 4.2.1 Influence of the pump pulse on the plasma wavelength

The plasma wave, which is excited by the driving laser pulse, is a periodic electron density modulation. Its characteristic wavelength depends on the electron density and is given by

$$\lambda_p^* = 2\pi \frac{c}{\omega_p} \sqrt{\gamma} = 2\pi c \sqrt{\frac{\epsilon_0 \gamma m_e}{e^2 n_e}}. \quad (4.1)$$

The vacuum intensity of the laser used in the experiments has a normalized vector potential in vacuum of  $a_0 < 2$ , which is quite moderate. One would not expect that the plasma wavelength be altered significantly by the intensity related mass increase of the plasma electrons. However, in the following chapters it becomes apparent that a manifold of effects like relativistic self-focusing and longitudinal compression of the driving laser pulse can alter the wavelength of the first and subsequent plasma periods. The wavelength increase due to intensity amplification of the pump pulse can be estimated by [107]:

$$\lambda_p^* \approx \lambda_p \left( 1 + \frac{a_0^2}{2} \right)^{1/4} \quad (4.2)$$

Applying this formula for the here discussed experiments (estimated  $a_0 = 1.7$  for an aberration free beam) would result in a slight increase of the plasma wave length to  $1.25 \lambda_p$ .



### 4.2.2 Comments on beamloading

In addition to the pump's intensity amplification, which can change the plasma wavelength, beamloading can also lead to a lengthening of the individual periods of the plasma wave. Beamloading occurs when electrons are injected into the wakefield and the electric field generated by their charge overlaps with the wakefield associated with the laser generated plasma wave. Beamloading is reached when the resulting electric field is constant across the whole electron bunch. Compared to linear wakefields where transverse beamloading poses a problem [109], in the nonlinear blowout regime it can be neglected as the amplitude of the longitudinal electric field does not vary in the transverse direction. Tzoufras *et al.* [110] analyzed the nonlinear regime theoretically and Rechatin *et al.* [111] investigated it experimentally. They found that beamloading acts in different ways depending on its strength. First, if the electron charge injected into the bubble is high enough, the electrons at the front of the bunch shield the wakefield from the electrons at the bubble's rear. Hence, depending on the position in the bunch, the electrons experience different acceleration field strengths. As a result, the energy spectrum broadens and the bunch length increases, causing the length of the bubble to grow. Consequently, electrons can be trapped more easily and the effect amplifies itself. At one point, the wakefield cavity is completely loaded and electron injection is stopped. Following Eq. (2.44), beamloading in the here presented experiments has to be considered if the injected charge  $Q_{\text{tr}} > 200$  pC.

## 4.3 Measurement of the plasma wavelength and the self-injection threshold

In Sections 4.4 and 4.5 it will be shown that for a fixed background electron density the plasma wavelength changes during the interaction. It does not solely depend on the background plasma density but depends also on the pump's momentary intensity, which changes too. To be able to study both effects, a position sufficiently far into the gas jet was chosen and kept fixed during this investigation. In its central region, the supersonic gas jet produces a plateau in the background density, see the experimental setup in Figure 4.1. At this position, the emission of wave breaking radiation was detected frequently. Its appearance is an indication of the position for transverse wave breaking and thereby the beginning of electron injection. As it is still early in the acceleration phase and injection just happened, beamloading effects are still negligible. At this probing position, the backing pressure of helium gas was scanned from 5 bar to 35 bar. In this range, shadowgrams of the plasma wave were obtained with a contrast sufficient for a quantitative evaluation. Above 35 bar, the plasma wave had sometimes already started to disintegrate or intense



scattered pump light made an exact evaluation impossible. Below 9 bar, the visibility of the plasma wave was quite poor.

In the experiment, 1800 shots covering the above mentioned density range were taken and in 900 shots, a single plasma wave was present. In 600 shots, no plasma wave was visible. The reason for this may be either an electron density, which was too low, or a malfunction of the valve. The remaining 300 shadowgrams, mostly taken at high background densities, show a strongly distorted plasma wave with no clear periodicity. This particularly includes images showing a plasma wave, which was broken after the first wave period. Unfortunately, these shapes of the plasma wave are observed most frequently when mono-energetic electron bunches were simultaneously detected. A number of shadowgrams show a remarkable sharpness and richness in detail, like in Figure 4.4, and can therefore be used to determine the plasma wavelength directly from a profile along the propagation axis. However, to reduce the influence of brightness modulations in the image, the shadowgrams are post processed and the relative intensity modulation is calculated as explained in Appendix B. After that, a profile along the laser axis was taken from the normalized images and then a continuous wavelet analysis (CWT) performed. The analysis of a 1-D lineout yields a 2-D spectrogram with the spatial wavelengths plotted for each position along the propagation axis. This is different to a 1-D Fourier transformation yielding the complete frequency spectrum. Using CWT the local plasma wavelength as a function of its position in the plasma wave train can be obtained. Two exemplary CWT maps are shown in Figure 4.5.

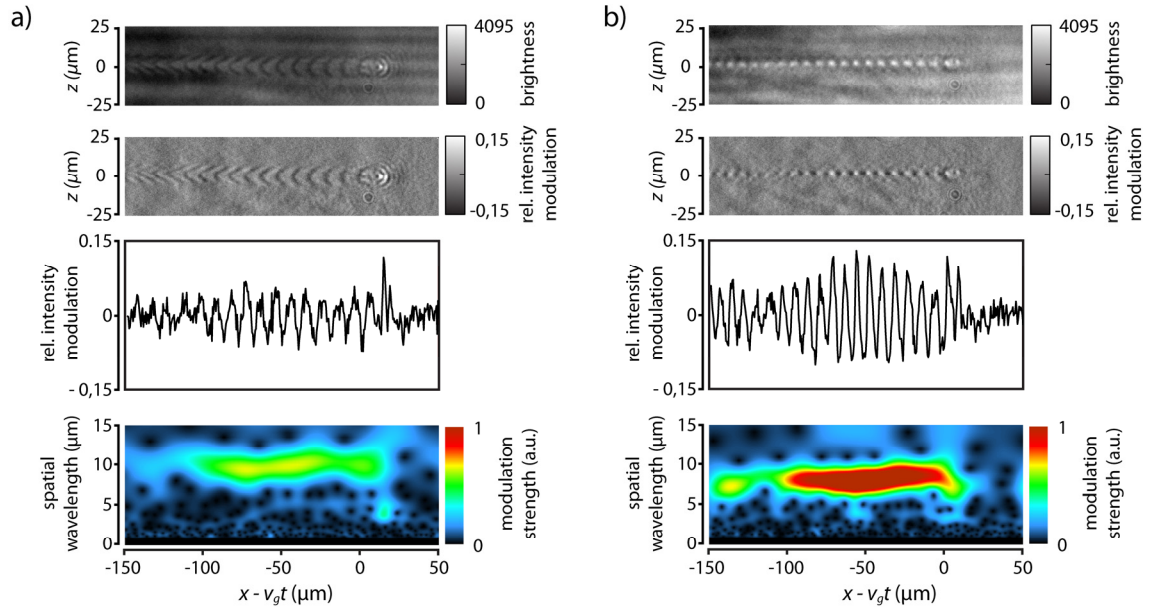


Figure 4.5 | Evaluation of the shadowgrams. From top to bottom: Raw data, postprocessed shadowgram, profile along  $z = 0$  from the postprocessed shadowgram, CWT maps of the profile a)  $n_e = 2.1 \cdot 10^{19} \text{ cm}^{-3}$ ,  $\lambda_p = 10.5 \text{ } \mu\text{m}$  b)  $n_e = 2.1 \cdot 10^{19} \text{ cm}^{-3}$ ,  $\lambda_p = 8.5 \text{ } \mu\text{m}$ .

Using this approach, small structures with a shorter modulation period than the plasma wavelength are detectable at the front of the bubble (Figure 4.5a). Additionally, the amplitude in the CWT map gives information about the modulation depth of the shadowgram. This in turn gives qualitative information about the plasma wave amplitude. The higher the plasma wave amplitude the stronger its influence on the probe beam as it gets refracted into regions of low electron densities. This leads to bright spots on the laser axis as evident in Figure 4.5b. While the profile and the calculated CWT map show a strong modulation in amplitude, the shadowgram shows less detail. The transverse extent of the plasma wave is reduced and looks similar to a pearl necklace. However, the plasma wavelength can still be retrieved but information of its distinct shape, like in Figure 4.5a, is lost. At the same time, the modulation strength is not constant but seems to be at a minimum around  $x - v_g t = -130 \mu\text{m}$ , i.e., around the 12<sup>th</sup> oscillation period of the wave. This is probably an effect of phase mixing induced by position dependent plasma frequency shifts [8].

A complete plot of the wavelength of the second plasma period versus the backing pressure of the valve and therefore versus the background electron density is shown in Figure 4.6. The second period was chosen because it enabled an automatic analysis of the full data set using the CWT method described above. The first period shows a more distinct substructure, which makes an automated measurement more challenging. At a fixed pressure, the plasma wavelength seems to fluctuate by up to 20 %, which is more than the expected fluctuation in the gas density profile of the supersonic jet. Nevertheless, two regions can be distinguished. For pressures between 5 bar and 25 bar, the plasma wavelength steadily decreases with increasing backing pressure. For pressures beyond 25 bar, the fluctuations are much higher but within this variation, the average wavelength appears nearly constant. This behavior has not been observed before.

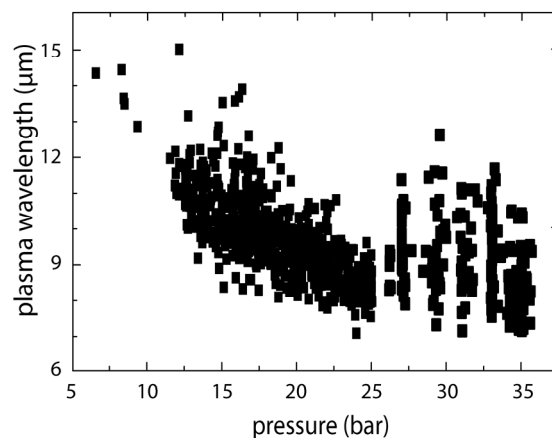


Figure 4.6 | Wavelength of the second plasma period versus backing pressure for helium gas. Data from 900 shots for the second plasma period after 1.1 mm propagation into the gas jet.

To initially analyze this phenomenon, data points up to a pressure of 25 bar were evaluated. Eq. (4.2) was used as a fit function but any influence of the  $\gamma$ -factor of the electrons was neglected ( $\gamma = 1$ ). Rewriting in practical units, cf. Eq. (4.2), allows correlation of the backing pressure  $p$  with the plasma wavelength.

$$\lambda_p = \frac{10.56 \mu m}{\sqrt{C_{\text{He}} \times [\text{bar}]}} \quad (4.3)$$

For  $C_{\text{He}} = 0.065 \pm 0.001$  the deviation is minimized. For  $p = 25$  bar, the extrapolated plasma wavelength agrees quite well with the one calculated using the density profile from neutral helium in Figure 3.3 and assuming double ionization. Hence, for  $p < 25$  bar,  $\gamma \approx 1$  in Eq. (4.1) seems reasonable. Consequently, the  $\gamma$ -factor and accordingly the intensity of the pump pulse at this position is smaller than expected (for  $a_0 = 1.7 \rightarrow \gamma = 1.56$ ). A possible source for this intensity reduction can be spatio-temporal aberrations such as a pulse front tilt [112] as will be described in later sections. Following the justification from above, the applied backing pressures can be directly associated with the background electron density. To get a better understanding of the underlying mechanics in Figure 4.6 it makes sense to include the results from the electron beam profile diagnostics. Electron densities and corresponding electron beam profiles within a range of  $\Delta n_e = 2 \cdot 10^{18} \text{ cm}^{-3}$  were averaged and binned. The error bars were calculated from the standard deviation of the averaging divided by the square root of the number of samples taken. The results are shown in Figure 4.7. Below an electron density of  $n_e \approx 1.5 \cdot 10^{19} \text{ cm}^{-3}$ , which seems to be a threshold value, the binned values follow the relation of Eq. (4.1) with  $\gamma = 1$ , shown as a red line in Figure 4.7a. Above this threshold density the plasma wavelength actually *increases* and remains almost constant, despite increasing background density. At this point, it makes sense to correlate these findings with results of the first scintillation screen, which records the electron beam profile and the overall accelerated charge, cf. Figure 4.7b. The screen was positioned 53.5 cm behind the gas jet and detects all electrons with an energy above 100 keV and within a full opening angle of 100 mrad. The intensity of the emitted light by the screen is proportional to the electron charge passing through the screen. For the Kodak Biomax screen, which was used in these experiments, its response was only weakly dependent to the electron's energy in the range between 1 MeV and 200 MeV. Furthermore, the electron charge was sufficiently low to avoid saturation [93]. For electron densities,  $n_e < 1 \cdot 10^{19} \text{ cm}^{-3}$ , hardly any charge is injected and subsequently accelerated, even though a plasma wave could be observed in the shadowgrams. However, increasing the electron density above  $n_e = (1.5 - 1.6) \cdot 10^{19} \text{ cm}^{-3}$  leads to the formation of a collimated electron bunch. Obviously, this density is a threshold for self-injection. As described in Section 2.14.1, this threshold depends solely on the parameters of the driving laser pulse and the background electron density.

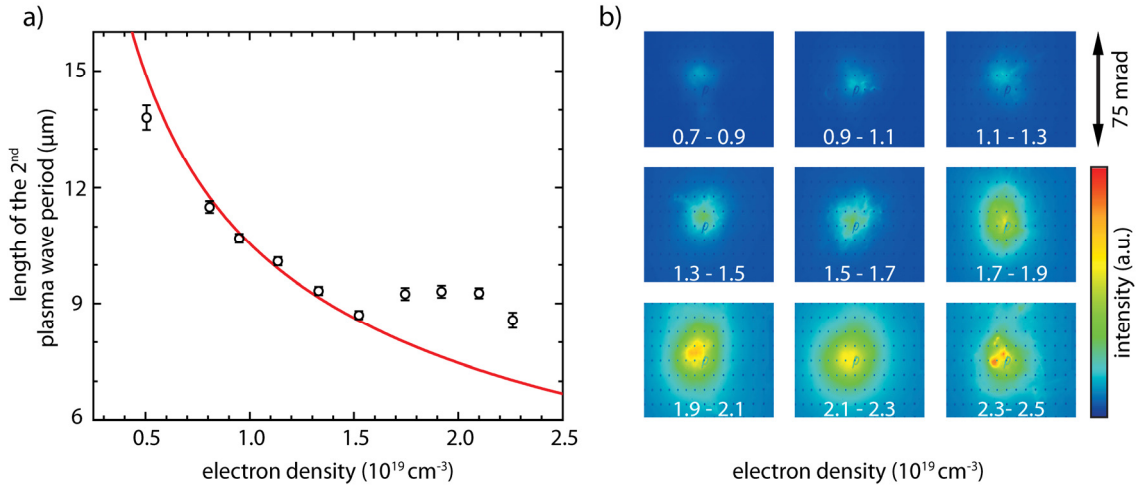


Figure 4.7 | Plasma wavelength of the 2<sup>nd</sup> period for different electron densities and injection threshold. a) Data from Figure 4.6 binned and Eq. (4.3) used as a fit function (red curve). The fit only included data points up to  $n_e = 1.5 \cdot 10^{19} \text{ cm}^{-3}$ . b) Electron beam profiles from the first scintillator screen for different plasma densities averaged over 40-180 shots, corresponding to the data points in a).

For fixed laser conditions, as in the experiments described here, the electron density is the only free parameter to control the injection by transverse wave breaking. The laser power in units of the critical power for relativistic self-focusing multiplied by a parameter  $\alpha$ , which determines the fraction of laser energy within the FWHM of the focal spot, should fulfill [86]

$$\frac{\alpha P}{P_c} > \frac{1}{16} \left[ \ln \left( \frac{2n_c}{3n_e} \right) - 1 \right]^3. \quad (4.4)$$

For the laser parameters specified in the beginning of this chapter this relation is fulfilled for  $n_e > 1.5 \cdot 10^{19} \text{ cm}^{-3}$ . At the threshold for self-injection, the electron beam has a small divergence on the order of 1-2 mrad and its energy spectrum has a very narrow energy spread. Both features are related to the pump pulse just being intense enough to trigger injection at a very small point in space. This limits the amount of injected charge and is not expected at higher electron densities. As the pump pulse depletes quickly after wave breaking, subsequent injection, which would generate a dark current, is suppressed. In Figure 4.8, shadowgrams from different shots are shown together with the beam profile of the corresponding electron pulse. All three shots have produced electron beams with similar beam profiles having a full divergence of 2 mrad (FWHM) and showing a low background only. These beams exhibit a narrow energy spread with central energies from 90 MeV (Figure 4.8a) to 140 MeV (Figure 4.8b). The electron densities are close to (Figure 4.8b) or above the threshold for self-injection. However, the similarity in the electron beam profiles cannot be found in the shadowgrams. In each shot the plasma wave exhibits

distinctly different shapes after a propagation length of  $x = 1.1$  mm. In particular instabilities like filamentation are prominent as indicated by the white arrows in Figure 4.8a and c. The splitting of the pump pulse leads to a reduction of energy of the pump pulse in each of the pulse fragments.

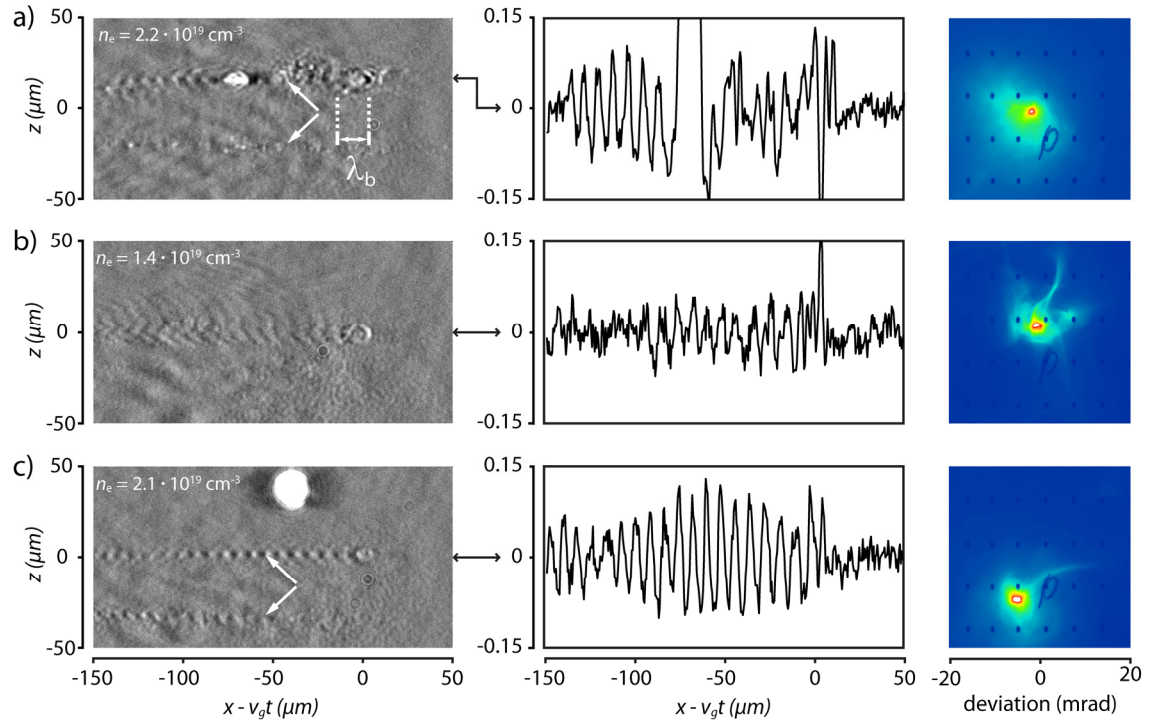


Figure 4.8 | Shadowgrams, longitudinal profiles and electron bunch profiles with a typical divergence of 2 mrad at different electron densities. The images are cropped and shifted to match the position of the pump pulse's peak to  $x = 0 \mu\text{m}$  at the absolute position  $x = 1.1$  mm. a)  $n_e = 2.2 \cdot 10^{19} \text{ cm}^{-3}$ , b)  $n_e = 1.4 \cdot 10^{19} \text{ cm}^{-3}$ , c)  $n_e = 2.1 \cdot 10^{19} \text{ cm}^{-3}$ .

This can explain the good collimation of the electron bunches at rather high background densities. Following Eq. (4.4) the reduced energy in the main pump pulse now requires a higher electron density for self-injection. The plasma wave itself is typically more than 150  $\mu\text{m}$  long but sometimes deformed. In Figure 4.8a, a very long bubble with nearly double the length expected at this electron density is seen. This is characteristic for a long propagation at this high electron density where the first and second period can merge and the trailing wave is completely broken. However, it seems to recover 70  $\mu\text{m}$  behind the peak of the pump pulse. This strong modulation in the envelope of the amplitude of the plasma wave is present in a number of shots. In Figure 4.8b, the modulation strength of the plasma wave is reduced compared to Figure 4.8c, which can be an indicator for wave breaking although no radiation was detected here. The phase fronts of the plasma wave in Figure 4.8b show a strong tilt above the relativistic channel and are visible up to 40  $\mu\text{m}$  above the laser's propagation axis. These *leaking* plasma oscillations were detected very

rarely and can be explained by the hosing instability [113]. Here, a spatio-temporal asymmetric pump pulse propagates through the plasma while the back of the pulse experiences the space and time dependent plasma frequency profile generated by the front of the pulse and starts to oscillate transversely along the propagation. At the turning points, parts of the back of the pulse *leak* outside the relativistic channel and can excite plasma waves propagating under an angle away from the optical axis.

However, even at a background density slightly above the threshold for self-injection the pump pulse has to undergo several stages of self-focusing and pulse compression as the vacuum intensity seems to be too low. Otherwise, wave breaking and injection would occur at the very beginning of the interaction already. Therefore, the evolution of the pump pulse, which can be deduced indirectly from the evolution of the plasma wave is of central importance and will be analyzed in detail in the following sections.

To summarize, the strong deviation from the simple square root dependency of the plasma wavelength at a fixed position on the electron density is caused by the nonlinear intensity amplification of the pump pulse. The plateau at  $n_e = (1.6 - 2.2) \cdot 10^{19} \text{ cm}^{-3}$ , where the plasma wavelength remains constant while the background density increases, is formed by two counteracting mechanisms. The plasma wavelength is increased due to intensity amplification of the driving laser pulse and eventually by beamloading as the pump pulse is further in its relative evolution; and the plasma wavelength is simultaneously decreased due to a higher electron density. However, at the same time, the depletion length decreases with increasing electron density and so the laser intensity will decrease causing the plasma wavelength to shorten. The threshold densities at which the deviation from the square root law sets in relates to the self-injection of electrons into the plasma wave. This is in very good agreement with the self-injection model by Mangles *et al.*, which accurately predicts this threshold, even though the relativistic wavelength increase due to  $a_0 \approx 1.7$  was not taken explicitly into account. It seems that the relativistically corrected plasma frequency  $\omega_{\text{rel}} = \omega_p \cdot \gamma^{-1/2}$ , which is measured by FCM via the plasma wavelength, is the key parameter.

#### **4.4 Temporal evolution of the plasma wave in the self-injection regime**

In the previous section, the plasma wave was analyzed at a fixed position for a broad range of electron densities. A threshold density,  $n_e = 1.5 \cdot 10^{19} \text{ cm}^{-3}$ , above which electrons emitted in laser-forward direction could be detected, was discovered and identified with the threshold for self-injection of electrons into the plasma wakefield. As the next step, the evolution of the plasma wave was studied at this particular electron density. Operating close to a threshold usually results in a high fluctuation and a broad range of results, so a slightly higher electron density of  $n_e = 1.65 \cdot 10^{19} \text{ cm}^{-3}$  was chosen while the delay

between pump and probe was varied. To improve statistics, 100 shots were taken at each of the 30 different delay steps. Hence, the 2.7 mm long interaction length of the gas jet was divided into steps, which were each 100  $\mu\text{m}$  apart. This corresponds to an evolution time of 330 fs of the plasma wave between two adjacent steps. Due to the limited field of view of 650  $\mu\text{m}$  of the imaging system, the microscope objective was moved parallel to the pump pulse direction while the delay between the pump and the probe was scanned. Afterwards, the absolute position of the shadowgrams was calculated from the displacement and referenced to the position in Figure 4.1a. Cross-calibration was done by just moving the objective without changing the temporal delay and measuring the shift in the shadowgram. Between two successive shots, the plasma wave jitter in position in the propagation direction was up to 10  $\mu\text{m}$ . At this point, it could not be distinguished whether the fluctuations in the arrival time are due to nonlinear effects in the plasma, which can affect the group velocity of the pump pulse, or due to a variation in the different beam path length of pump and probe. The two pulses were separated 10 m before the interaction point. The pump pulse propagates in vacuum while the probe pulse mainly propagates in air. A relative error of  $10 \mu\text{m}/10 \text{ m} = 10^{-6}$  of the arrival time seems reasonable in such an environment.

The energy spectra of the electrons were recorded simultaneously with the shadowgrams. The snapshots shown in Figure 4.9 (left column) are representative for each time step during the evolution of the plasma wave during the acceleration process. Those images were selected, which corresponded to shots producing similar electron spectra with a narrow energy spread between 100 MeV and 150 MeV as shown in Figure 4.9a-l and having a good image quality, i.e., a high contrast. The recorded charge was typically between 10 pC and 40 pC. At the very edge of the gas jet, i.e., before the pump pulse goes through the (vacuum) focal plane, only a bright modulation originating from the momentary position of the highest intensities of the pump pulse is visible, which is surrounded by granular noise. As the pump pulse propagates up the initial density ramp, the regions of high and low electron density gradient (dark and light regions in the image) are approximately equal in length, indicating a linear excitation of the plasma wave, Figure 4.9a. The plasma wave itself is asymmetric and the phase fronts are tilted. This can be caused by a spatio-temporal asymmetry in the pump pulse's intensity profile [33, 114]. A misalignment of the laser pulse's compressor or stretcher grating can result in a pulse front tilt [112]. It is important to note that the design of the JETi40 pulse compressor does not allow compensation of the angular chirp in the vertical direction, which is the same direction as the asymmetry shown here, but only in the dispersion plane of the gratings and so the polarization direction of the laser. During propagation of the pulse through the focal plane, the asymmetry in the plasma wave is reduced and a relativistic curvature of the phase fronts dominates (Figure 4.9b-d). This means that the oscillation normal to the phase fronts in Figure



4.9b,c is now dominated by a transverse oscillation. In this region, some scattered radiation below the plasma wave is visible emanating from the pump pulse. This is attributed to Raman side scattering due to the above mentioned asymmetries in the initial pump pulse. The transverse extent of the plasma wave reduces and the amplitude of the wave increases, cf. Figure 4.9e, due to pulse shortening and self-focusing of the laser pulse.

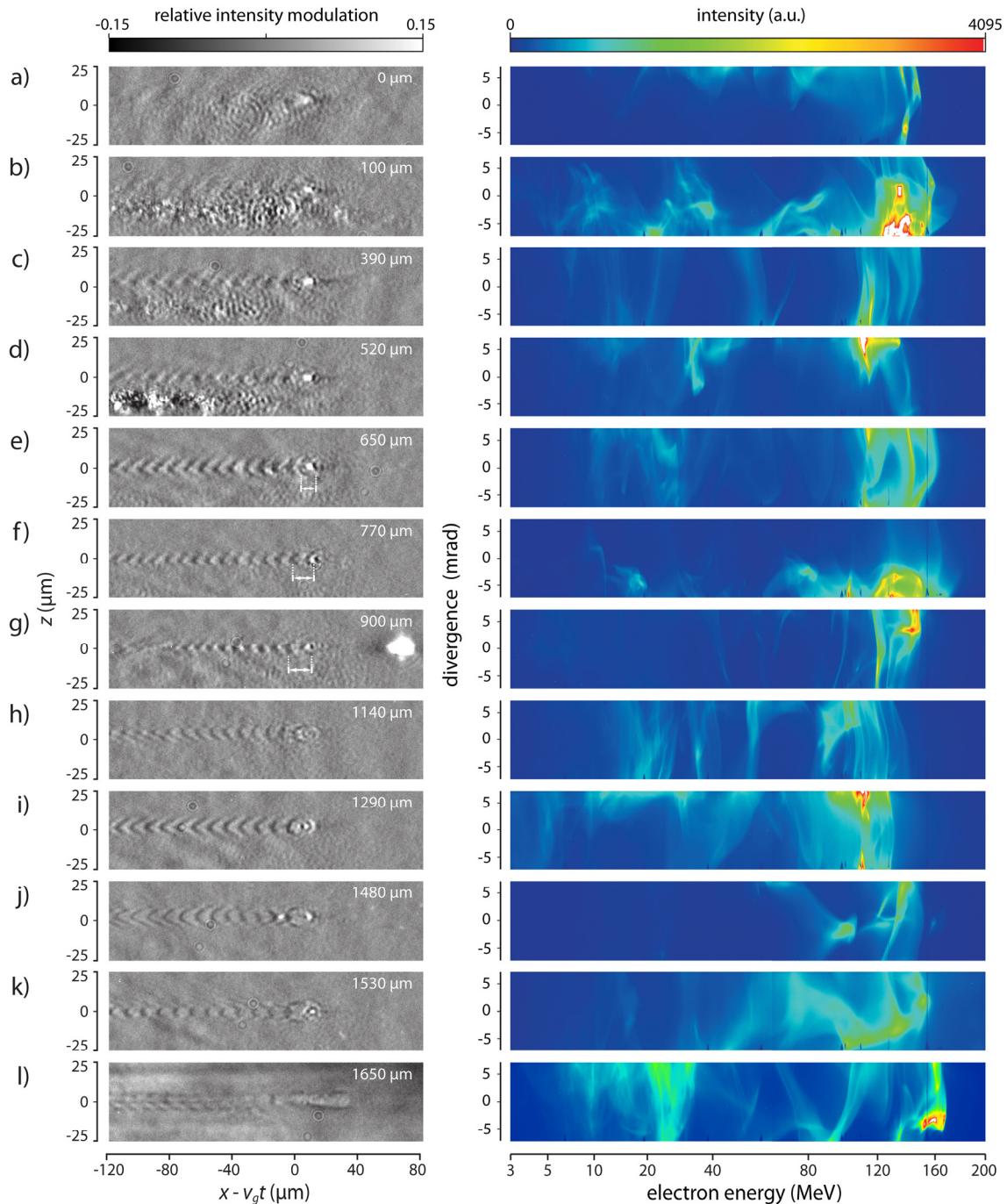


Figure 4.9 | Evolution of the laser driven plasma wave. Postprocessed shadowgrams (left) at different propagation distances (white inset) and corresponding electron energy spectra spatially resolved in the vertical direction (right).



A significant increase of curvature of the plasma wave train and, in particular, in the lengthening of the first plasma period in Figure 4.9e-g is visible. Just ahead of the region where this lengthening starts, bright emission from the plasma was observed, cf. Figure 4.9g. Spectrally resolved measurements, see appendix C, reveal its broad spectrum, which is consistent with wave breaking radiation [108]. This emission is a direct signature of the point of self-injection in the experiment. Further propagation enhances the density gradient at the front of the bubble, which now appears in the shadowgrams at the beginning of the wave train with a curvature in the opposite direction. The length covered by the laser pulse up to this position matches quite closely the depletion length, cf. Eq. (2.39). After this length, approximately the front half of the pulse is etched away and a density spike is formed at the front of the bubble. From this observation, we can conclude that the main part of the acceleration process takes place *after* the depletion of the pump pulse. After wave breaking, the plasma wave reveals more details; in particular, the reversal in the direction of curvature of the trailing wave periods in the shadowgrams, Figure 4.9h-k. This is closely linked to the process of transverse wave breaking [71]. It is important to note, although wave breaking has occurred already, there are still several wake periods following the main pulse albeit at reduced modulation strength. Only in a very small number of shots was the plasma wave completely broken after the first oscillation period. This is equivalent to the evolution of the plasma wave into a single bubble. In these cases, the energy spread of the accelerated electron bunch was very narrow and no dark currents were present. In the last image of Figure 4.9, the first two plasma periods have merged and formed a very large bubble, which is another possible outcome of the plasma wave evolution and was observed in the simulation presented in Section 4.8.2.

#### 4.4.1 Wave breaking radiation

In the following section, a particular point during the plasma wave's evolution signified by the appearance of wave breaking radiation is characterized in more detail. At this point, injection of electrons into the wakefield sets in. The violent acceleration of the electrons during self-injection leads to emission of radiation with a broad spectrum. Its intensity correlates with the injected charge. The point of emission is highly localized and its longitudinal extent in a single shot is in the range of  $\Delta x = 5 \dots 15 \mu\text{m}$ , while the transverse extend is smaller, typically  $\Delta z = 5 \mu\text{m}$ . The actual source could be even smaller since the images are saturated at that point. In some cases, there is more than one emission point of bright radiation, which can result in the generation of multiple electron pulses. The position  $x$  of each point where wave breaking radiation was emitted was taken and statistically evaluated. The result is shown in Figure 4.10a. The mean position is located at  $x = 930 \mu\text{m}$  with a standard deviation of  $\sigma = 67 \mu\text{m}$ . The spread is caused by the pump pulse's evolution and, hence, depends on its initial parameters, which can vary slightly

from shot to shot. In Figure 4.10b a number of shadowgrams are shown in which wave breaking radiation could be detected. As it was already pointed out in the last section, the point of emission of wave breaking radiation separates two regimes characterized by the front of the bubble. In front of this point, the bubble's front is hardly visible, only as a small black dot. Behind the point of emission and thus after injection, the front exhibits a concave curvature.

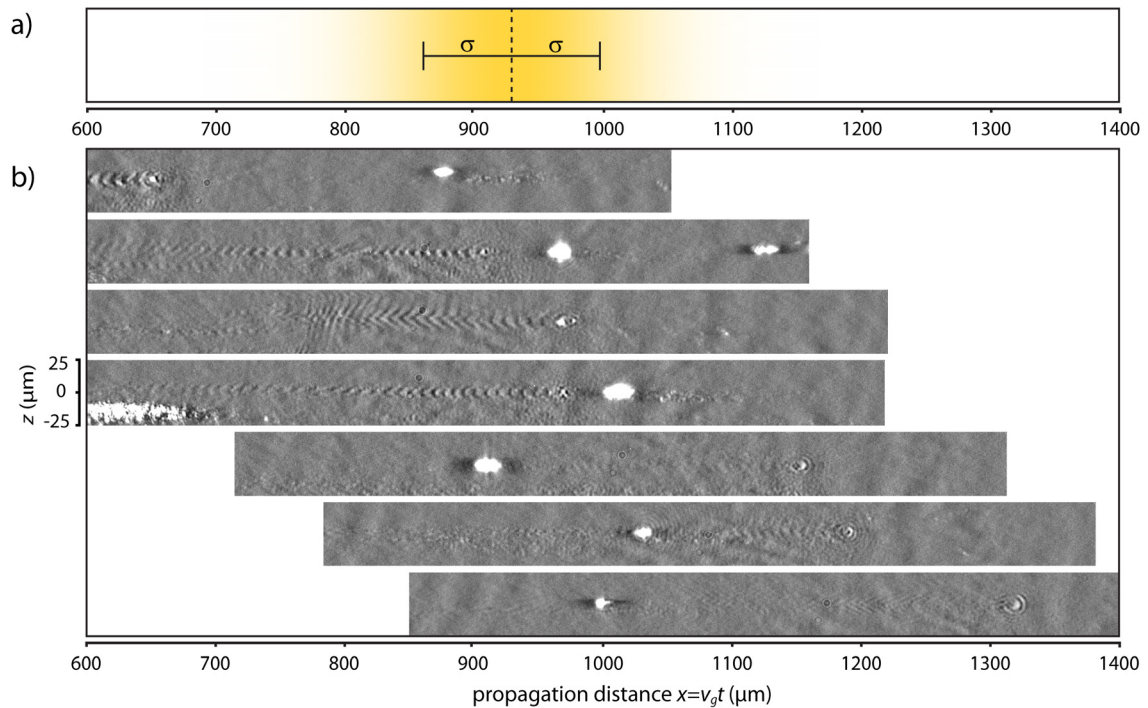


Figure 4.10 | Wave breaking radiation in the self-injection regime. a) Representation of the normal distributed positions of wave breaking emission from all evaluated shots. b) Selected shadowgrams with wave breaking emission present.

Injection of electrons is occurring at the back of the bubble, hence, changes at the bubble front are likely to be attributed to changes of the pump pulse. Therefore, it is more likely that the density spike due to the etching of the front of the pump pulse causes the curvature at the bubble front. At this point, it has to be stressed that although depletion length and position of the wave breaking radiation matches quite closely in the experiment described here, they are not directly linked but are rather an attribute of the pump pulse's evolution as shown in the following sections.

## 4.5 Evolution of the first and second oscillation periods

In the previous sections, it was shown that the plasma wave undergoes a dramatic change in shape during its propagation through the plasma. It is of particular interest how the length of the first, i.e., the bubble, and second plasma period change during propagation

and injection of electrons. As shown in Section 4.3, the length of the second period can be extracted directly from the shadowgram. The position of the back of the bubble is usually easy to determine due to the characteristic shape of the plasma wave and its good visibility in the shadowgrams. The front, however, shows more details and exhibits a high brightness modulation within this period. This kind of modulation is not expected here since the electron density gradient should be sufficiently smooth. However, the simulated shadowgrams, which will be discussed in more detail in Section 4.8, show the same feature. The computed shadowgrams in combination with the electron density distribution from the simulation allow determination of the position of the bubble front, see Figure 4.11. At an early stage during the evolution, see Figure 4.11a, the electron density gradient at the front of the bubble is relatively weak. Still, a small white spot can be used that

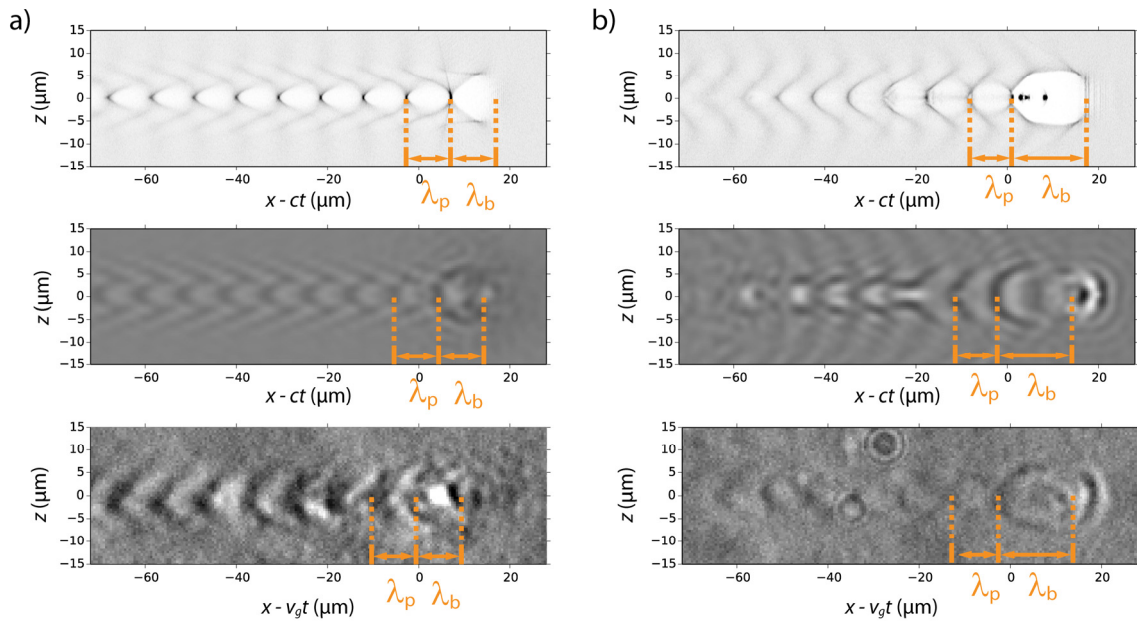


Figure 4.11 | Measurement of the bubble length. Electron density distribution from the simulation (top), artificial shadowgram (center) and experimental data after a)  $x = 455 \mu\text{m}$  and b)  $x = 1214 \mu\text{m}$  propagation. The length of the first, i.e., the bubble, and second plasma periods are drawn in at the appropriate positions.

marks the position of the front of the bubble. Note that there seems to be a *virtual* first period, which should not be considered for the measurement. The probing geometry has a major influence on this and it will be explained later in Section 4.8.1. After further propagation, the front of the bubble has further evolved and the electron density gradient is much stronger. Now a small black dot is the feature, which marks the position of the front of the bubble.

From the 3000 shots taken during the delay scan with helium gas, only shots were selected, which have produced an electron bunch charge of more than 10 pC at energies higher than 60 MeV to ensure an acceleration in the self-injection regime. Operating

slightly above the threshold density for self-injection, this resulted in a total number of 202 shots. The propagation distance  $x$  was sampled in  $100 \mu\text{m}$  steps, and the measured bubble lengths were averaged. For the evolution of the second plasma oscillation period, the CWT method was used which also provided information about the modulation strength. Special care has to be taken for measuring the plasma period length at the leading edge of the gas jet. There, the pulse front tilt of the pump pulse excites an almost linear plasma wave with phase fronts tilted by an angle  $\varphi$  with respect to the pump pulse's propagation direction. Thus, the wave period determined by CWT is stretched by  $1/\cos(\varphi)$  along a true linear oscillation, see Figure 4.12.

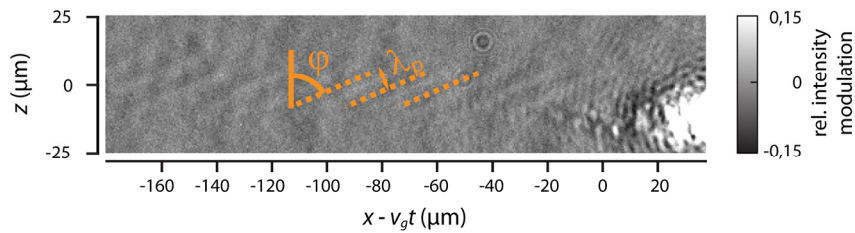


Figure 4.12 | Tilted plasma wave at the edge of the gas jet ( $x = 70 \mu\text{m}$ ) and determination of the plasma period length.

This increases the plasma wavelength along the propagation axis as shown in Figure 4.13a for  $x \leq 0.6 \text{ mm}$ . Afterwards the plasma period follows the density profile of the gas jet. Up to  $x = 1.2 \text{ mm}$  it is only slightly longer than the plasma wavelength calculated from Eq. (4.1). After the propagation distance of two to three Rayleigh lengths the tilt has disappeared and the nominal plasma period can be deduced from the shadowgrams.

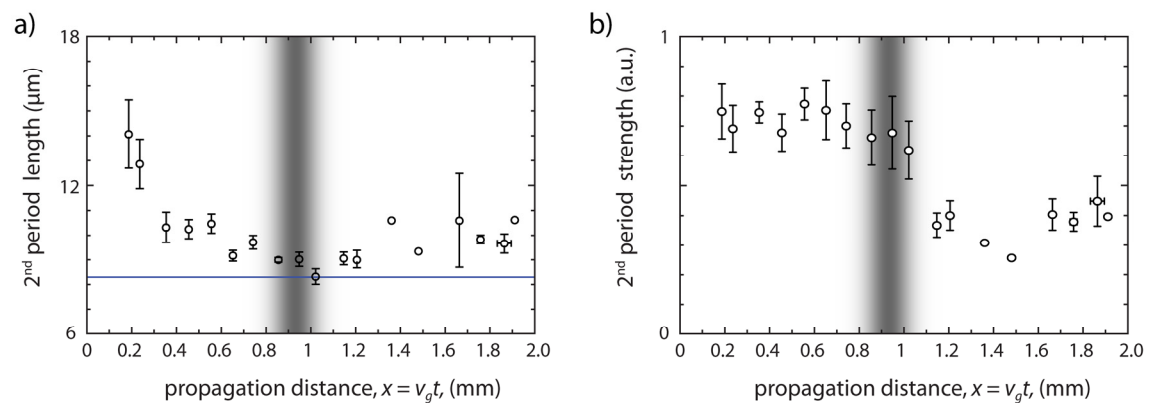


Figure 4.13 | Evolution of the second plasma wave oscillation period. a) Length of the period. The blue horizontal line is the expected plasma period for  $n_e = 1.65 \cdot 10^{19} \text{ cm}^{-3}$  and linear excitation. b) Modulation strength. The grey shaded area marks the region of wave breaking emission.

At  $x = 1.1 \text{ mm}$ , the plasma wavelength matches the value expected from the density scan in Figure 4.7a, as the electron density calibration was done at this point. After the

point of injection, which is indicated by the emission of wave breaking radiation, the wavelength starts to fluctuate from shot to shot. This can mainly be attributed to the strong variation of the length of the first oscillation period, which also effects the second. If the transition to the highly nonlinear blowout or pure bubble regime occurs, only the bubble remains and all following plasma wave periods break, which strongly reduces their amplitude. This can also be seen by analyzing the modulation strength of the second period, see Figure 4.13b. The amplitude of the modulation remains almost constant up to  $x = 1.0$  mm, and then significantly drops and remains at this low level for the rest of the propagation. Hence, by analyzing the modulation strength of the second plasma period after the depletion length, one can predict whether electrons were injected into the plasma wave or not. This was also observed by Buck *et al.* [21].

Compared to the second period, the first oscillation period should undergo an even more dramatic transformation. For the evaluation of the bubble, a sharp shadowgram with good contrast in the bubble front is mandatory, which further reduces the number shots to 65. These remaining shots were binned in 100  $\mu\text{m}$  delay steps and the results are shown in Figure 4.14a. Early in the interaction, the length of the first period has already increased as compared to a linear excitation, which is represented by the blue line, similar to the length of the second plasma wave period, cf. Figure 4.13a. The length of the bubble then

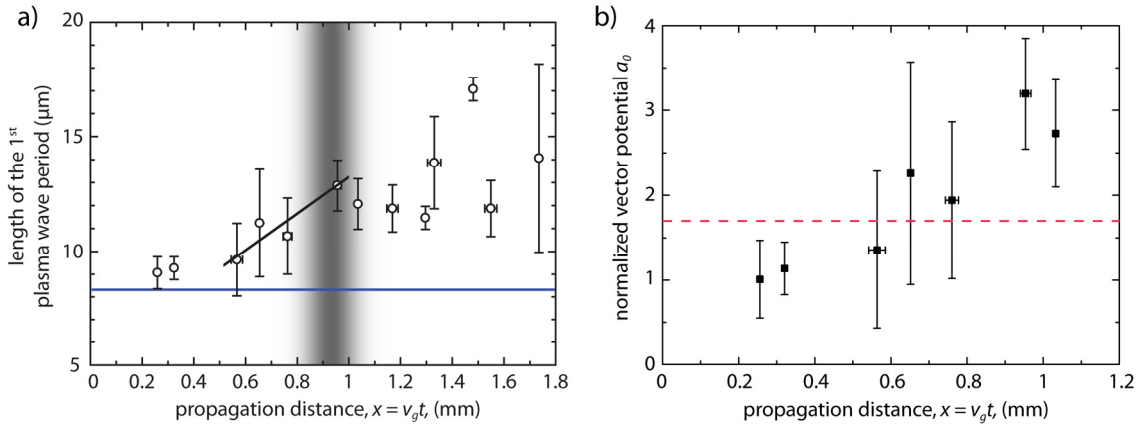


Figure 4.14 | Evolution of the 1<sup>st</sup> plasma period. a) Wavelength as a function of the propagation distance  $v_g t$  taken from the shadowgrams. Error bars represent combination of uncertainty in determining the bubble length and the standard error from averaging. The blue horizontal line is the expected plasma period for  $n_e = 1.65 \cdot 10^{19} \text{ cm}^{-3}$  and linear excitation. b) Retrieved normalized vector potential using Eq. (4.5) from the relative bubble lengthening and estimated vector potential of the pump pulse ( $a_0 = 1.7$  red dashed line).

increases up to the point of wave breaking. A linear regression of the data (black line in Figure 4.14a) shows that the bubble starts expanding from a length of  $(9.4 \pm 1.0) \mu\text{m}$  at an expansion velocity  $v_{be} = (2.4 \pm 1.4) \cdot 10^6 \text{ m/s}$ . The transverse dimension of the bubble, however, remains for the most part unchanged. Thus, the bubble resembles an ovoid

at the point of wave breaking. The fact that a lengthening of the bubble is observed before injection clearly demonstrates that this initial expansion is not caused by the effect of charge loaded into the wake. The lengthening is, in contrast, induced by intensity amplification of the pump pulse. Rearranging Eq. (4.2) results in Eq. (4.5) where the normalized vector potential and, hence, the intensity of the pump pulse can be calculated from the length of the plasma wave period at a given electron density, see Figure 4.14b.

$$I \propto a_0^2 = 2 \cdot \left[ \left( \frac{\lambda_p^*}{\lambda_p} \right)^4 - 1 \right] \quad (4.5)$$

It is apparent that at the beginning of the interaction up to  $x = 0.6$  mm, the retrieved  $a_0$  is smaller than the one estimated in Section 4.1. This result, as well as the observed tilt of the plasma wave's phase front, is a strong indicator that the pump pulse's intensity in the focal plane is reduced due to a pulse front tilt of the pump pulse. As the pulse propagates through the plasma, the intensity increases steadily up to the point of electron trapping. An  $a_0 = 3.2 \pm 0.7$  is reached at this point, which corresponds to an intensity increase by almost an order of magnitude compared to the beginning of the interaction.

After the depletion length is reached the intensity decreases and hence the length of the first plasma wave period decreases as well. Afterwards the length of the bubble varies from shot to shot due to the nonlinear behavior. Depending on the pump pulse parameters, this can lead to, e.g., complete wave breaking and the formation of a single bubble or to the merging of the first two plasma wave periods, as shown in Figure 4.9I. Despite the reduction in intensity due to the depletion of the pump pulse, the length of the bubble remains nearly constant. This is a consequence of beamloading. The threshold charge of  $Q_{\text{tr}} = 200$  pC predicted by Eq. (2.44) would suggest that this effect is negligible. However, when using the actual plasma parameters measured via FCM at the point of injection ( $\lambda_p = 12.5$   $\mu\text{m}$ ,  $k_p \approx 500000$  rad/m),  $Q_{\text{tr}} \approx 40$  pC, which is comparable to the charge recorded in the electron spectrometer.

Using the directly measured lengths of the bubble during injection can also clear the dispute between the detected electron energies and the ones predicted by using Lu's scaling [29]. Crucial for the understanding is the evolution of the pump pulse. Although the intensity at the beginning of the interaction was smaller due to a pulse front tilt, at the point of injection it has increased by nearly one order of magnitude to  $a_0 \approx 3$ . This was achieved by a combination of pulse compression and self-focusing. It is remarkable that this observed threshold value for electron trapping was predicted by Mangles [79] and seems to be a universal quantity in LWFA experiments. While the bubble expands, the dephasing

length increases geometrically. Therefore, the maximum predicted electron energy increases from  $\sim 60$  MeV ( $n_e = 1.65 \cdot 10^{19} \text{ cm}^{-3}$ ) to  $\sim 140$  MeV ( $n_{e,\text{eff}} = 7 \cdot 10^{18} \text{ cm}^{-3} \cong \lambda_p = 12.5 \text{ }\mu\text{m}$ ), which fits the maximum observed electron energies much better. It should be stressed again that the main part of the acceleration has occurred after the depletion of the pump pulse (as defined by Eq. (2.39)).

## 4.6 Transverse wave breaking and transition to the bubble regime

Using the JETi 40 laser at the highest pulse powers and tuning the plasma parameters just above the threshold for self-injection can lead to the generation of a quasi-monoenergetic electron bunch. Besides the spectral characteristics of the generated electron bunch, the plasma wave is completely broken after the first oscillation period, as it was first described by Pukhov and Meyer-ter-Vehn [74]. However, this transition has never been imaged so far, either due to the limitations of the used techniques [25-28] or due to the peak power of the pump pulse, which was not sufficient to reach the bubble regime [21]. Here, an electron density of  $n_e = 1.65 \cdot 10^{19} \text{ cm}^{-3}$  was chosen to be on the threshold for self-injection for helium, producing an electron bunch with energy of 110 MeV and a relative energy spread of  $\Delta E/E \leq 0.05$  with a very small transverse divergence (Figure 4.15). No dark currents are present and the bunch contains a total charge of 6 pC.

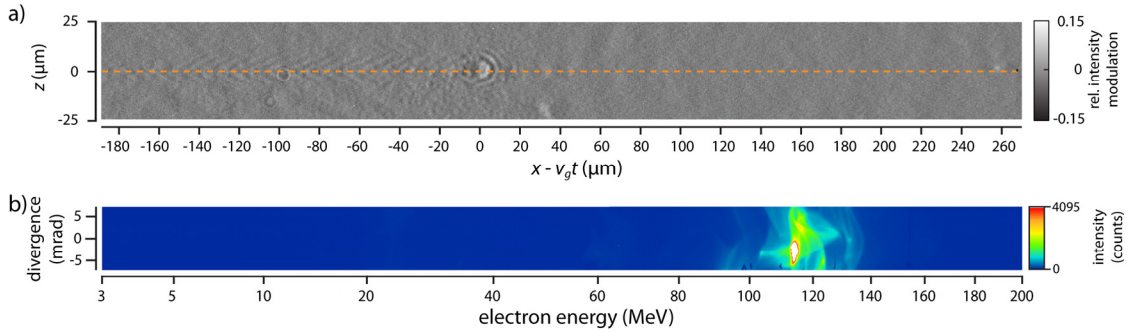


Figure 4.15 | Bubble formation in helium plasma at  $x = 1450 \text{ }\mu\text{m}$ . a) Shadowgram. b) Electron spectrum spectrally dispersed in horizontal direction and spatially resolved in the vertical direction.

The delay between the pump and the probe pulse was adjusted to image the evolution at the position  $x = 1.45 \text{ mm}$ . Using an empirical estimate for the effective acceleration field of  $E_{\text{eff}} = 160 \text{ GV/m}$  and the averaged point of injection at  $x = 0.96 \text{ mm}$  would locate this snap shot into the last third of the acceleration phase. The plasma wave is broken and low amplitude Raman side scattering waves are visible, which are discussed in more detail in Section 5.4. The length of the bubble can no longer be easily determined, since the first plasma oscillation no longer has a distinct shape.



On rare occasions, double bubble structures were observed, see Figure 4.16. There is a slight transversal offset between the two cavities and the spatially resolved electron spectrum reveals a substantial transverse momentum associated with the betatron motion of the electron bunch [33].

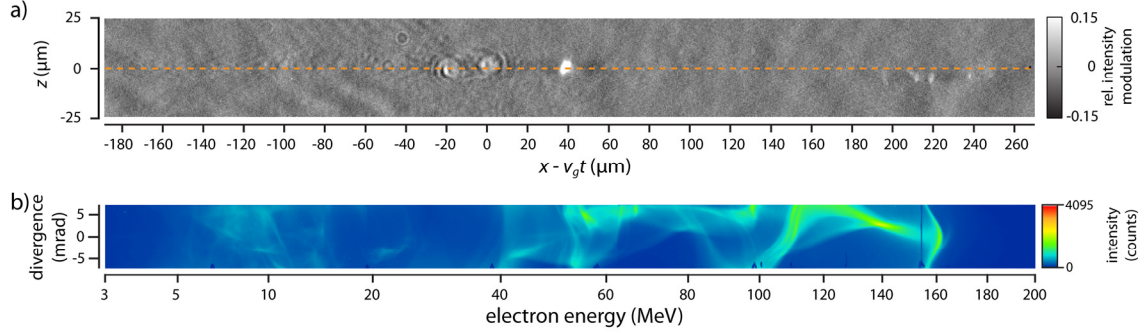


Figure 4.16 | Formation of a double bubble at  $x = 1610 \mu\text{m}$ . a) Shadowgram. b) Electron spectrum spectrally dispersed in horizontal direction and spatially resolved in vertical direction.

## 4.7 Analysis of the wavefront curvature of the plasma wave

The high spatial resolution of FCM allowed retrieval of additional quantitative data apart from the plasma oscillation period. Due to the relativistic motion of the electrons associated with the plasma wave, the wavefront of the plasma wave shows a distinct horseshoe shape with a well-defined curvature. Kalmykov *et al.* [115] have shown that the wavefront curvature increases linearly with distance from the exciting main pulse. This leads to transverse wave breaking and is one possible mechanism for the injection of electrons into the plasma wave. In the weakly relativistic regime, this breaking point can be calculated and is usually located several oscillation periods behind the driving pulse. Increasing the power of the laser shifts these points closer to the front and eventually the power is high enough [78] that the threshold for entering the bubble regime is reached and the plasma wave breaks transversely already after one oscillation.

From the wavefront curvature, the plasma wave amplitude can be derived and from there the acceleration regime, e.g., linear or highly relativistic, can be determined. Here, the plasma wave was recorded after 1 mm of propagation into the gas jet, see Figure 4.17a. The peak energy of the accelerated electron bunch reaches  $E = 180 \text{ MeV}$  suggests that at the time of the snapshot injection had already occurred. The back of the bubble still has the envelope of a parabola but shows some additional substructure, which may be related to wave breaking. For the analysis of the wave front curvature, a parabolic fit was applied to the shape of the wave fronts. The curvature or the inverse radius  $\rho^{-1}$  is calculated from the first derivative of the parabolic fit and plotted for different positions behind the pump pulse (Figure 4.17c). The curvature increases with increasing distance from the



pump pulse due to the variation in the transverse plasma frequency induced by the Gaussian profile of the pump pulse. This was observed by Matlis *et al.* [25] before; however, at much lower plasma wave amplitudes resulting in a curvature almost hundred times smaller. Analyzing the inverse radius of the wave front can give information about

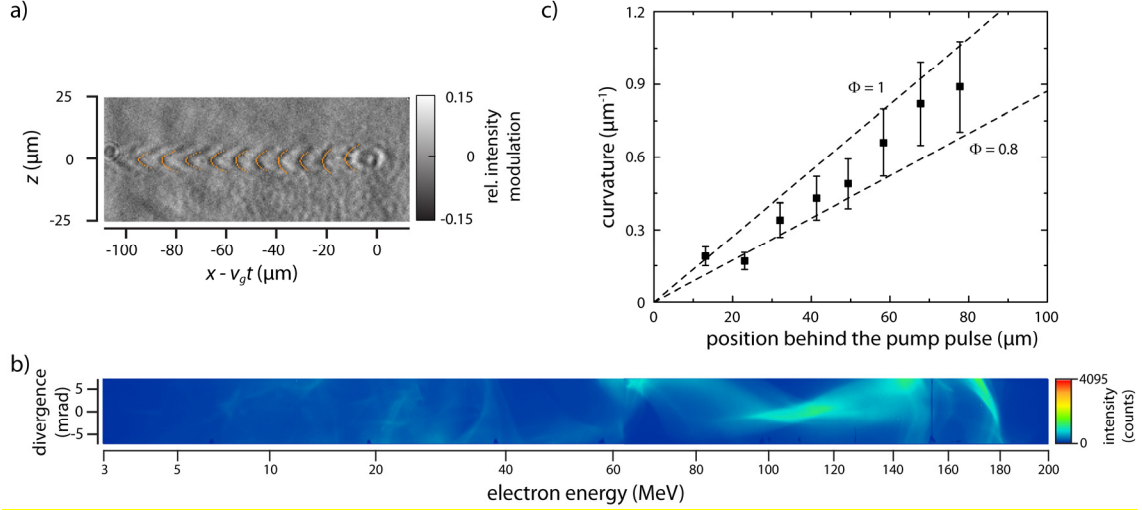


Figure 4.17 | Measuring the curvature of the plasma wave at  $x = 1020 \mu\text{m}$  and  $n_e = 1.65 \cdot 10^{19} \text{cm}^{-3}$ . a) Shadowgram with parabolic fits to the wave's phase fronts determined by regression analysis. b) Electron spectrum spectrally dispersed in the horizontal direction and spatially resolved in the vertical direction. c) Evolution of the wave front curvature behind the pump pulse (black squares). Calculated values for two wake potential amplitudes (dashed lines).

the plasma wave amplitude  $\delta_0 = |\delta n_e(r = 0)/n_e|_{\text{max}}$ . If  $\phi$  and thus  $\delta_0$  approach unity the plasma wave will show a strong modulation resulting in cavities with a very low electron density and peak densities at least twice above the background plasma density as predicted by the nonlinear theory presented in Section 2.8.1. In the weakly relativistic limit, ( $\gamma \leq 2$ ), an analytical expression is given by Kalmykov *et al.* [115]

$$\rho^{-1}(x) = 1.5 \cdot x \cdot \left[ \frac{\phi}{w_0} \right]^2, \quad (4.6)$$

with  $w_0$  being the  $1/e^2$  radius of the focal spot given in  $\mu\text{m}$  and  $\phi$  the amplitude of the electrostatic wake potential normalized to  $m_e c^2/e$  and  $x$  the position behind the pump pulse in  $\mu\text{m}$ . The dashed black lines in Figure 4.17c are simulated values of  $\rho^{-1}$  for  $\phi = 0.8$  and  $\phi = 1$  with  $w_0 = 10.5 \mu\text{m}$  giving an upper and lower bound for the amplitude of the wake potential.

In Figure 4.18a, the wave front is analyzed for a different shot after 1.6 mm propagation into the gas jet. In contrast to the previous measurement, only a low number of electrons were detected in the electron spectrometer. The curvature of the first and second period is stronger compared to the one in Figure 4.17 and remains nearly constant up to the 10<sup>th</sup>

plasma period indicating a higher amplitude of the wake potential, see Figure 4.18a. Afterwards the phase fronts start to overlap due to phase mixing. The strong curvature of the first plasma period suggests a fully blown out electron cavity was generated, see Figure 4.18b. However, the pump pulse seems to be depleted before it could become intense enough to trigger wave breaking and lead to the injection of electrons into the plasma wave.

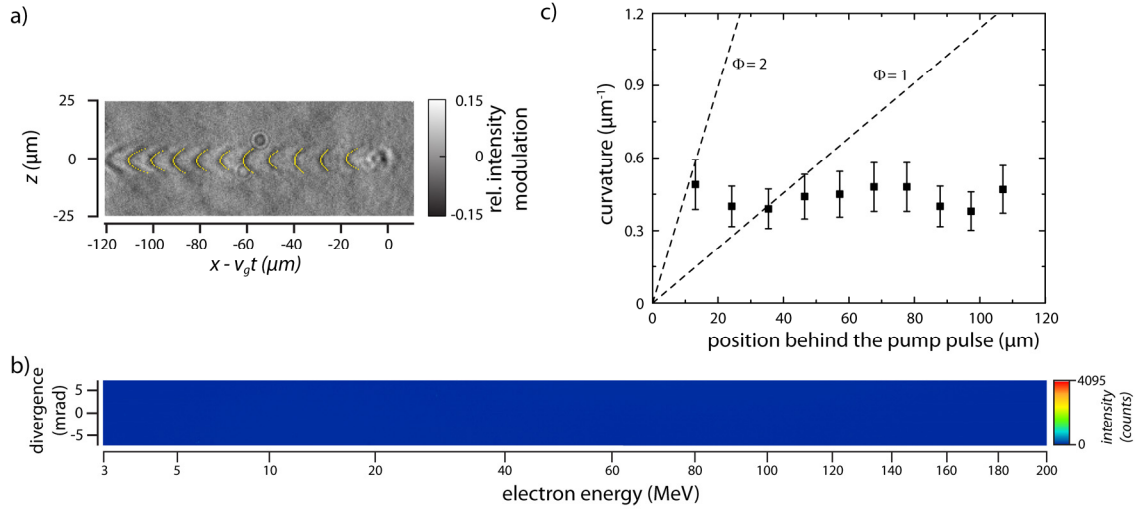


Figure 4.18 | Measuring the curvature of the plasma wave at  $x = 1.6$  mm and  $n_e = 1.65 \cdot 10^{19} \text{ cm}^{-3}$ . a) Shadowgram with parabolic fits to the wave's phase front determined by regression analysis. b) Electron spectrum spectrally dispersed in the horizontal direction and spatially resolved in the vertical direction. c) Evolution of the wave front curvature behind the pump pulse (black squares). Calculated values for two wake potential amplitudes (dashed lines).

## 4.8 3-D PIC simulation including a few-cycle probe pulse

While highly charged, highly energetic electron bunches with narrow energy spread are currently generated routinely in laboratories all over the world, the laser plasma interaction itself still remains somewhat of a black box. Due to the small length and ultrashort timescales, the plasma accelerator itself and the associated plasma wave are challenging to observe. To get an insight into the acceleration, PIC simulations are widely used. Reducing the complexity of the experiment and simplifying to two spatial dimension results in faster computing times. However, after carrying out basic simulations it became apparent that special features of the plasma wave were only reproduced by a 3-D simulation. To generate shadowgrams from the simulated electron density profiles a simple ray tracing algorithm was initially developed. Yet, the retrieved shadowgrams did not match the experimental data, which showed much more detail. This is especially the case at the bubble front, where the electron density gradient is much shallower as compared to the following electron density modulation. Nevertheless, strong brightness modulations appear

in the shadowgrams. This demanded that the propagation of the probe beam and its interaction with the plasma wave be also included in the simulation, which now makes a 3-D simulation mandatory due to the transverse probing geometry. E. Siminos *et al.* have carried out the simulations and the post-processing that are the basis for the following discussion [35] and a more detailed analysis will be published in [116]. The three dimensional particle in cell (3-D-PIC) simulations were performed with the code EPOCH. These simulations are divided into two parts. First, the input parameters for the plasma and the pump pulse were matched to the conditions in the experiment, described in Section 4.1, to get similar properties of the accelerated electron beam, in particular bunch charge and peak energy. Second, the probe beam was included, simulating its propagation through the plasma and the subsequent formation of the probing images.

In this simulation, a laser pulse with  $\tau_L = 36$  fs and  $\lambda_0 = 810$  nm was focused to a spot size with a diameter of  $18.8 \mu\text{m}$  (FWHM),  $300 \mu\text{m}$  into a plasma density profile that matched the experimentally measured one (see Section 4.1) with a peak density  $n_e = 1.7 \cdot 10^{19} \text{ cm}^{-3}$ . In order to take into account imperfections in the experimental focal spot the maximum intensity of the laser pulse was set to  $I_0 = 2.5 \cdot 10^{18} \text{ W/cm}^2$ , leading to similar energies enclosed within the focal spot FWHM in both experiment and simulation [117]. The computational domain was a sliding window of size  $150 \times 70 \times 70 \mu\text{m}^3$  moving at  $c$ . A total of  $2700 \times 525 \times 525$  cells were used with two electrons per cell corresponding to a spatial resolution of  $\Delta x = 0.056 \mu\text{m}$  and  $\Delta y = \Delta z = 0.133 \mu\text{m}$  respectively. A stationary ion background in a fully ionized helium plasma was used. A 6<sup>th</sup> order finite-difference-time-domain scheme was employed, together with 5<sup>th</sup> order particle weighting. At different times in the pump pulse propagation the moving window was stopped and a probe pulse was injected from the side of the box, propagating along the negative  $y$ -direction, while the pump pulse continued its propagation. The probe pulse had a central wavelength  $\lambda_{\text{pr}} = 750$  nm, a transform limited duration of  $\tau_{\text{TL}} = 4.4$  fs and a negative linear chirp that increased its duration to 12 fs for a best match to the experimental images. The influence of the probe pulse's chirp on the formation of the shadowgram is discussed in more detail in [116]. Then, the probe pulse propagated across the wakefield structure, until approximately  $y = -15 \mu\text{m}$ . After that, propagation in vacuum was assumed and modelled in Fourier space including the imaging system aperture, sensor sensitivity and image plane position. To adjust for the latter, the probe pulse was propagated backwards and the time averaged Poynting flux was recorded through the object plane, which in the images presented here was taken to be at  $y = 0$ . The following subsections will focus on the specific results of the simulation.

### 4.8.1 Formation of the shadowgrams

It is important to mention that, even though there is a striking resemblance between the electron density and the retrieved shadowgrams, the shadowgrams are only proportional to the 2<sup>nd</sup> spatial derivative of the electron density. However, the plasma wave exhibits extremely strong gradients that can strongly refract the probe beam so that a high contrast between high density and low density regions is achieved. Nevertheless, not every feature, e.g., the accelerated electron bunch itself, is visible. Even though the local density is quite high in the bunch, so is the  $\gamma$ -factor of these electrons. As shown in Section 2.5, the refractive index of the plasma depends on the plasma frequency and thus on the effective electron mass, which increases with the  $\gamma$ -factor. Therefore, the quantity, which defines the contrast in the shadowgrams or the visibility of the plasma wave is related to:

$$\frac{\omega_p}{\sqrt{\gamma}\omega_{pr}} = \sqrt{\frac{n_e}{\gamma n_c}},$$

with  $n_c$  being the critical electron density for the probe beam. The difference between the electron density retrieved from the simulation and the electron density modified by the relativistic  $\gamma$ -factor is shown exemplary in Figure 4.19.

The difference between the electron density retrieved from the simulation and the electron density modified by the relativistic  $\gamma$ -factor is shown exemplary in Figure 4.19.

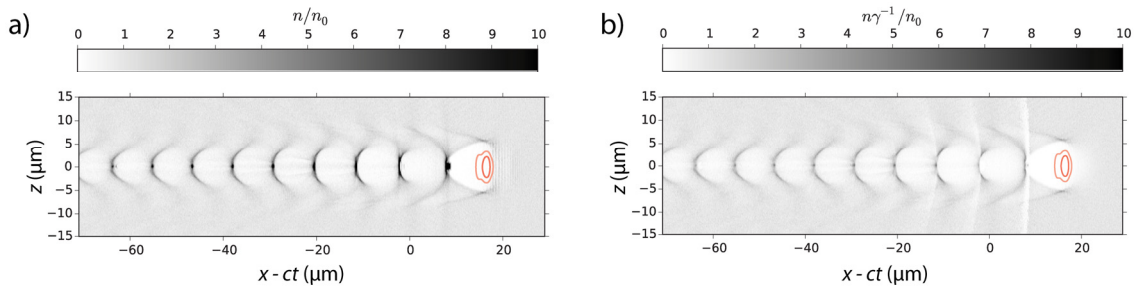


Figure 4.19 | Effective electron density. a) Normalized electron density distribution (greyscale) and the magnetic field of the driving laser pulse (red), b) relativistic corrected electron density  $n_e/\gamma$ .

It is apparent that the accelerated electron bunch has vanished and the central part of the plasma wave has a strongly reduced visibility. At the front of the bubble, where electrons are accelerated by the ponderomotive force of the pump pulse, the density gradient seems shallow. This implies that the bubble front should be hardly visible. This is contrary to the experimental observations where the bubble front actually induces the strongest intensity modulations. To unravel the mechanism behind this phenomenon, the probe beam was tracked by its propagation through the plasma wave.

In Figure 4.20 various snap shots of the probe beam crossing the plasma wave from top to bottom at  $z = 0 \mu\text{m}$  are shown. The contour of the electron density with  $n_e = 2n_0$  is marked in white. First, the probe pulse passes the outer part of the wake structure nearly undisturbed as the electron density gradients are for the most part normal to the incoming beam. However, in the central parts, which exhibit the highest density gradients, parts

of the probe beam are refracted and modulation is imprinted on the probe's intensity profile. As one can see, the structure of the wave is smeared out over the probe due to the probing geometry, but as long as the probe's duration is shorter than half a plasma period the features are not blurred. In the first period, a more detailed substructure can be seen. The electron density gradient at the leading front of the bubble is weaker than in the following oscillations. However, in the shadowgram a strong brightness modulation

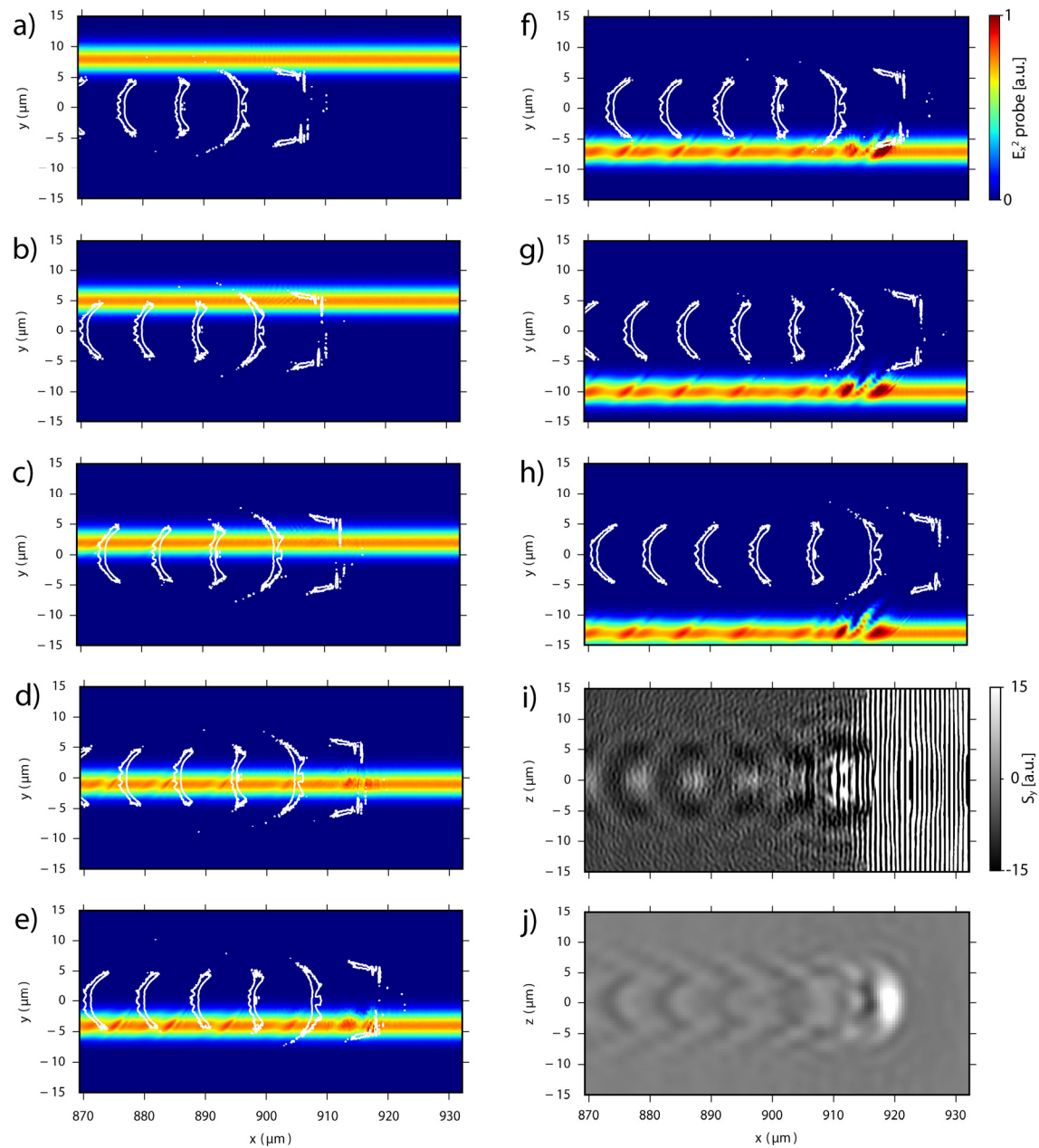


Figure 4.20 | Analysis of the probe propagation through the plasma wake field structure. a-h): The white contour equals  $2n_0$ . The probe pulse is propagating from top to bottom. The momentary intensity of the probe is plotted in rainbow colour scale. i) Calculated shadowgram, j) calculated shadowgram but taken the imaging aperture into account.

is visible. The source for this modulation is still under investigation. For a brief hypothesis

we may consider that in this front region the driving laser pulse interacts with the background electrons as it pushes them out of the region of highest intensity due to the ponderomotive force. However, not all electrons are expelled and some of them experience the ultra high electric and magnetic fields of the driving laser pulse. They are accelerated to velocities close to  $c$  and so the refractive index in this region shows a strong variation, leading to the observed brightness modulation, already present at very short propagation distances, as shown in Section 4.4. Consequently, it would allow direct tracking of the laser pulse in the plasma in the absence of a plasma wave and possibly a direct measurement of the driving pulse's intensity. Note that due to the shape of the front of the bubble and due to the transverse probing geometry, the transverse refractive index distribution is actually mapped out in the longitudinal direction.

It was found by tracking the probe beam through the plasma wave that the probe beam image is only formed by a small part in the center of the wake field. This in turn explains why the structure is so sharply imaged, although the transverse dimension of the plasma wave is on the order of  $10\ \mu\text{m}$ , which is also the characteristic longitudinal extent, i.e., the plasma period. As the central part of the plasma wave causes the primary influence on the formation of the shadowgrams, important quantities like the plasma wave period (see Figure 4.21) can be directly measured from electron density distribution and then transferred to the simulated shadowgrams. It is apparent that the length of the second and the subsequent plasma periods is determined by the minima in the shadowgram.

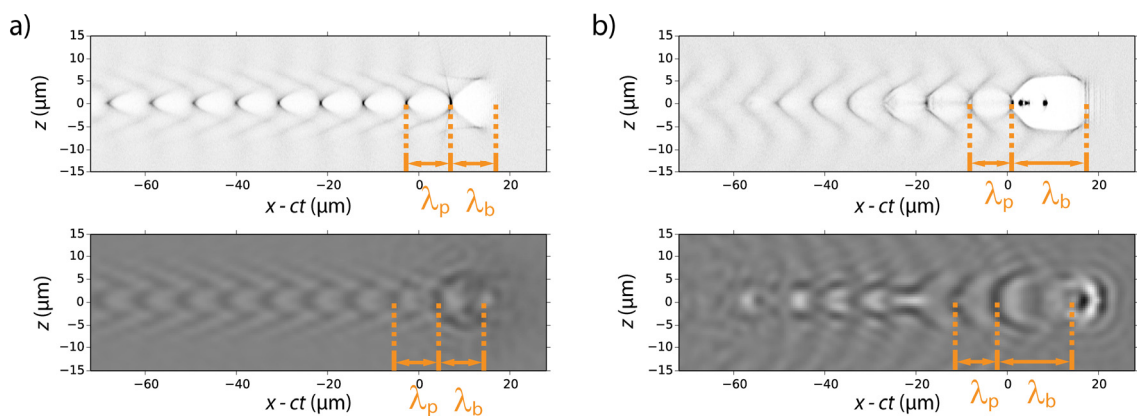


Figure 4.21 | Measurement of the plasma wavelength. Electron density distribution from the simulation (top) and artificial shadowgram (bottom) after a)  $x = 455\ \mu\text{m}$  and b)  $x = 1214\ \mu\text{m}$  propagation. The length of the first, i.e., the bubble, and second plasma period are drawn in at the appropriate positions.

This can also be understood intuitively since those parts of the probe beam traversing the central part of the plasma wave are strongly refracted. However, the length of the first period can only be estimated by the simulated shadowgrams. Depending on the evolution of the pump pulse, strong intensity modulations are present at the front of the bubble.

Thus, the length of the bubble can be determined from the back of the first period to the beginning of the global modulation minimum represented by a black dot.

#### 4.8.2 Temporal evolution of the plasma wave - bubble expansion

Since the parameters for the laser wake field acceleration and the probing setup are included in the simulation the evolution at different time steps could be analyzed. The computed shadowgrams can be directly compared to the recorded shadowgrams. However, the tilt of the plasma wave fronts at the initial, quasi-linear stage of the evolution, which were present in the experiment, was not modelled here. For example, no quantitative information about the pulse front tilt in the plasma was available. A trial and error method for the simulation to include the tilt is a possible approach, but was not performed due to the cost of the very expensive computing time for 3-D calculations. The result is a small discrepancy between the simulation and the experiment up to a propagation distance of  $x = ct = 0.5$  mm. However, key parameters like electron spectrum and bunch charge, as well as the point of injection are in very good agreement. Snapshots of the simulation were taken at six time steps, see Figure 4.22.

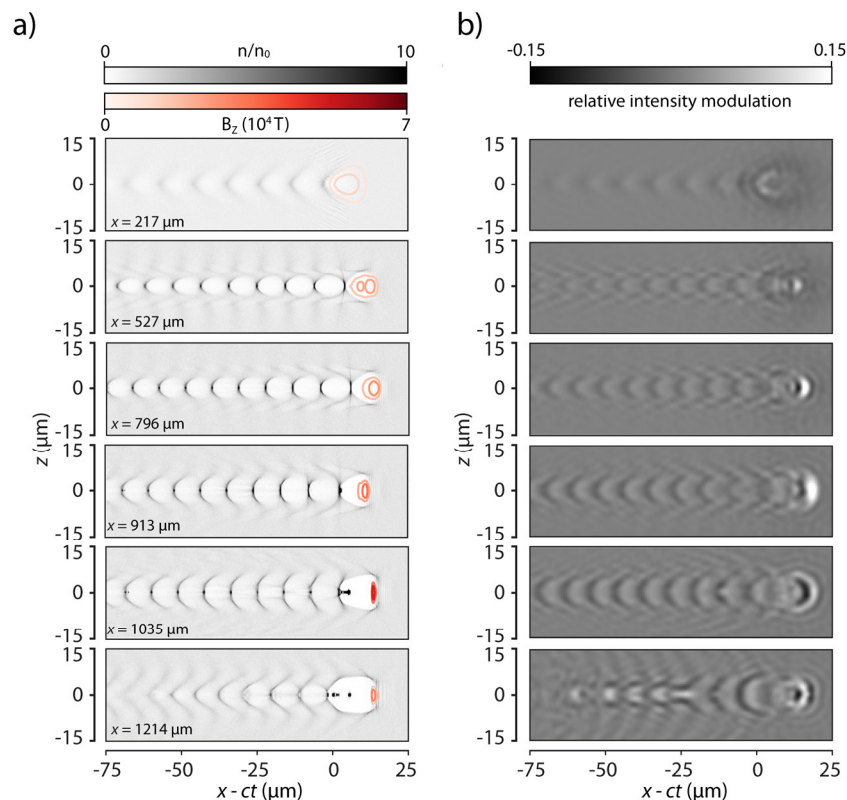


Figure 4.22 | Snapshots of the simulation at different propagation distances. a) Electron density maps (gray) from the simulation at different positions and contours of the envelope of the pump magnetic field  $B_z$  (red) corresponding to 50% and 75% of the maximum value. b) Computed shadowgrams from the simulations in a).



At the beginning of the interaction, the pump pulse has already excited a small amplitude plasma wave. The pump pulse length itself is still on the order of the plasma wavelength. Subsequently, compression leads to an increase in intensity. As the transverse size of the pump pulse is matched to the plasma wave period after passing through the (vacuum) focal plane, the compression mostly occurs in longitudinal rather than in transverse direction. At  $ct = 1035 \mu\text{m}$  the pump pulse also starts to focus further in transverse direction until it depletes. The electron density distribution reveals a similar evolution. As the pump pulse gets more and more intense, the amplitude of the wake field also increases. At the same time, the transverse extent of the plasma wave is slightly reduced. Starting at  $ct = 913 \mu\text{m}$ , electrons are injected into the first period and subsequently accelerated. Additionally, a small amount of charge is injected in the trailing wave buckets. The computed shadowgrams once again manifest the close link between the electron density and the shadowgram. The features of the plasma wave are imaged quite well until very complex shapes arise starting at the middle until the end of the acceleration at  $ct = 1214 \mu\text{m}$ . The overall excellent qualitative and quantitative agreement between simulation and experiment, cf. Figure 4.9, is remarkable. It was already pointed out in Section 4.8.1 and is prominent here as well: the injected electron bunch neither appears in the simulated nor in the experimental shadowgrams. It is also convincing that the brightness modulations at the front of the bubble seem to be connected to the intensity evolution of the pump pulse. As the pump's intensity increases the strength of the modulation increases, too. At the point of injection, the strength of this modulation seems to be highest and then finally decreases after depletion is reached. The same is true for the transverse extent of the modulation, which grows and reduces in a similar way.

Using the electron density distribution from the simulation the length of the first plasma period was taken at various positions during the propagation through the plasma. The simulation also includes data about the local intensity of the pump pulse, therefore, the maximum amplitude of the pump pulse's Poynting vector, which is associated with the local intensity, were calculated as well and is shown in Figure 4.23a. In addition, the total injected charge with kinetic energies above 20 MeV from the PIC simulations is plotted. The intensity increase due to pump pulse compression and self-focusing is small until approximately  $ct = 800 \mu\text{m}$ . Up to that point; the bubble length slowly grows from  $1.2\lambda_p$  to  $1.5\lambda_p$ . After  $ct = 800 \mu\text{m}$  a phase of rapid intensity amplification begins, accompanied by bubble expansion and injection around  $ct = 930 \mu\text{m}$ . At this stage, there is no charge injected yet, hence, the bubble expansion is not due to beamloading but due to intensity amplification of the pump pulse, cf. Eq. (4.2). Significant charge is only injected into the wake after the length of the bubble has started to increase which was also observed previously in simulations [16, 87, 118].



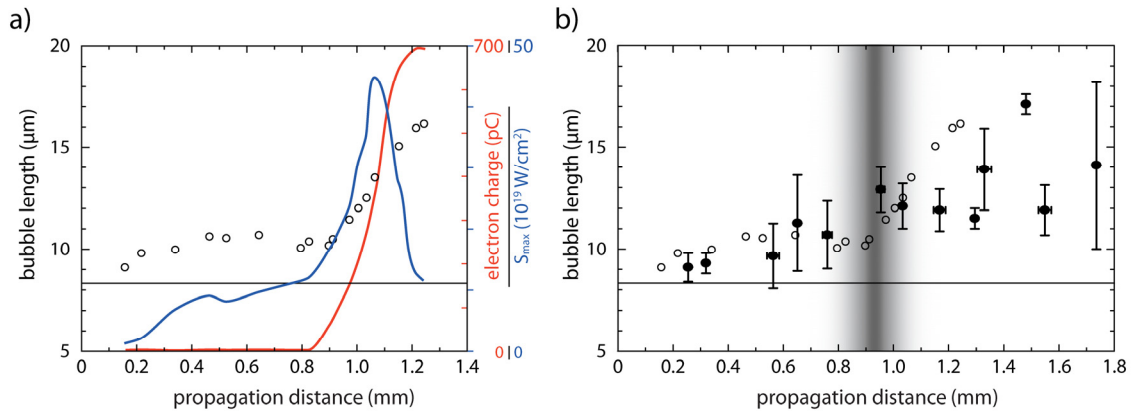


Figure 4.23 | Bubble expansion results from the simulation. a) Bubble length derived from density maps (black circles) and injected charge with energies larger than 20 MeV (red line) from the PIC simulation and maximum instantaneous value  $S_{\max}$  of the Poynting vector magnitude (blue line) from the PIC simulation. b) Bubble length from the simulation (black circles) and from the experiment (black squares)

After  $ct = 1100 \mu\text{m}$ , the pump intensity decreases, while the length of the bubble keeps increasing due to high number of injected electrons altering the wakefield. At approximately  $ct = 1300 \mu\text{m}$ , the simulation shows a merging of the first two periods of the wake due to beamloading, which was also observed in the experiment in some shots, c.f. Figure 4.9l. Compared to the good repeatability of the simulation, the experimental data shows a wider spread of values in Figure 4.23b, in particular after wave breaking. This can be explained by the shot-to-shot variations in the pump pulse's intensity profile as well as gas flow dynamics of the supersonic gas jet.

In summary, the simulation has shown that for the case of unmatched laser-plasma parameters, the pump pulse undergoes several phases of longitudinal and transversal compression until it resonantly excites a plasma wave. Further propagation has eventually increases the pump pulse's intensity by almost one order of magnitude compared to the intensity in the focal plane. The same behavior was also observed in the experiment, cf. Figure 4.23b. This intensity increase leads to the expansion of the first plasma oscillation period and then triggers the injection of electrons into the plasma wave. The lengthening of the bubble is also observed in the computed shadowgrams, which are in excellent agreement with the experimental data and allow reliable determination of the plasma wavelength. In particular, the bubble front, which experiences an unintuitive brightness modulation, is reproduced and it is shown that the modulation amplitude correlates to the intensity of the pump pulse. Since the basics of the formation of the shadowgrams taken by FCM are now understood, this opens the path to interpret more complex plasma phenomena, which are difficult to simulate, such as hosing, soliton formation or stimulated Raman scattering. The latter being the focus of the next chapter.

# 5. Dynamics of the target gas in a LWFA

In this chapter, the influence of the target gas on a LWFA is investigated. In the previous chapter, the dynamics with helium gas, which is used in most electron acceleration experiments, was investigated by shadowgraphy. In this chapter, hydrogen is used as well and the results are compared. From a naïve point of view, the plasma created by a highly intense laser pulse by ionizing either of these gases should have very similar properties. Nevertheless, the plasma dynamics are quite different. They are influenced by the temporal intensity contrast of the pump pulse and depend on the ionization threshold of the different gases. Using shadowgraphy, interferometry and spectrally resolved backscatter diagnostics the underlying dynamics are revealed. This knowledge has been employed to improve the LWFA and has enabled the first application oriented experiment in which in vivo dose response to laser accelerated electron pulses was investigated [32, 36].

## 5.1 Experimental setup

The results in this chapter were retrieved in a number of experiments with the JETi 40 laser system using either the high energy or the few-cycle probe beam. All experiments used the same focusing geometry, laser energy and comparable main pulse duration. The temporal intensity contrast and its influence on the ionization and injection dynamics for helium and hydrogen was the key parameter under investigation. At the same number density, both gases would yield the same electron density when fully ionized. The charge to mass ratios are different but on the relevant time scales, the plasma frequency, the influence of the ions remains negligible. For the considered intensities of  $10^{15}$  W/cm<sup>2</sup> and the ionization energy of 15.43 eV, tunnel (TI) and barrier suppression (BSI) ionization are the dominating ionization mechanisms for hydrogen molecules. The possible intermediate product  $H_2^+$ , which can dissociate into a neutral hydrogen atom and a proton in a few fs would be almost instantaneously ionized. Although the ionization process for hydrogen can be a two-step process, both steps take place in less than the (FWHM) pulse duration of the laser pulse. In some of the experiments, deuterium was used as well but other than a slightly higher ionization energy of 15.47 eV, the femtosecond scale dynamic remains unchanged. For helium, the two ionization levels are further apart. The first is at 24.6 eV and the second at 54.4 eV. For convenience, the ionization energies are converted into the required intensity for BSI and shown in Figure 5.1. In the same figure, the temporal intensity contrast of the JETi40 laser is presented for two settings, high and low. High contrast (HC) refers to a nearly transform limited laser pulse, whereas low contrast (LC) refers to pulses with a residual high-order spectral phase.

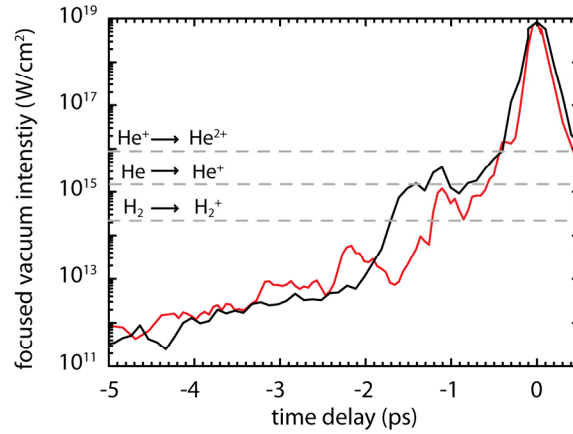


Figure 5.1 | Temporal intensity contrast and ionization thresholds. Temporal intensity profile for low contrast laser pulses with residual high-order spectral phase (black) and for transform limited, high contrast, laser pulses (red). The dashed lines show the intensity thresholds of BSI for  $H_2$ , He and  $He^+$ .

For the two temporal contrast settings, low and high, the main pulse duration was 30 fs (FWHM), as measured with the SPIDER technique [91]. Differences in the picosecond contrast could only be measured by a 3<sup>rd</sup>-order cross-correlation, see Figure 5.1, with the peak intensity scaled to the intensity assumed in the experiment. Optimizing the pulse duration with only the grating separation of the pulse compressor results in an intensity pedestal at  $I = 2 \cdot 10^{15} \text{ W/cm}^2$  starting at  $t = -1.5 \text{ ps}$  before the peak intensity. Starting at  $t = -400 \text{ fs}$ , the intensity rises steeply to the maximum value of  $I_L = 8.3 \cdot 10^{18} \text{ W/cm}^2$ . Using a feedback loop between the SPIDER measurement and the Acousto Optical Programmable Dispersive Filter (AOPDF, fastlite DAZZLER) to compensate for higher order spectral phase terms shortens the picosecond pedestal by 500 fs and reduces its intensity by a factor of four. Using the threshold intensities for field ionization for helium and hydrogen, the momentary position of the main pulse in the plasma can be deduced from the interferograms in combination with the 3<sup>rd</sup> order cross-correlation curve from Figure 5.1. Here, it is important to note that this contrast trace was measured in the collimated beam; however, in the plasma the pulse is focused. Therefore, the local intensity profile before and after the focal plane is modified due to diffraction. For propagation in a homogeneous medium, e.g., a fully ionized plasma, the local intensity increases before and drops behind the focal plane due to natural diffraction. Behind the focus, this would lead to a faster drop of the intensity than measured in the collimated beam and, hence, increases the temporal contrast. Close to the laser axis, however, where the laser intensities and peak power is above the critical power for self-focusing, the laser pulse is guided in the plasma due to relativistic and ponderomotive self-focusing. Hence, no beam divergence occurs for the central part of the laser pulse and the on-axis intensity remains nearly constant. In consequence, the distance between the ionization front and the peak of the laser pulse is decreasing with further propagation distance and the rising edge of the laser pulse steepens.

## 5.2 Laser wakefield acceleration with helium, hydrogen and deuterium

Using helium as the target gas, the position of the gas jet was optimized to get well-collimated electron beams with high bunch charge and kinetic energy. The laser was focused into the leading edge of the gas jet so that a slightly diverging beam enters the central density plateau. This reduces the intensity amplification via self-focusing to just a short position suitable for self-injection [119]. Moving the focal plane further into the gas jet resulted in highly charged electron bunches but with a significantly broader energy spectrum and a higher divergence [32]. During subsequent changes of the target gas, e.g., to hydrogen or deuterium, and during scans of the backing pressure the optimized focal position was kept constant. After every change of the target gas, all tubes for the gas supply were first evacuated and then filled with the pure new gas type several times (relative impurities  $\leq 0.1\%$  for  $H_2$ ,  $\leq 0.04\%$  for He and  $\leq 0.5\%$  for  $D_2$ ). This ensured that ionization-induced injection from any residual high- $Z$  gases like nitrogen [120, 121] could be neglected during the interactions.

### 5.2.1 Results with high contrast laser pulses

First, the electron beam profiles using hydrogen and helium were recorded on a scintillator screen to characterize the total charge, divergence and pointing of the individual bunches. For technical reasons, deuterium was not available for those experiments. For high contrast laser pulses (Figure 5.2), helium and hydrogen show similar averaged electron bunch profiles. Charge and divergence are nearly identical showing a collimated electron beam with a FWHM divergence of 11 mrad in horizontal and 16 mrad in vertical direction. Individual shots showed divergences of down to 2 mrad for both gases while the total charge was higher for hydrogen but less reliable. Although the averaged beam profiles appear similar, they were recorded at different electron densities.

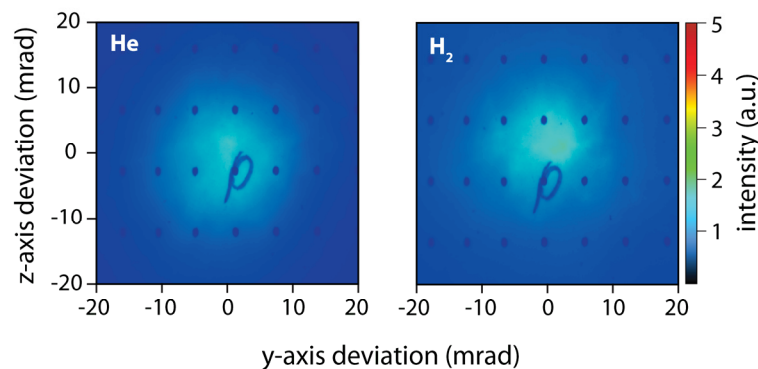


Figure 5.2 | Electron beam profile for HC laser pulses averaged over 80 shots for helium (left) and 40 shots for hydrogen (right). Only shots within a full opening angle of 20 mrad along the laser axis, which is the acceptance angle of the electron spectrometer, and of sufficient charge were considered.

For helium, the optimal results were achieved at  $n_e = (2.0 \pm 0.3) \cdot 10^{19} \text{ cm}^{-3}$ , while for hydrogen the optimum was found at  $n_e = (1.3 \pm 0.2) \cdot 10^{19} \text{ cm}^{-3}$ . This difference is much larger than expected, even if the margins of error are considered, following the discussion at the beginning of this chapter. It is remarkable that the best results for hydrogen were measured at the self-injection threshold, whereas for helium a higher number density is needed. Although the properties of the central electron bunch are similar, hydrogen has a higher electron background signal with a Gaussian distribution created by a second electron component with much higher divergence and thus probably lower energy. The averaged electron spectra also reflect the similar behavior of the two gases, see Figure 5.3 and Table 3. To make the results comparable, the electron density for both gases was set at the empirically found self-injection threshold density. Due to the high shot-to-shot variations in this regime, monoenergetic features appearing in individual shots are smeared out and are not visible after averaging.

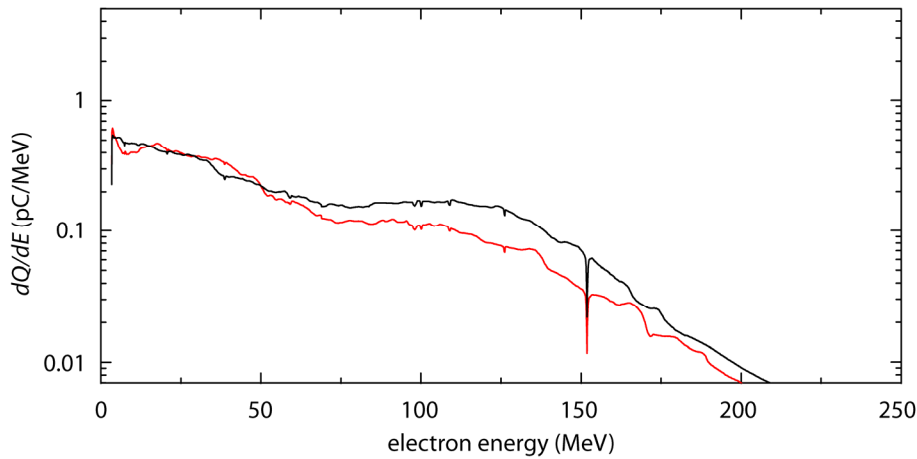


Figure 5.3 | Averaged electron spectrum for helium (black) at  $n_e = (1.65 \pm 0.1) \cdot 10^{19} \text{ cm}^{-3}$  and hydrogen (red) at  $n_e = (1.35 \pm 0.1) \cdot 10^{19} \text{ cm}^{-3}$  for HC laser pulses. The cut in the spectrum at 150 MeV is caused by two adjoined scintillator screens in the electron spectrometer.

The total charge of the averaged electron spectrum in the range from 3 MeV to 200 MeV for helium is 34.2 pC compared to 29.5 pC for hydrogen. The primary difference comes from the charge in the range from 70 MeV to 200 MeV, see Table 3. In this energy range, the total charge for hydrogen is 8.4 pC and for helium 13 pC. The higher total number could be explained by the higher background density (1.2 times higher for helium), which would allow for a higher number of trapped particles.

Gas	Total charge Q (pC)	Q in 70-200 MeV	$n$ , minimum charge
hydrogen	29.5	8.4	#40, 9 pC
helium	34.2	13	#80, 9 pC

Table 3 | Electron bunch properties retrieved from the spectrometer and averaging parameters for HC laser pulses.

In summary, for a high laser pulse contrast the averaged electron beam profiles and electron spectra look very similar at the optimal electron density. However, for the results with helium a higher electron density was needed. Although the averaged beam profiles and spectra look strikingly similar, individual best shots with hydrogen show a higher electron bunch energy and charge.

## 5.2.2 Results with low contrast laser pulses

The same experiment as in the previous section was also performed with a low laser pulse contrast (LC). Exemplarily, averaged electron beam profiles are shown in Figure 5.4. Using helium as the target gas at an optimized plasma density of  $n_e = (1.3 \pm 0.1) \cdot 10^{19} \text{ cm}^{-3}$  resulted in a collimated electron beam with a FWHM divergence of 11 mrad in the horizontal and 16 mrad in the vertical direction, similar to the experiments with HC laser pulses. The pointing stability is 7 mrad rms in the horizontal and 9 mrad rms in the vertical direction. Changing the gas to hydrogen at a plasma density of  $n_e = (1.6 \pm 0.1) \cdot 10^{19} \text{ cm}^{-3}$  results in a doubling of the electron bunch charge and a reduction in divergence to 6 mrad in horizontal direction and 8 mrad in vertical direction. Individual shots showed divergences of less than 1 mrad. Notable at this point is that in the averaged bunch profiles of hydrogen and deuterium a higher background signal with Gaussian distribution is present, similar to the result with hydrogen using higher laser intensity contrast.

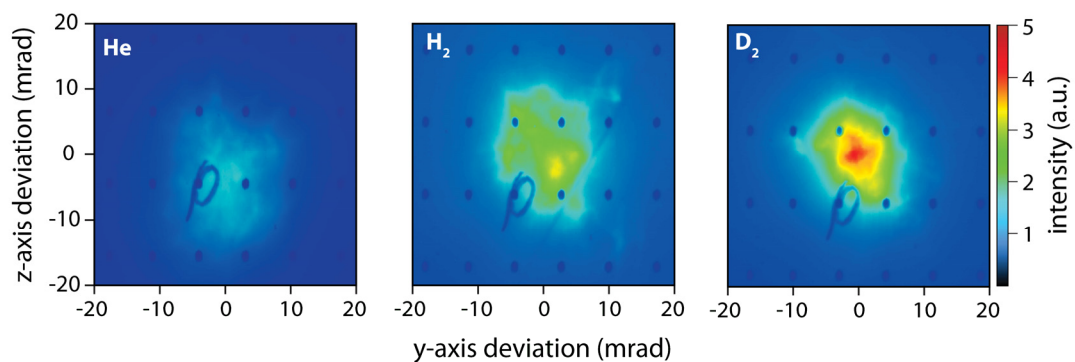


Figure 5.4 | Electron beam profiles at the scintillator screen within a full opening angle of 20 mrad averaged over 30-40 shots for helium (left), hydrogen (center) and deuterium (right) for low contrast pulses.

Considering that the intensity scales in Figure 5.3 and Figure 5.4 are the same; comparing the LC results with the HC results shows that helium gives very similar beam profile results at a smaller background electron density. However, the most apparent difference is for hydrogen where more charge in a beam with smaller divergence is accelerated. The optimal electron density is a little bit higher than for the HC laser pulses. Helium and hydrogen should give similar plasma parameters as pointed out in Section 5.2, hence the difference seem to be rooted in the acceleration dynamics. Helium has a higher ionization threshold

but also a higher charge to mass ratio for the core ions. To distinguish between these two effects, experiments with deuterium have been carried out. Deuterium has a similar ionization energy as hydrogen but the same charge to mass ratio as helium. This allowed to investigate the influence of the background ions. When using deuterium similar results as for hydrogen were received but the pointing stability has improved further down to 3 mrad rms both in the horizontal and the vertical direction. Therefore, the charge area density of the electron pulses when using deuterium gas increased nearly by a factor of five as compared to helium gas. The difference between the three gases can also be seen in the averaged electron spectra, see Figure 5.5 and Table 4. The results for helium are quite similar to the results with HC laser pulses when comparing the overall charge as well as the distribution in the range from 70 MeV to 200 MeV. For hydrogen and deuterium, the recorded charge has more than doubled compared to the experiments with HC laser pulses and now reach an average of  $> 65$  pC per shot.

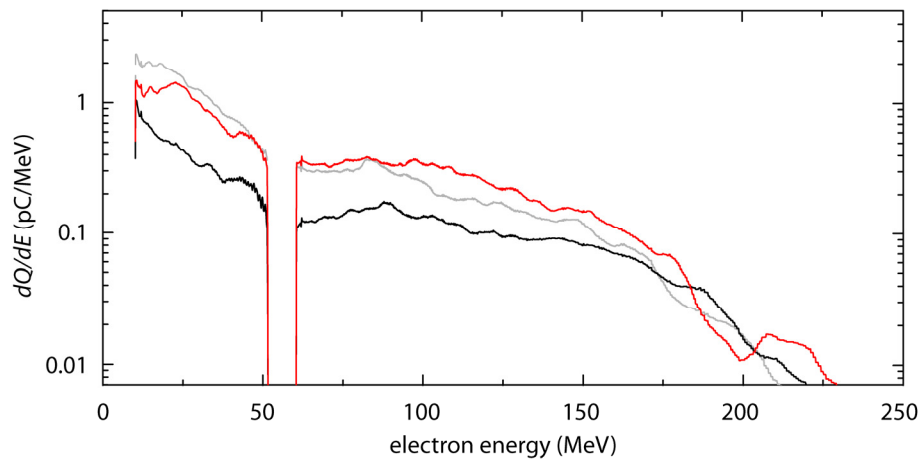


Figure 5.5 | Averaged electron spectra for helium (black, 96 shots) at  $n_e = (1.65 \pm 0.1) \cdot 10^{19} \text{ cm}^{-3}$ , hydrogen (red, 50 shots) at  $n_e = (1.35 \pm 0.1) \cdot 10^{19} \text{ cm}^{-3}$  and deuterium (light grey, 60 shots). The gap in the spectrum around 60 MeV corresponds to a physical gap between two scintillating screens used in the spectrometer.

The spectral distribution differs between the two gases as deuterium has a higher charge in the range between 10 MeV and 50 MeV, while hydrogen nets a higher charge starting from 90 MeV. This high average charge and the good collimation of the electron bunches was used in an experiment investigating the in vivo dose response of biological tissue to laser generated electron beams. For a time span of over four weeks, a stable electron beam had to be provided and characterized on a daily basis. Details are published in [32]. Despite the one year difference between the irradiation experiment and the results in Figure 5.4 and Figure 5.5, the characterization yielded the same average bunch charge. Individual shots with  $Q > 250$  pC were also recorded. The collimation of the electron

bunches actually was too good, and required a 1mm thick aluminum sheet as a scatter target to homogenize the beam profile for the cell-irradiation experiment.

Gas	Total charge $Q$ (pC)	$Q$ in 70-200 MeV	n, minimum charge
hydrogen	67.8	25.4	#50, 7.5 pC
helium	29.8	11.9	#96, 4.0 pC
deuterium	74.1	19.7	#83, 6.0 pC

Table 4 | Electron bunch properties retrieved from the spectrometer and averaging parameters for LC laser pulses.

Although the difference in the accelerated electron beam parameters between helium and hydrogen is so prominent, they are nowhere published in the literature. It is expected that the charge to mass ratio is more important for longer pulses, with  $\tau_L \approx 2\pi\omega_I^{-1}$ , with  $\omega_I$  being the ion plasma frequency. The relevant time scale for LWFA is the electron plasma period, which for hydrogen is at least a factor 45 shorter than the ion plasma period. This and the previous results point to the ionization threshold as the key difference between hydrogen and helium. To investigate the dynamics of the two gases, transverse probing as well as backscatter diagnostics were employed. Combining the results of both suggest that laser-plasma instabilities, which are typically neglected for short laser pulses, play a central role.

### 5.2.3 Results from interferometry

The refractive index profile of the plasma can be measured via interferometry, cf. Section 3.4.1. From this data, the background electron density can be derived, which is a fundamental parameter in LWFA. Special care has to be taken concerning the propagation effects of the probe pulse through the plasma as the investigated object moves nearly with the speed of light [104]. The recorded integrated phase shift accumulated by the probe beam is not solely a transversal cut through the plasma's profile but it is rather taken under  $45^\circ$  as both the pump and the probe propagate at the same velocity. Even if few-cycle probe pulse are used, this propagation effect as well as the large lateral extension of  $\Delta x \approx \Delta y \gg c\tau_{pr}$  leads to blurring. Details of plasma structures with sizes below a couple of 10s of  $\mu\text{m}$  cannot be resolved without using advanced techniques like tomography. Using interferometry to measure the modulation of the electron density inside a plasma wave is even more challenging since the additional phase shift compared to the background is quite small. Assuming a plasma wakefield with a diameter of  $10 \mu\text{m}$  in the bubble regime, i.e., full cavitation ( $n_e \ll n_{bg} \approx 10^{19} \text{ cm}^{-3} \rightarrow \eta = 1$ ) and walls with the thickness of the skin depth ( $c/\omega_{pw} \approx 0.5 \mu\text{m}$  with  $n_e \approx 10^{20} \text{ cm}^{-3}$ , cf. Section 4.8.1) results in a net phase shift of  $\Delta\phi \approx 10 \text{ mrad}$  compared to a homogeneous plasma at  $n_{bg} = 1.65$



$\cdot 10^{19} \text{ cm}^{-3}$ . At the same time, the steep density gradients in the plasma wave result in an amplitude modulation and thus the requirements for interferometry, e.g., a pure phase object, are no longer fulfilled. Hence, it is more convenient to use longer probe pulses with higher pulse energy to outshine any scattered light from the pump pulse to record undisturbed interferograms. However, no shadowgrams of the plasma wave were available. Depending on the threshold ionization intensity for the used gas and the transverse profile of the pump pulse, the transverse diameter of the plasma column ranges from 100  $\mu\text{m}$  to 300  $\mu\text{m}$ . Figure 5.6. presents by interferometry retrieved refractive index profiles from representative shots from experiments using hydrogen and helium target gases with high and low intensity contrast, as defined in Section 5.1.

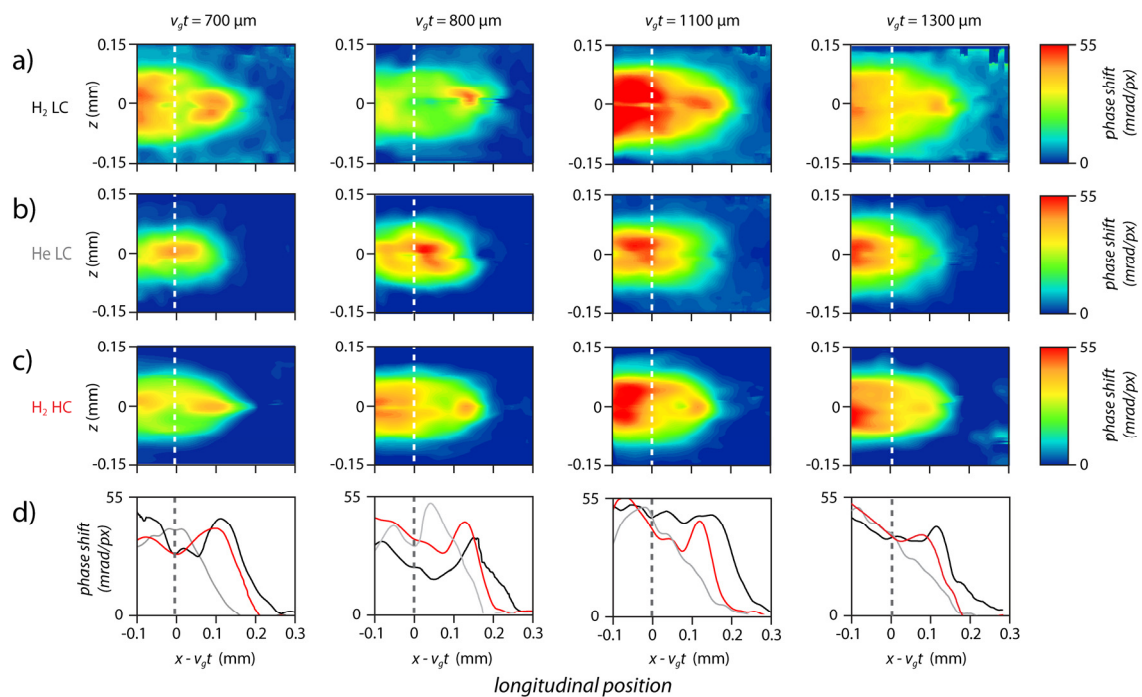


Figure 5.6 | Retrieved phase shift of the probe beam from the interferograms a) hydrogen, LC, b) for helium, LC and c) hydrogen, HC. The profiles in d) were taken along the  $z = 0$  axis with helium (grey), hydrogen HC (red) and hydrogen LC (black).

The laser pulse enters the 3 mm long gas jet at a distance of 1.25 mm above the nozzle's exit. The interferograms are taken at different time steps during the evolution. The position of the pump pulse was determined by using the temporal intensity profile from Figure 5.1. For this modified longitudinal intensity profile the ionization rate equations were solved for hydrogen and helium according to [122]. The ratio of the electron density between hydrogen and helium after 800  $\mu\text{m}$  propagation at -600 fs, i.e., 200  $\mu\text{m}$  before the main pulse (Figure 5.6, second column) are consistent with the calculations from the ionization rates above. Hence, it is feasible to determine the position of the FWHM main pulse, marked in Figure 5.6 (white dashed line), by computing temporal intensity profiles

of the pump pulse during the propagation, the gas's ionization rate equations, and the interferometrically retrieved data. Further measurements presented in the Master thesis of D. Ullmann [123] verified this method by recording shadowgrams including the position of the plasma wave and interferograms in the same shot.

For all three experiments in Figure 5.6, there is a local minimum in the refractive index profile at the position of the driving laser pulse for propagation distances  $v_g t < 1.3$  mm. Whether this minimum in the refractive index profile can also be associated with a minimum in the electron density profile is the main topic in the following discussion.

One has to keep in mind, that the electron density is retrieved from the phase shift recorded by interferometry. The phase shift accumulated by the probe beam is described by the refractive index of the plasma, given by

$$\eta(\omega_p) = \sqrt{1 - \omega_p^2 / (\gamma \cdot \omega_L^2)} \quad (5.1)$$

for a non-magnetic plasma, far away from resonances. For non-relativistic electron energies and underdense plasmas the refractive index can immediately be associated with the electron density. Using laser pulses with low contrast, the hydrogen plasma (Figure 5.6a) is formed at earlier times than the helium plasma (Figure 5.6b), as it is expected from the lower ionization level. The gradient of the plasma density at the ionization front is steeper for hydrogen, because ionization and subsequent dissociation and additional ionization occur at the same intensity. The full ionization of helium is a double-staged process and requires a higher laser intensity than is needed for hydrogen. The transverse diameter of the hydrogen plasma is 200  $\mu\text{m}$ , while for helium the diameter is only 140  $\mu\text{m}$ , which is due to its higher ionization threshold. The transverse extent of the plasma also depends on the quality of the laser focus. Higher order aberrations cause a non-Gaussian lateral distribution of the focus intensity. For high contrast laser pulses and with hydrogen as the target gas (Figure 5.6c), the onset of ionization is slightly delayed and the gradient of the rising edge is even steeper. A lineout along the propagation axis for each configuration is shown in Figure 5.6d. The profile of the refractive index for all three experiments shows a strong modification from a homogeneous plasma and is heavily modulated. During the laser pulse's propagation into hydrogen gas, the rising edge of the laser pulse ionizes the gas but there is an apparent minimum in the phase shift between the peak of the pulse and the ionization front. It is most pronounced in hydrogen gas with low contrast pulses. For high contrast pulses in hydrogen, this feature is reduced and is rarely present in helium. The modulation depth of this minimum decreases after propagation  $v_g t = 800$   $\mu\text{m}$  for hydrogen LC and is gone at  $v_g t = 1.3$  mm.

This modulation is interpreted as follows. The width of the plasma column remains constant over the longitudinal extent of the measured depression in phase shift. The depression itself is spatially localized in front of the main pulse. After the peak of the pulse has passed, the apparent dip in the refractive index density vanishes. Hence, any lateral expansion of the plasma, which would not lead to a temporal but to a permanent decrease in on-axis density, can be excluded. Considering an oscillation rather than an expansion would result in a temporal period of a few 100 fs. No plasma effect is known so far, which would explain this behavior for laser pulses as short as the ones that were used in the experiment.

As it can be seen in Eq. (5.1), the refractive index only depends on the plasma frequency and the  $\gamma$ -factor of the plasma electrons. An increase in  $\gamma$  would lead to an increase in the refractive index. Therefore, the smaller phase shift in front of the main pulse is presumably not due to a reduction in electron density, but due to an increase of the  $\gamma$ -factor of the plasma electrons. In the case of hydrogen, the reduction of the refractive index in Figure 5.6a after  $v_g t = 800 \mu\text{m}$  can be explained if background electrons with a density of  $n_e = 1.5 \cdot 10^{19} \text{ cm}^{-3}$  and  $\gamma \approx 1.6$ , i.e., a kinetic energy of  $E_{\text{kin}} \approx 300 \text{ keV}$ , are considered. In conclusion, the measurement of the refractive index profile for hydrogen and helium shows modulations, which are most prominent for low contrast laser pulses in hydrogen. Following the arguments given above it is quite likely that this reduction in the phase shift is not due to a reduced electron density but rather due to a heating of the background electrons at this position. After a couple of Rayleigh lengths ( $Z_R \approx 150 \mu\text{m}$ ), the retrieved longitudinal phase profile is for the most part smooth and the dip has vanished. For underdense plasmas and low intensities (between  $10^{15} \text{ W/cm}^2$  and  $10^{17} \text{ W/cm}^2$ ) stimulated Raman backscattering can efficiently heat/accelerate electrons up to  $\gamma \approx 2$  [56, 124]. This plasma instability will be the topic in the next sections.

### 5.3 Backscattered spectra for helium and hydrogen

During the interaction of the pump pulse with the plasma, photons are scattered in many directions depending on the scattering process. Thomson scattered light is mainly scattered perpendicular to the polarization of the pump pulse. Raman backscattered light is scattered anti-parallel to the pump pulse's propagation and gives information about the plasma frequency directly at the position where the pump pulse was scattered. The focusing parabola was used to re-collimated any backscattered light from the gas jet, see Figure 5.7. The last mirror before the parabola was used to suppress any pump light and only wavelengths above 880 nm and below 720 nm are transmitted with an efficiency  $> 50 \%$ . The transmitted light was then focused into a glass fiber coupled to a spectrometer. In the case of Raman backscattering, the pump pulse is shifted to longer wavelengths, hence the minimum shift that could be recorded with this setup is 70 nm. This would

correspond to a plasma density of  $n_e = 8 \cdot 10^{18} \text{ cm}^{-3}$ . However, there may still be red shifted parts of the pump pulse generated by (relativistic) self-phase modulation, which is scattered into the backward direction as well and is strong enough to outshine the weakly scattered signal.

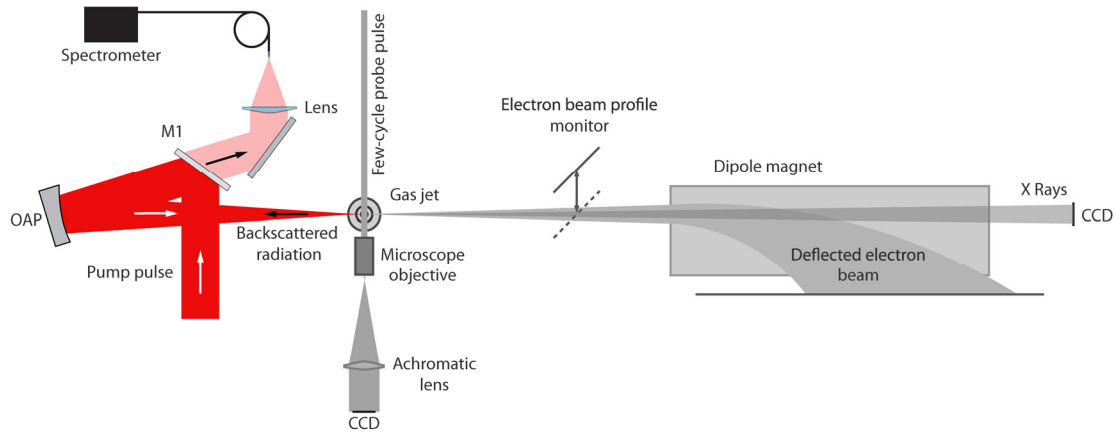


Figure 5.7 | Setup for backscatter diagnostic. M1: mirror with high transmission for  $\lambda = (740 \dots 850) \text{ nm}$ ; OAP: silver coated off-axis parabolic mirror, Lens to focus the backscattered light into the fiber attach to the spectrometer.

In the experiment, high contrast laser pulses with a spectral distribution at full power as shown in Figure 5.8a were used. The fundamental spectrum is highly red shifted due to saturation in the power amplifier. Although the central wavelength is at  $\lambda_0 = 810 \text{ nm}$ , the highest spectral intensity and therefore the highest probability for backscattering is for even longer wavelengths. To separate the backscattered signal from other sources and from noise, a Gaussian fit was applied to the recorded backscattered signal and the wavelength shift determined. The backscattered signal for hydrogen and helium at an electron density  $n_e = 2.1 \cdot 10^{19} \text{ cm}^{-3}$  is shown in Figure 5.8b. The FWHM of the backscattered spectrum ( $\Delta\lambda = 22 \text{ nm}$ ) is used to determine the central frequency of the effective scattered fundamental spectrum. It is assumed that only the highest intensities of the fundamental spectrum contribute and that the width of the backscattered spectrum is taken from the red part of the fundamental spectrum to get the effective scattered fundamental wavelength  $\lambda_{\text{eff}} = 822 \text{ nm}$ . The central wavelength of the back scattered signal was determined by the displacement parameter of the Gaussian fit-function. It was found that hydrogen as a target gas gives a signal nearly one order of magnitude stronger than helium. However, the relative shift is the same for both gases with a peak for hydrogen at  $\lambda_{B,H_2} = (903.5 \pm 0.5) \text{ nm}$  and for helium at  $\lambda_{B,He} = (904.2 \pm 0.4) \text{ nm}$ , which is smaller for both gases than  $\lambda_B = 926 \text{ nm}$  expected from linear Raman backscatter theory. To get a full picture of this issue, the spectra for hydrogen and helium for different electron densities are shown in Figure 5.9. Due to technical reasons, the spectra were taken at the same backing pressures for the gas jet, which results in different electron densities for helium and hydrogen due a difference in the velocity of sound, cf. Section 3.2. Increasing the

electron density also increases the amplitude of the backscattered signal. This effect is more pronounced for helium than for hydrogen. However, the spectral shift is still the same for hydrogen and helium at identical electron densities.

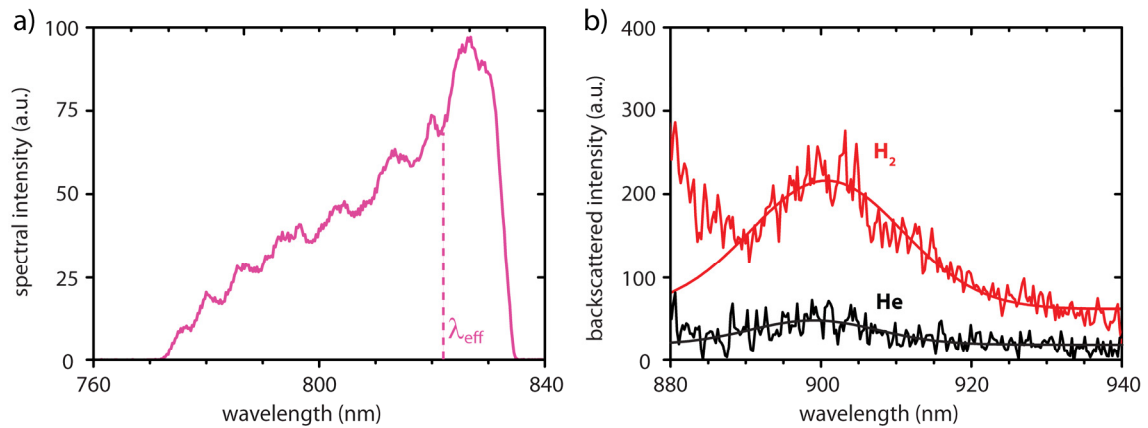


Figure 5.8 | Backscatter analysis. a) Fundamental laser spectrum at full power with effective scatter wavelength b) Comparison of the intensity of the back scattered light for hydrogen (red) and helium (black) at an electron density of  $n_e = 2.1 \cdot 10^{19} \text{ cm}^{-3}$ .

The central wavelength of the backscattered light is indicated by the black dots in Figure 5.9. Even for increasing electron density, the shift seems nearly constant. This becomes more obvious, when the shift is plotted in terms of angular frequency over the electron density. This is done in Figure 5.10 and using data from Figure 4.7. There, the discrepancy between linear backscattering theory and the experimental data becomes evident. Hydrogen and helium data show a good agreement in their overlapping electron density ranges besides the different amplitudes of the backscattered signal. Both show a strong

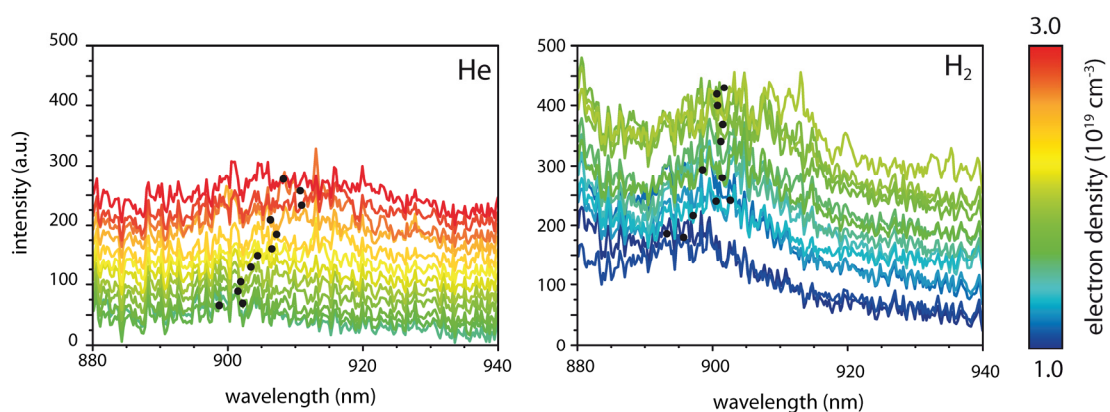


Figure 5.9 | Backscattered spectra for helium (left) and hydrogen (right) for different electron densities. The black dots mark the central wavelength according to a Gaussian fit. For better visibility the spectra are shifted in the vertical direction with respect to each other.

deviation from the linear theory starting at an electron density  $n_e = (1.3 - 1.5) \cdot 10^{19} \text{ cm}^{-3}$ . A similar behavior was observed by Matsuoka *et al.* [107]. There it was suggested that the

deviation from the linear regime can be explained by taking the  $\gamma$ -factor connected to the pump pulse's intensity into account,  $\gamma = \sqrt{1 + a_0^2/2}$ , and using the relativistically corrected plasma frequency  $\omega_p^* = \omega_p/\sqrt{\gamma}$ . Applying  $a_0 = 1.7$  from the experiment nets a fixed correction factor of  $\sqrt{\gamma} = 1.25$ , which would be still not sufficient to match the experimental data. The actual intensity of the laser pulse has to be much higher and depend on the electron density to explain the experimental findings. A similar deviation from the stationary linear theory was also observed for the plasma period in Section 4.3. Using the values obtained there for the effective plasma frequency  $\omega_p^*$  directly measured with FCM gives the blue squares in Figure 5.10. The agreement with this set of data is much better including the point at which the deviation from the linear Raman scattering theory occurs.

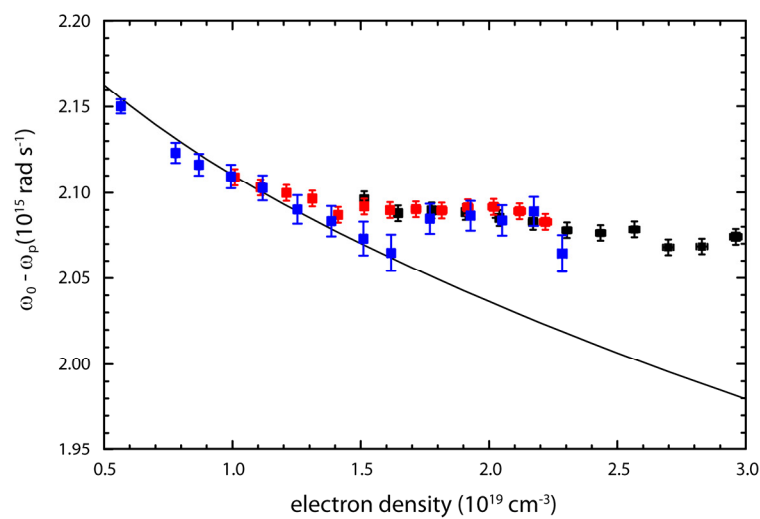


Figure 5.10 | Angular frequency shift of the backscattered radiation for hydrogen data (red squares) and helium data (black squares). The black solid line is the simulated shift using linear Raman theory and  $\omega_0 = 2.29 \cdot 10^{15}$  rad/s ( $\lambda_{\text{eff}} = 822$  nm). The blue data points are retrieved by using  $\omega_p^*$  measured in Section 4.3, Figure 4.7

From the previous considerations it can be concluded: The laser pulse undergoes substantial intensity amplification, which can be indirectly measured either by the shift of the backscattered radiation due to the Raman effect or directly measured by the plasma period and, hence, the plasma frequency via FCM. At this point, it has to be stressed, that SRS-B is influenced by the pump's intensity at the bubble front where the pump pulse excites the plasma wave and radiation is backscattered, while shadowgraphy measures the effect in the following plasma periods. In the high contrast experiments discussed here, where hydrogen and helium deliver very similar results in electron bunch properties, the overall plasma wave evolution strongly depends on the evolution of the pump pulse and the plasma density and temperature. However, the amplitude of the backscattered radiation is much stronger for hydrogen and some indication for this difference could be expected in the shadowgrams.

It is remarkable that the data from the plasma wave measurement, which was taken right at the point of injection at a very specific position in the pump pulse's propagation shows such a good agreement to the data from a temporally and spatially averaged measurement such as the backscattering radiation. It is to be expected that the growth rate for SRS-B is peaked at two points in the evolution of the pump pulse. The first is at the beginning of the interaction before the vacuum focal plane is reached, since the intensity of the pump is still low and its spectrum comparable narrow. However, the observed tilt in the plasma wave would suggest that the backscattered radiation is propagating under a sufficiently large angle; hence, the radiation is not collected by the parabolic mirror. After passing through the focal plane, lower intensity parts of the pump pulse are not self-focused and diffract after a few Rayleigh lengths, which leads to a steepening of the pump pulse's leading edge and thus prohibits the growth of the instability. Nevertheless, SRS-B can grow again, once the pump pulse is depleted due to the lower intensity and the large wave vectors. In the here described experiment the position of wave breaking, i.e., injection of electrons and depletion are very close together, which can explain the good agreement between the shift in the backscattered radiation and the lengthening of the plasma wavelength.

These results underline once more, that the relativistically corrected plasma frequency is the key parameter in LWFA and has to be measured properly to provide a comparison between experimental data and simulations or analytical models. The evolution of the laser pulse due to self-focusing and self-compression has a huge influence on the actual pump pulse intensity and has to be taken into account rather than using the vacuum pulse intensity and background electron density. The very strong signal from SRS-B raises the question as to whether or not these waves can also be observed in the shadowgrams. This will be the topic of the next section.

## **5.4 Time-resolved shadowgraphy with helium and hydrogen**

To get further insight into the experiments with helium and hydrogen gas, the FCM setup was used with high contrast laser pulses. Besides a stronger backscattered signal, the interaction in the two gases yielded a rather similar outcome in electron bunch parameters. Operating at the threshold density for self-injection for both gases the propagation of the pump pulse was tracked through the gas jet. The focus of the analysis for the selected images relies on specific differences between the two gases with representative shadowgrams shown in Figure 5.11 at the threshold for self-injection. Images were selected to compare the acceleration at different evolution steps with similar electron spectra. In helium, a long plasma wave with more than 10 oscillations is generated directly from the beginning of the interaction with the gas, see Figure 5.11a. The phase fronts of the plasma



wave are tilted due to a pulse front tilt as already pointed out in Chapter 4. With further propagation, after passing the vacuum focal plane the linear and tilted wave fronts are transformed into their characteristic nonlinear shape. Further along the propagation, transverse focusing of the pump pulse results in a smaller transverse extent of the plasma wave. The amplitude of the oscillation also increases, which is visible by the stronger brightness modulation in the images. After wave breaking, the plasma wave amplitude is reduced and only the first period, the bubble, remains.

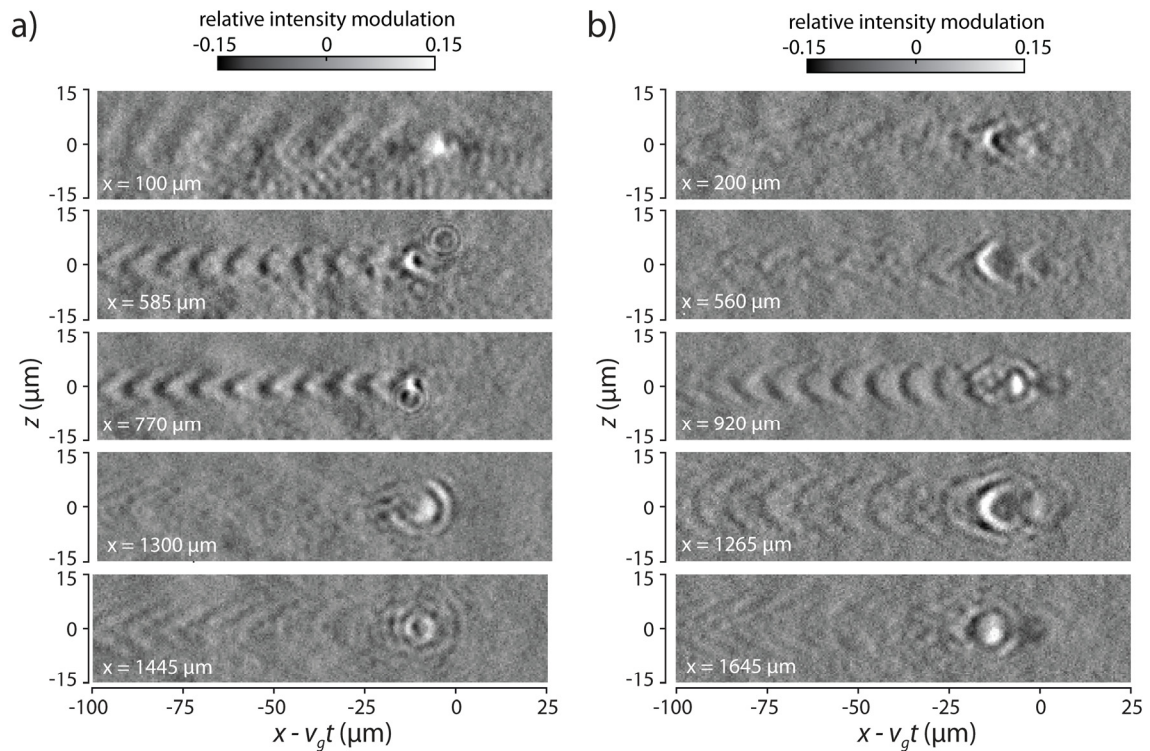


Figure 5.11 | Experimental shadowgrams for: a) helium at  $n_e = 1.65 \cdot 10^{19} \text{ cm}^{-3}$  and b) hydrogen at  $n_e = 1.5 \cdot 10^{19} \text{ cm}^{-3}$  at different positions,  $x$ , in the gas jet

The following oscillations are barely visible and the previously rounded curvature of the wave structure has morphed into a more pointed triangular shape. These waves have been seen in simulations before [107] and are identified with stimulated Raman side scattering (SRS-S). For helium, these side scattered waves are only present after the point of wave breaking if at all. This can explain the good agreement between the measurement of the plasma period at different electron densities in Section 4.3 and the frequency shift of the backscattered radiation in 5.3. The presence of these waves, which are a combination of Raman forward and backward scattering, indicate the position of backscattering, which contributed to the majority of the integrated signal in the backscatter diagnostics. The measurement of the plasma period in Chapter 4 was done around the wave breaking position and so just slightly in front of the appearance of the side scattering waves. Hence,



the backscatter diagnostics and the FCM give complementary results during this point in the evolution of the plasma wave.

For hydrogen, see Figure 5.11b, the shadowgrams look significantly different. Following the discussion in Section 4.8.1, the position of the main pulse is given by the strongest brightness modulation and is visible in the right part of the image. The small modulation in front of the main pulse seems to indicate a small part of the pump pulse was split off. At this early stage in the interaction, there is no apparent plasma wave. All oscillations are heavily dampened and exhibit a pointy shape on axis like the SRS-S waves as opposed to the curved wavefronts previously described. In the second image from the top, the upper and the lower part of the dampened wave show different angles and do not seem to cross on axis which may be related to the spatio-temporal asymmetry of the pump pulse. At  $x = 920 \mu\text{m}$ , the trailing oscillations have grown in amplitude and have developed a distinct relativistic curvature; however, the back of the very first oscillation still has a rather pointy shape with a dip in the center, which marks the point of transverse wavebreaking [71]. A large variety of shapes in the plasma oscillation can be observed with further propagation and in comparison with the helium gas the trailing plasma oscillations in hydrogen remain dampened. It is remarkable that no wave breaking radiation for hydrogen was observed at all in spite of the fact that electron bunches with sufficient charge were accelerated.

The weak modulation of the plasma wave that always precedes the high visibility modulation driven by the peak of the main pulse can be interpreted to be a result of self-modulation of the pump pulse caused by stimulated Raman forward scattering (SRS-F). The higher growth rate of SRS-F in hydrogen caused a splitting of the pump pulse with the smaller part in front of the main pulse driving a small-scale *pre*-plasma wave. To understand this behavior with hydrogen, simulations have been carried out; however, the observed effect could not yet be reproduced. Other simulations have shown that a hot plasma can prevent the formation of plasma waves due to Landau damping and reduced self-focusing of the pump pulse [125]. Combining the results from the analysis of the interferograms, backscattered radiation and the shadowgrams, strong evidence points towards the stimulated Raman instability and the generation of a hot plasma as the main difference in the interaction between helium and hydrogen.

## **5.5 Stimulated Raman scattering as efficient pre-acceleration and injection mechanism**

In this chapter, the influence of the target gas on the LWFA was discussed. Helium and hydrogen, two gases which were expected to behave similarly, show different results in LWFA experiments depending on the temporal intensity profile of the pump pulse. Using low contrast laser pulses with hydrogen can generate highly charged, well collimated and

stable electron bunches, which were used in an application based experiment. Improving the temporal intensity contrast of the laser pulses brings the results from helium and hydrogen closer together but particular differences still remain, e.g., the higher electron bunch charge obtained with hydrogen in individual shots. Differences were observed as well in the amplitude of the backscattered spectrum, in the phase shift of the probe beams and in shadowgrams taken by FCM. Due to the lower ionization threshold, hydrogen is fully ionized earlier with respect to the peak of the pump pulse than helium and so instabilities such as stimulated Raman scattering can grow faster at these higher electron densities. It was shown in Section 5.3 that this results in a higher amplitude of the backscattering signal for hydrogen. The higher growth rate for backscatter leads to pre-heating of the on-axis background plasma by the intensity pedestal of the laser pulse at intensities around  $10^{15}$  W/cm<sup>2</sup>. The result is a hot plasma with temperatures in the 100s of keV, which suppresses the generation of a long lasting plasma oscillation [125]. For low contrast pump pulses the spatial extent of this hot plasma was large enough to be observed by interferometry while for high contrast pulses it could not be observed due to the lack of spatial resolution. However, using FCM allowed the influence of the hot plasma on the formation of the plasma wave to be observed for the first time. As the pump pulse propagates further into the hydrogen plasma the pulse front steepens and at the same time the lower intensity pulse pedestal is diffracted, hence, the growth rate for SRS-B is reduced. Therefore the relativistic effects of the pump pulse become dominant and drive a plasma wave similar to the helium interaction. However, the combination of SRS-B and SRS-F has efficiently generated a high number of seed electrons with sufficient forward momentum that can be longitudinally injected into the plasma wave driven by the peak of the pump pulse as they were passed by. This leads to well collimated electron bunches with more charge than in the LWFA experiments using helium.

Reproducing these complex and manifold effects in a simulation requires huge computational power because the transverse beam profile as well as the temporal intensity profile of the pump pulse are required, and the ionization dynamics have to be included in a 3-D simulation. This was beyond the scope of this thesis. Nevertheless, FCM in combination with the backscattered spectra and the refractive index profiles from interferograms have already revealed the important mechanism behind the interaction.

## 6. Conclusion and future applications

In this thesis, laser driven wakefield acceleration of electrons in the self-injection regime was investigated. A newly developed few-cycle probe beam at the JETi40 laser system was used and shadowgrams of the laser-plasma interaction were recorded with a high-resolution microscope (Few-Cycle Microscopy, FCM). The pulse duration of the probe beam, of 5.5 fs was significantly shorter than the driving laser pulse, which allowed a pristine insight into this acceleration regime. Using 3-D PIC simulations, which included the propagation of the probe beam as well as the imaging system, the recorded features could be reproduced exactly and the detailed formation of the shadowgram could be described for the first time. This allowed the extraction of quantitative information such as the plasma wavelength and especially the length of the first oscillation period, i.e., the bubble, with high accuracy for the first time. By scanning the backing pressure of the gas valve and thereby changing the background density of the gas jet a deviation from the square root dependence of the plasma wavelength on the electron density was observed. This unexpected behavior has never been reported [21, 25] before. The threshold electron density at which this deviation occurs first depends only on the effective laser power in units of the critical power for self-focusing as it was derived by Mangles *et al.* [86], which is in very good agreement with the here reported value. At the threshold for self-injection the evolution of the plasma wave along its propagation was recorded. Here, the change of the bubble size was of particular interest. The expansion of the bubble prior to the injection of electrons into the plasma wakefield was observed. The origin of this expansion was linked to the amplification of the pump pulse, which drives the plasma wave. Before injection occurs, the intensity of the pump pulse has increased by almost one order of magnitude as compared to the vacuum intensity of the laser pulse. The observed intensity threshold for trapping is in very good agreement with the prediction by Mangles [79]. After the laser pulse depletes, the bubble should contract again but instead remains unchanged and even expands further due to beamloading of the injected electrons. Measuring the dephasing length at the point of injection directly from the bubble length resolved the discrepancy between the theoretical prediction of the maximum energy of the accelerated electrons and the experimentally observed values. Here, the key is that the model requires laser pulses matched to a certain electron background density resulting in the generation of a stationary bubble. In the case of unmatched conditions, FCM allows direct access to the evolving plasma quantities and is, hence, an important tool to benchmark PIC simulations.

In a second experiment described in this thesis light was shed on the differences between helium and hydrogen as the target gas in a laser wakefield accelerator. The temporal intensity contrast of the rising edge of the driver pulse was identified as an important parameter in this situation. Due to the lower ionization threshold of hydrogen, a low temporal contrast leads to an earlier complete ionization up to 1 ps before the laser pulse's peak. The high electron density and laser intensity levels of  $10^{15}$  W/cm<sup>2</sup> give rise to the stimulated Raman instability where the incident light wave decays into forward or backward scattered electromagnetic waves and an electrostatic wave. The low phase velocity of these waves generated by Raman backscattering can efficiently trap background electrons and accelerate them to energies of several 100 keV in the forward direction. The resulting hot plasma was observed in interferograms for low contrast conditions of the pump pulses as compared to the case of higher laser contrast. There, the hot plasma may still be present but could not be observed due to the limited spatial resolution in the interferograms. The hot plasma further suppresses the formation of the plasma wave at the beginning of the interaction. Due to a steepening of the pump pulse's edge during its propagation, the growth of the Raman backscattering instability was heavily reduced and a plasma wave similar to the interaction with helium gas was formed. The hot background electrons with momentum in the forward direction were overtaken by the plasma wave driven by the main pulse due to its higher velocity which lead to longitudinal injection of pre-accelerated electrons into the main plasma wave. Consequently, the charge of the accelerated electron bunch is increased, the collimation is improved and the pointing fluctuations are reduced. This enabled an applied experiment where the dose response of cancer cells from their irradiation with laser generated accelerated electron bunches could be investigated for the first time [36].

To overcome the inherent shot-to-shot fluctuations in the laser-plasma-interaction it would be beneficial to record the complete process by FCM in a single shot. This would allow the study of instabilities like filamentation, hosing or the formation of relativistic solitons. A possible approach will be discussed in the next section and the scalability of FCM to lower plasma densities, which are required for future high-energy accelerators, will be shown.

## **6.1 Complete temporal evolution of the plasma wave in a single shot**

A very broad spectrum is required to generate ultrashort laser pulses as it was shown in Section 3.5.2. However, the temporal resolution of the probing itself solely depends on the transform limited pulse duration, as long as only a linear chirp is present. This was demonstrated in [126] for fs-pump-probe spectroscopy. In the presence of a linear chirp, i.e., a longer pulse duration at the interaction point, spectral filtering in the detector plane

preserves the temporal resolution. The smaller the spectral window, the higher the temporal resolution, up to the transform limit. This can be understood by representing the short pulse in a Wigner spectrogram (WS), i.e., a two-dimensional representation of the time and frequency profile of a laser pulse. Calculating the integral over frequency gives the temporal intensity profile of the laser pulse while the integral over time gives the energy spectral density. Hence, one can conclude, that the longer pulse duration caused by a strong frequency chirp (with purely quadratic phase), is represented by temporal shearing of the WS of the corresponding transform limited pulses, as the various frequency components of the pulse arrive at different times. While the temporal intensity profile of the chirped pulse is dramatically broadened, any horizontal cut of the WS at a given frequency preserves the duration of the transform limited pulse. The effect of spectral filtering of the probe pulse before and after the laser-plasma interaction and its influences on the temporal resolution of the shadowgram was investigated. For this purpose, a two channel shadowgraphy setup was used. The probe beam was split by means of a non-polarizing beam splitter cube and the laser-plasma interaction was imaged onto two separate cameras. One camera was equipped with a narrow band interference filter with a central wavelength of 700 nm ( $\Delta\lambda = 10$  nm) or 800 nm ( $\Delta\lambda = 40$  nm) while for the other camera only a ND filter was used. The results are shown in Figure 6.1. The plasma wave is visible whether an interference filter or a ND filter was placed in front of the CCD. Changing the central wavelength of the filter does not change the outcome. However, the contrast of the plasma wave is defined by the transmittance of the filter and the spectral intensity of the probe beam in that spectral window resulting in a lower signal to noise ratio.

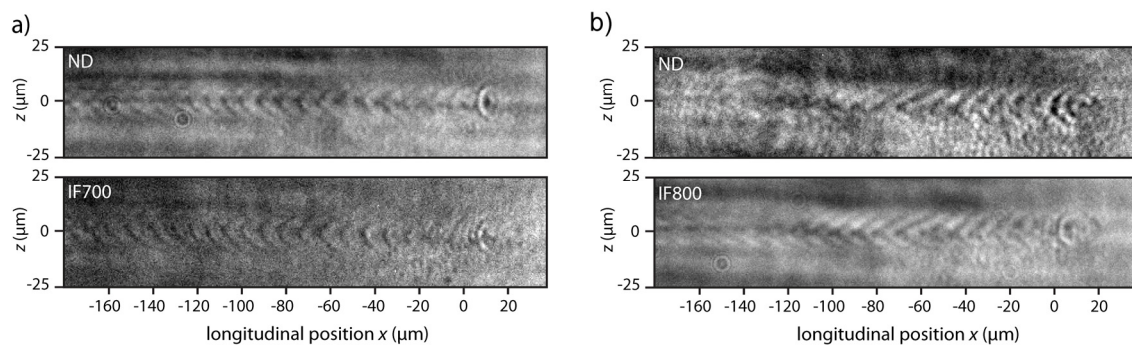


Figure 6.1 | Spectral filtering and temporal resolution. a) Filtering post-interaction with an ND filter (top) and 700(10) nm IF below b) Filtering post-interaction with an ND filter (top) and 800(40) nm IF below.

Despite that, the images with the 10 nm bandwidth interference filters show the best visibility of the plasma wave, which is an experimental verification of the effects discussed above. The temporal resolution only depends on the transform limited pulse duration, as long as only a linear chirp is applied. So even if the pulses are stretched, e.g., by glass components or just air, the temporal resolution can be maintained if the image is recorded in a narrow spectral window.

Generating probe pulses with higher energy and a more evenly distributed spectral intensity, e.g., by using differentially pumped hollow core fibers, opens the path for future applications with chirped pulses. Different time steps in the evolution are imprinted in different colors of the probe pulse. To record the evolution in a single shot a “3-D” camera is required, which would record the probe pulse’s spectrum in every pixel similar to *Sequentially Timed All-optical Mapping Photography* described in [127]. However, the requirement can be relaxed if only distinct time steps during the interaction are considered. As it was shown in Section 4.4, dividing the evolution into ten steps seems sufficient to get a detailed overview about the evolution within 2 mm of propagation. The probe pulse has to be stretched linearly by a factor of  $\approx 2000$  to a duration of at least 6.7 ps. For a laser pulse with a bandwidth of 500 nm this can be achieved by inserting a 30 mm block of fused silica into the beam. To recover the temporal resolution in the detector plane a filter with a bandwidth of  $\Delta\lambda = 500 \text{ nm}/2000 = 0.25 \text{ nm}$  would be necessary. These filters can be implemented as an array in front of the detector with decreasing wavelength from left to right if the pump pulse propagates in the same manner. Now the complete interaction could be recorded in a single image.

## 6.2 Extension of ultrafast shadowgraphy to longer wavelengths

The next generation of plasma wake field accelerators driven either by lasers or particle beams will use electron densities in the range of  $n_e \approx 10^{17} \text{ cm}^{-3}$  to reach energies in excess of 10 GeV. At these low densities, probing at optical wavelengths lowers the contrast in the shadowgrams since the ratio  $\frac{\omega_p}{\sqrt{V}\omega_{pr}}$  is the essential quantity, which is connected to the refractive index of the plasma (Eq. 2.20). This issue was investigated with the help of a simulation including the imaging setup, similar to the simulation described in Section 4.8. The result is shown in Figure 6.2. Here the laser pulse and plasma parameters were scaled to yield a similar plasma wave although scaled by a factor of two in all dimensions, see Figure 6.2b. Hence, the electron density was reduced to  $n_0/4$  resulting in reducing the plasma frequency by a factor of two. Using the same probe pulse at a center wavelength of  $\lambda_{pr} = 750 \text{ nm}$  reduces the visibility of the plasma wave in the shadowgram dramatically. However, the visibility is recovered when probe pulses at  $\lambda_{pr} = 1.4 \mu\text{m}$  but still with a duration of a few cycles are used. Using even lower electron background densities would require few-cycle probe pulse in the mid infrared. These pulses can be generated by shifting the wavelength of the probe beam using an optical parametric amplifier and generating the difference frequency. Such few-cycle pulses in the mid-IR have been already generated [128]. Furthermore, beam driven wake field accelerators could use a standalone OPCPA laser system operating in the mid-IR, which has the advantage of a

much higher repetition rate [129] thus enabling it to be synchronized to the particle accelerator. FCM would be the ideal tool to monitor the spatial and temporal overlap between different acceleration stages, starting with the initial injection of electrons in the first stage and later coupling between tens of post acceleration modules [12] for a proposed TeV electron-positron collider. While the position of the plasma wave can be observed with shadowgraphy, the electron bunch can be located via its surrounding azimuthal magnetic field, which rotates the probe beam's polarization due to the Faraday effect [21, 130]. The remaining challenge would be the implementation of advanced imaging techniques to overcome the scattering of the probe beam at the rough walls of the capillary used as the acceleration modules.

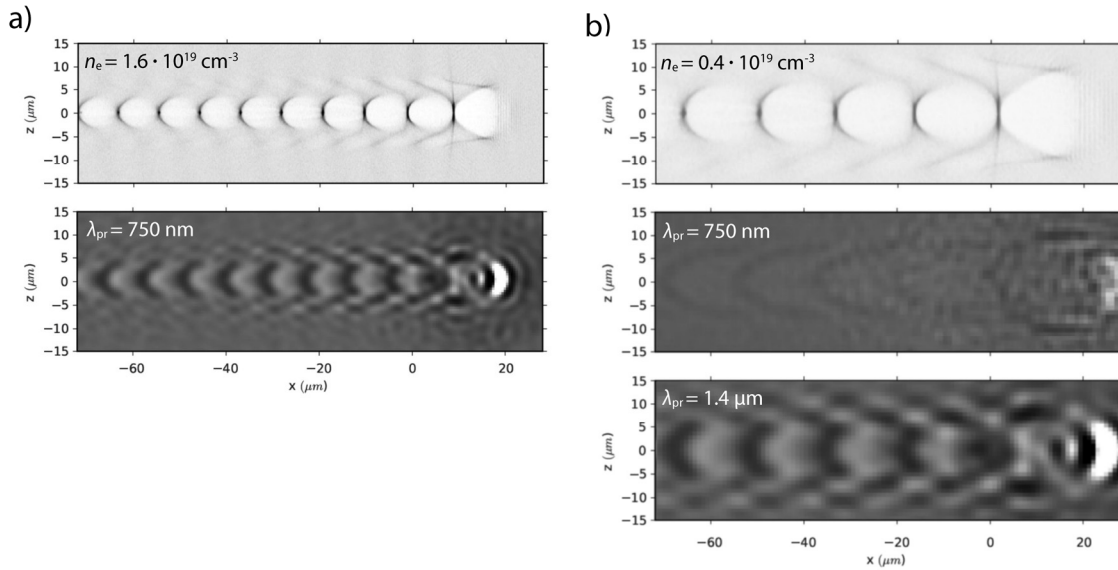


Figure 6.2 | Simulated shadowgrams at different electron densities and probing wavelengths. a) Electron density distribution at  $n_e = 1.6 \cdot 10^{19} \text{ cm}^{-3}$  (top) and simulated shadowgram with  $\lambda_{pr} = 750 \text{ nm}$  (bottom). b) Electron density distribution at  $n_e = 0.4 \cdot 10^{19} \text{ cm}^{-3}$  (top) and simulated shadowgram with  $\lambda_{pr} = 750 \text{ nm}$  (center) and with  $\lambda_{pr} = 1.4 \text{ μm}$  (bottom). (image courtesy by E. Siminos).

A possible solution was already demonstrated by C. Ma *et al.* [131] by using the *Time-Reversed Adapted Perturbation* (TRAP) technique involving a spatial light modulator to compensate the random phase imprinted on the wavefront of the probe beam by the capillary walls. Ultimately, the recording of the complex light field of the plasma wave via holographic techniques [132] would allow a 3-D reconstruction, which can also yield valuable information about the spatio-temporal shape of the pump pulse at these relativistic intensities. In all these scenarios, FCM would be an invaluable tool to gain detailed insight into the different acceleration regimes, which would bring future radiation and particle sources based on plasma acceleration closer to reality.

# Bibliography

1. Nobel Prizes and Laureates, (2016 March 20). Retrieved from [www.nobelprize.org/nobel\\_prizes/](http://www.nobelprize.org/nobel_prizes/)
2. Conseil European pour le Recherche Nuclaire, Retrieved from home.cern
3. The Stanford Linear Accelerator Center, (2016 March 20). Retrieved from slac.stanford.edu
4. S. Chatrchyan, et al., Observation of a new boson at a mass of 125 GeV with the CMS experiment at the LHC. *Physics Letters B* **716**, 30-61 (2012).
5. G. Aad, et al., Observation of a new particle in the search for the Standard Model Higgs boson with the ATLAS detector at the LHC. *Physics Letters B* **716**, 1-29 (2012).
6. The Linear Collider Collaboration, (2016 March 20). Retrieved from [www.linearcollider.org](http://www.linearcollider.org)
7. E. A. Peralta, K. Soong, R. J. England, E. R. Colby, Z. Wu, B. Montazeri, C. McGuinness, J. McNeur, K. J. Leedle, D. Walz, E. B. Sozer, B. Cowan, B. Schwartz, G. Travish and R. L. Byer, Demonstration of electron acceleration in a laser-driven dielectric microstructure. *Nature* **503**, 91-94 (2013).
8. J. M. Dawson, Nonlinear Electron Oscillations in a Cold Plasma. *Physical Review* **113**, 383-387 (1959).
9. J. B. Rosenzweig, D. B. Cline, B. Cole, H. Figueroa, W. Gai, R. Konecny, J. Norem, P. Schoessow and J. Simpson, Experimental Observation of Plasma Wake-Field Acceleration. *Phys. Rev. Lett.* **61**, 98-101 (1988).
10. M. Litos, E. Adli, W. An, C. I. Clarke, C. E. Clayton, S. Corde, J. P. Delahaye, R. J. England, A. S. Fisher, J. Frederico, S. Gessner, S. Z. Green, M. J. Hogan, C. Joshi, W. Lu, K. A. Marsh, W. B. Mori, P. Muggli, N. Vafaei-Najafabadi, D. Walz, G. White, Z. Wu, V. Yakimenko and G. Yocky, High-efficiency acceleration of an electron beam in a plasma wakefield accelerator. *Nature* **515**, 92-+ (2014).
11. S. Corde, E. Adli, J. M. Allen, W. An, C. I. Clarke, C. E. Clayton, J. P. Delahaye, J. Frederico, S. Gessner, S. Z. Green, M. J. Hogan, C. Joshi, N. Lipkowitz, M. Litos, W. Lu, K. A. Marsh, W. B. Mori, M. Schmeltz, N. Vafaei-Najafabadi, D. Walz, V. Yakimenko and G. Yocky, Multi-gigaelectronvolt acceleration of positrons in a self-loaded plasma wakefield. *Nature* **524**, 442-445 (2015).



12. W. Leemans and E. Esarey, Laser-driven plasma-wave electron accelerators. *Physics Today* **62**, 44-49 (2009).
13. E. Gschwendtner, T. Bohl, C. Bracco, A. C. Butterworth, S. Cipiccia, S. Döbert, V. Fedosseev, E. Feldbaumer, C. Heßler, W. Höfle, M. Martyanov, M. Meddahi, J. A. Osborne, A. Pardons, A. V. Petrenko and H. Vincke, The AWAKE Experimental Facility at CERN. *Proceedings of IPAC2014*, 582 (2014).
14. A. Caldwell, K. Lotov, A. Pukhov and F. Simon, Proton-driven plasma-wakefield acceleration. *Nature Phys.* **5**, 363-367 (2009).
15. D. Strickland and G. Mourou, Compression of Amplified Chirped Optical Pulses. *Opt. Commun.* **56**, 219-221 (1985).
16. S. P. D. Mangles, C. D. Murphy, Z. Najmudin, A. G. R. Thomas, J. L. Collier, A. E. Dangor, E. J. Divall, P. S. Foster, J. G. Gallacher, C. J. Hooker, D. A. Jaroszynski, A. J. Langley, W. B. Mori, P. A. Norreys, F. S. Tsung, R. Viskup, B. R. Walton and K. Krushelnick, Monoenergetic beams of relativistic electrons from intense laser-plasma interactions. *Nature* **431**, 535-538 (2004).
17. J. Faure, Y. Glinec, A. Pukhov, S. Kiselev, S. Gordienko, E. Lefebvre, J. P. Rousseau, F. Burgy and V. Malka, A laser-plasma accelerator producing monoenergetic electron beams. *Nature* **431**, 541-544 (2004).
18. C. G. R. Geddes, C. Toth, J. van Tilborg, E. Esarey, C. B. Schroeder, D. Bruhwiler, C. Nieter, J. Cary and W. P. Leemans, High-quality electron beams from a laser wakefield accelerator using plasma-channel guiding. *Nature* **431**, 538-541 (2004).
19. W. P. Leemans, A. J. Gonsalves, H. S. Mao, K. Nakamura, C. Benedetti, C. B. Schroeder, C. Tóth, J. Daniels, D. E. Mittelberger, S. S. Bulanov, J. L. Vay, C. G. R. Geddes and E. Esarey, Multi-GeV Electron Beams from Capillary-Discharge-Guided Subpetawatt Laser Pulses in the Self-Trapping Regime. *Phys. Rev. Lett.* **113**, 245002 (2014).
20. O. Lundh, J. Lim, C. Rechatin, L. Ammoura, A. Ben-Ismaïl, X. Davoine, G. Gallot, J. P. Goddet, E. Lefebvre, V. Malka and J. Faure, Few femtosecond, few kiloampere electron bunch produced by a laser-plasma accelerator. *Nature Phys.* **7**, 219-222 (2011).
21. A. Buck, M. Nicolai, K. Schmid, C. M. S. Sears, A. Sävert, J. M. Mikhailova, F. Krausz, M. C. Kaluza and L. Veisz, Real-time observation of laser-driven electron acceleration. *Nature Phys.* **7**, 543-548 (2011).
22. Y. Ding, A. Brachmann, F. J. Decker, D. Dowell, P. Emma, J. Frisch, S. Gilevich, G. Hays, P. Hering, Z. Huang, R. Iverson, H. Loos, A. Miahnahri, H. D. Nuhn, D. Ratner, J. Turner, J. Welch, W. White and J. Wu, Measurements and Simulations of Ultralow Emittance

and Ultrashort Electron Beams in the Linac Coherent Light Source. *Phys. Rev. Lett.* **102**, 254801 (2009).

23. S. Kneip, C. McGuffey, J. L. Martins, S. F. Martins, C. Bellei, V. Chvykov, F. Dollar, R. Fonseca, C. Huntington, G. Kalintchenko, A. Maksimchuk, S. P. D. Mangles, T. Matsuoka, S. R. Nagel, C. A. J. Palmer, J. Schreiber, K. T. Phuoc, A. G. R. Thomas, V. Yanovsky, L. O. Silva, K. Krushelnick and Z. Najmudin, Bright spatially coherent synchrotron X-rays from a table-top source. *Nature Phys.* **6**, 980-983 (2010).
24. C. W. Siders, S. P. LeBlanc, D. Fisher, T. Tajima, M. C. Downer, A. Babine, A. Stepanov and A. Sergeev, Laser wakefield excitation and measurement by femtosecond longitudinal interferometry. *Phys. Rev. Lett.* **76**, 3570 (1996).
25. N. H. Matlis, S. Reed, S. S. Bulanov, V. Chvykov, G. Kalintchenko, T. Matsuoka, P. Rousseau, V. Yanovsky, A. Maksimchuk, S. Kalmykov, G. Shvets and M. C. Downer, Snapshots of laser wakefields. *Nature Phys.* **2**, 749-753 (2006).
26. P. Dong, S. A. Reed, S. A. Yi, S. Kalmykov, G. Shvets, M. C. Downer, N. H. Matlis, W. P. Leemans, C. McGuffey, S. S. Bulanov, V. Chvykov, G. Kalintchenko, K. Krushelnick, A. Maksimchuk, T. Matsuoka, A. G. R. Thomas and V. Yanovsky, Formation of optical bullets in laser-driven plasma bubble accelerators. *Phys. Rev. Lett.* **104**, 134801 (2010).
27. P. Dong, S. A. Reed, S. A. Yi, S. Kalmykov, Z. Y. Li, G. Shvets, N. H. Matlis, C. McGuffey, S. S. Bulanov, V. Chvykov, G. Kalintchenko, K. Krushelnick, A. Maksimchuk, T. Matsuoka, A. G. R. Thomas, V. Yanovsky and M. C. Downer, Holographic visualization of laser wakefields. *New Journal of Physics* **12**, (2010).
28. Z. Li, H.-E. Tsai, X. Zhang, C.-H. Pai, Y.-Y. Chang, R. Zgadzaj, X. Wang, V. Khudik, G. Shvets and M. C. Downer, Single-Shot Visualization of Evolving Laser Wakefields Using an All-Optical Streak Camera. *Phys. Rev. Lett.* **113**, 085001 (2014).
29. W. Lu, M. Tzoufras, C. Joshi, F. S. Tsung, W. B. Mori, J. Vieira, R. A. Fonseca and L. O. Silva, Generating multi-GeV electron bunches using single stage laser wakefield acceleration in a 3D nonlinear regime. *Phys. Rev. ST Accel. Beams* **10**, 061301 (2007).
30. M. Nisoli, S. DeSilvestri and O. Svelto, Generation of high energy 10 fs pulses by a new pulse compression technique. *Applied Physics Letters* **68**, 2793-2795 (1996).
31. G. G. Paulus, F. Grasbon, H. Walther, P. Villoriesi, M. Nisoli, S. Stagira, E. Priori and S. De Silvestri, Absolute-phase phenomena in photoionization with few-cycle laser pulses. *Nature* **414**, 182-184 (2001).
32. M. Nicolai, A. Sävert, M. Reuter, M. Schnell, J. Polz, O. Jäckel, L. Karsch, M. Schürer, M. Oppelt, J. Pawelke and M. Kaluza, Realizing a laser-driven electron source applicable for radiobiological tumor irradiation. *Applied Physics B* **116**, 1-9 (2013).

33. M. Schnell, A. Sävert, I. Uschmann, M. Reuter, M. Nicolai, T. Kaempfer, B. Landgraf, O. Jaeckel, O. Jansen, A. Pukhov, M. C. Kaluza and C. Spielmann, Optical control of hard X-ray polarization by electron injection in a laser wakefield accelerator. *Nature Commun.* **4**, 2421 (2013).
34. M. B. Schwab, *Tailorable Femtosecond Probe-Beam for Observation of Laser Driven Acceleration Mechanisms*. Master thesis, Friedrich-Schiller-Universität Jena, 2011.
35. A. Sävert, S. P. D. Mangles, M. Schnell, E. Siminos, J. M. Cole, M. Leier, M. Reuter, M. B. Schwab, M. Möller, K. Poder, O. Jäckel, G. G. Paulus, C. Spielmann, S. Skupin, Z. Najmudin and M. C. Kaluza, Direct Observation of the Injection Dynamics of a Laser Wakefield Accelerator Using Few-Femtosecond Shadowgraphy. *Phys. Rev. Lett.* **115**, 055002 (2015).
36. M. Oppelt, M. Baumann, R. Bergmann, E. Beyreuther, K. Brüchner, J. Hartmann, L. Karsch, M. Krause, L. Laschinsky, E. Leßmann, M. Nicolai, M. Reuter, C. Richter, A. Sävert, M. Schnell, M. Schürer, J. Woithe, M. Kaluza and J. Pawelke, Comparison study of in vivo dose response to laser-driven versus conventional electron beam. *Radiation and Environmental Biophysics*, 1-12 (2015).
37. M. V. Ammosov, N. B. Delone and V. P. Krainov, Tunnel Ionization of Complex Atoms and Atomic Ions in a Varying Electromagnetic-Field. *Zhurnal Eksperimentalnoi I Teoreticheskoi Fiziki* **91**, 2008-2013 (1986).
38. L. V. Keldysh, Ionization in the field of a strong electromagnetic wave. *Soviet Physics JETP* **20**, 1307 (1965).
39. J. Liu, E. J. Salumbides, U. Hollenstein, J. C. J. Koelemeij, K. S. E. Eikema, W. Ubachs and F. Merkt, Determination of the ionization and dissociation energies of the hydrogen molecule. *The Journal of Chemical Physics* **130**, 174306 (2009).
40. J. D. Lawson, Lasers and Accelerators. *IEEE Transactions on Nuclear Science* **26**, 4217-4219 (1979).
41. E. Esarey, P. Sprangle and J. Krall, Laser Acceleration of Electrons in Vacuum. *Physical Review E* **52**, 5443-5453 (1995).
42. B. Quesnel and P. Mora, Theory and simulation of the interaction of ultraintense laser pulses with electrons in vacuum. *Physical Review E* **58**, 3719-3732 (1998).
43. T. Esirkepov, M. Borghesi, S. V. Bulanov, G. Mourou and T. Tajima, Highly Efficient Relativistic-Ion Generation in the Laser-Piston Regime. *Phys. Rev. Lett.* **92**, 175003 (2004).

44. W. B. Mori, The physics of the nonlinear optics of plasmas at relativistic intensities for short-pulse lasers. *IEEE Journal of Quantum Electronics* **33**, 1942-1953 (1997).
45. E. Esarey, C. B. Schroeder and W. P. Leemans, Physics of laser-driven plasma-based electron accelerators. *Reviews of Modern Physics* **81**, 1229-1285 (2009).
46. G. Z. Sun, E. Ott, Y. C. Lee and P. Guzdar, Self-focusing of short intense pulses in plasmas. *Phys. Fluids* **30**, 526-532 (1987).
47. P. Sprangle, E. Esarey and A. Ting, Nonlinear theory of intense laser-plasma interactions. *Phys. Rev. Lett.* **64**, 2011-2014 (1990).
48. C. D. Decker, W. B. Mori, K. C. Tzeng and T. Katsouleas, The evolution of ultra-intense, short-pulse lasers in underdense plasmas. *Phys. Plasmas* **3**, 2047-2056 (1996).
49. V. Kumarappan, K. Y. Kim and H. M. Milchberg, Guiding of Intense Laser Pulses in Plasma Waveguides Produced from Efficient, Femtosecond End-Pumped Heating of Clustered Gases. *Phys. Rev. Lett.* **94**, 205004 (2005).
50. W. P. Leemans, B. Nagler, A. J. Gonsalves, C. Toth, K. Nakamura, C. G. R. Geddes, E. Esarey, C. B. Schroeder and S. M. Hooker, GeV electron beams from a centimetre-scale accelerator. *Nature Phys.* **2**, 696-699 (2006).
51. J. Faure, Y. Glinec, J. J. Santos, F. Ewald, J. P. Rousseau, S. Kiselev, A. Pukhov, T. Hosokai and V. Malka, Observation of laser-pulse shortening in nonlinear plasma waves. *Phys. Rev. Lett.* **95**, 205003 (2005).
52. J. Schreiber, C. Bellei, S. P. D. Mangles, C. Kamperidis, S. Kneip, S. R. Nagel, C. A. J. Palmer, P. P. Rajeev, M. J. V. Streeter and Z. Najmudin, Complete temporal characterization of asymmetric pulse compression in a laser wakefield. *Phys. Rev. Lett.* **105**, 235003 (2010).
53. S. Y. Kalmykov, A. Beck, X. Davoine, E. Lefebvre and B. A. Shadwick, Laser plasma acceleration with a negatively chirped pulse: all-optical control over dark current in the blowout regime. *New Journal of Physics* **14**, 033025 (2012).
54. W. L. Kruer, *The Physics of Laser Plasma Interactions*. Addison- Wesley, Redwood City, 1988.
55. C. Rousseaux, G. Malka, J. L. Miquel, F. Amiranoff, S. D. Baron and P. Mounaix, Experimental validation of the linear theory of stimulated Raman-scattering driven by a 500-fs laser pulse in a preformed underdense plasma. *Phys. Rev. Lett.* **74**, 4655-4658 (1995).

56. P. Bertrand, A. Ghizzo, S. J. Karttunen, T. J. H. Pattikangas, R. R. E. Salomaa and M. Shoucri, 2-Stage electron acceleration by simultaneous stimulated Raman backward and forward scattering. *Phys. Plasmas* **2**, 3115-3129 (1995).
57. T. M. Antonsen and P. Mora, Self-focusing and Raman scattering of laser pulses in tenuous plasmas. *Physics of Fluids B* **5**, 1440-1452 (1993).
58. A. Modena, Z. Najmudin, A. E. Dangor, C. E. Clayton, K. A. Marsh, C. Joshi, V. Malka, C. B. Darrow, C. Danson, D. Neely and F. N. Walsh, Electron acceleration from the breaking of relativistic plasma waves. *Nature* **377**, 606-608 (1995).
59. C. E. Max, J. Arons and A. B. Langdon, Self-Modulation and Self-Focusing of Electromagnetic-Waves in Plasmas. *Phys. Rev. Lett.* **33**, 209-212 (1974).
60. W. B. Mori, C. D. Decker, D. E. Hinkel and T. Katsouleas, Raman Forward Scattering of Short-Pulse High-Intensity Lasers. *Phys. Rev. Lett.* **72**, 1482-1485 (1994).
61. E. Esarey, P. Sprangle, J. Krall and A. Ting, Overview of plasma-based accelerator concepts. *IEEE Transactions on Plasma Science* **24**, 252-288 (1996).
62. P. Gibbon, *Short Pulse Laser Interactions with Matter: An Introduction*. Imperial College Press, 2005.
63. V. I. Berezhiani and I. G. Murusidze, Relativistic wake-field generation by an intense laser-pulse in a plasma. *Physics Letters A* **148**, 338-340 (1990).
64. L. M. Gorbunov and V. I. Kirsanov, Excitation of plasma-wave by short electromagnetic-wave packets. *Zhurnal Eksperimentalnoi I Teoreticheskoi Fiziki* **93**, 509-518 (1987).
65. T. Tajima and J. M. Dawson, Laser Electron-Accelerator. *Phys. Rev. Lett.* **43**, 267-270 (1979).
66. C. D. Decker and W. B. Mori, Group-Velocity of Large-Amplitude Electromagnetic-Waves in a Plasma. *Phys. Rev. Lett.* **72**, 490-493 (1994).
67. A. I. Akhiezer and R. V. Polovin, Theory of Wave Motion of an Electron Plasma. *Soviet Physics JETP-USSR* **3**, 696-705 (1956).
68. J. B. Rosenzweig, Trapping, thermal effects, and wave breaking in the nonlinear plasma wake-field accelerator. *Phys. Rev. A* **38**, 3634-3642 (1988).
69. Z. M. Sheng and J. Meyer-ter-Vehn, Relativistic wave breaking in warm plasmas. *Phys. Plasmas* **4**, 493-495 (1997).

70. S. C. Rae and K. Burnett, Possible Production of Cold-Plasmas through Optical-Field-Induced Ionization. *Phys. Rev. A* **46**, 2077-2083 (1992).
71. S. V. Bulanov, F. Pegoraro, A. M. Pukhov and A. S. Sakharov, Transverse-wake wave breaking. *Phys. Rev. Lett.* **78**, 4205 (1997).
72. J. Faure, J. R. Marques, V. Malka, F. Amiranoff, Z. Najmudin, B. Walton, J. P. Rousseau, S. Ranc, A. Solodov and P. Mora, Dynamics of Raman instabilities using chirped laser pulses. *Physical Review E* **63**, 065401 (2001).
73. B. Hidding, K. U. Amthor, B. Liesfeld, H. Schwöerer, S. Karsch, M. Geissler, L. Veisz, K. Schmid, J. G. Gallacher, S. P. Jamison, D. Jaroszynski, G. Pretzler and R. Sauerbrey, Generation of quasimonoenergetic electron bunches with 80-fs laser pulses. *Phys. Rev. Lett.* **96**, (2006).
74. A. Pukhov and J. Meyer-ter-Vehn, Laser wake field acceleration: the highly non-linear broken-wave regime. *Appl. Phys. B* **74**, 355-361 (2002).
75. A. Butler, D. J. Spence and S. M. Hooker, Guiding of High-Intensity Laser Pulses with a Hydrogen-Filled Capillary Discharge Waveguide. *Phys. Rev. Lett.* **89**, 185003 (2002).
76. M. Tzoufras, W. Lu, F. S. Tsung, C. Huang, W. B. Mori, T. Katsouleas, J. Vieira, R. A. Fonseca and L. O. Silva, Beam Loading in the Nonlinear Regime of Plasma-Based Acceleration. *Phys. Rev. Lett.* **101**, 145002 (2008).
77. C. Rechatin, X. Davoine, A. Lifschitz, A. Ben Ismail, J. Lim, E. Lefebvre, J. Faure and V. Malka, Observation of Beam Loading in a Laser-Plasma Accelerator. *Phys. Rev. Lett.* **103**, 194804 (2009).
78. S. Gordienko and A. Pukhov, Scalings for ultrarelativistic laser plasmas and quasimonoenergetic electrons. *Physics of Plasmas (1994-present)* **12**, 043109 (2005).
79. S. P. D. Mangles, An Overview of Recent Progress in LaserWakefield Acceleration Experiments. *Proceedings of the CAS-CERN Accelerator School: Plasma Wake Acceleration* **1**, (2016).
80. J. Faure, C. Rechatin, A. Norlin, A. Lifschitz, Y. Glinec and V. Malka, Controlled injection and acceleration of electrons in plasma wakefields by colliding laser pulses. *Nature* **444**, 737-739 (2006).
81. A. Buck, J. Wenz, J. Xu, K. Khrennikov, K. Schmid, M. Heigoldt, J. M. Mikhailova, M. Geissler, B. Shen, F. Krausz, S. Karsch and L. Veisz, Shock-Front Injector for High-Quality Laser-Plasma Acceleration. *Phys. Rev. Lett.* **110**, 185006 (2013).

82. K. Floettmann, Generation of sub-fs electron beams at few-MeV energies. *Nuclear Instruments & Methods in Physics Research Section a-Accelerators Spectrometers Detectors and Associated Equipment* **740**, 34-38 (2014).
83. V. Malka, S. Fritzler, E. Lefebvre, M. M. Aleonard, F. Burgy, J. P. Chambaret, J. F. Chemin, K. Krushelnick, G. Malka, S. P. D. Mangles, Z. Najmudin, M. Pittman, J. P. Rousseau, J. N. Scheurer, B. Walton and A. E. Dangor, Electron acceleration by a wake field forced by an intense ultrashort laser pulse. *Science* **298**, 1596-1600 (2002).
84. I. Kostyukov, E. Nerush, A. Pukhov and V. Seredov, Electron Self-Injection in Multidimensional Relativistic-Plasma Wake Fields. *Phys. Rev. Lett.* **103**, 175003 (2009).
85. A. G. R. Thomas, Scalings for radiation from plasma bubbles. *Phys. Plasmas* **17**, 056708 (2010).
86. S. P. D. Mangles, G. Genoud, M. S. Bloom, M. Burza, Z. Najmudin, A. Persson, K. Svensson, A. G. R. Thomas and C. G. Wahlstrom, Self-injection threshold in self-guided laser wakefield accelerators. *Phys. Rev. ST Accel. Beams* **15**, 011302 (2012).
87. S. Kalmykov, S. A. Yi, V. Khudik and G. Shvets, Electron self-injection and trapping into an evolving plasma bubble. *Phys. Rev. Lett.* **103**, 135004 (2009).
88. R. Lehe, A. F. Lifschitz, X. Davoine, C. Thaury and V. Malka, Optical Transverse Injection in Laser-Plasma Acceleration. *Phys. Rev. Lett.* **111**, 085005 (2013).
89. M. Schnell, A. Sävert, B. Landgraf, M. Reuter, M. Nicolai, O. Jackel, C. Peth, T. Thiele, O. Jansen, A. Pukhov, O. Willi, M. C. Kaluza and C. Spielmann, Deducing the electron-beam diameter in a laser-plasma accelerator using x-ray betatron radiation. *Phys. Rev. Lett.* **108**, 075001 (2012).
90. S. P. D. Mangles, A. G. R. Thomas, M. C. Kaluza, O. Lundh, F. Lindau, A. Persson, Z. Najmudin, C. G. Wahlstrom, C. D. Murphy, C. Kamperidis, K. L. Lancaster, E. Divall and K. Krushelnick, Effect of laser contrast ratio on electron beam stability in laser wakefield acceleration experiments. *Plasma Physics and Controlled Fusion* **48**, B83-B90 (2006).
91. C. Iaconis and I. A. Walmsley, Spectral phase interferometry for direct electric-field reconstruction of ultrashort optical pulses. *Opt. Lett.* **23**, 792-794 (1998).
92. F. Budde, *Experiment zur Erzeugung von Undulatorstrahlung mit laserbeschleunigten Elektronen*. Master thesis, Friedrich-Schiller-Universität Jena, 2007.

93. A. Buck, K. Zeil, A. Popp, K. Schmid, A. Jochmann, S. D. Kraft, B. Hidding, T. Kudyakov, C. M. S. Sears, L. Veisz, S. Karsch, J. Pawelke, R. Sauerbrey, T. Cowan, F. Krausz and U. Schramm, Absolute charge calibration of scintillating screens for relativistic electron detection. *Rev. Sci. Instr.* **81**, (2010).
94. M. Schnell, *Betatron radiation from a laser-plasma accelerator*. PhD thesis, Friedrich-Schiller-Universität Jena, 2014.
95. S. Semushin and V. Malka, High density gas jet nozzle design for laser target production. *Rev. Sci. Instr.* **72**, 2961-2965 (2001).
96. B. Landgraf, M. Schnell, A. Sävert, M. C. Kaluza and C. Spielmann, High resolution 3D gas-jet characterization. *Rev. Sci. Instr.* **82**, (2011).
97. B. Landgraf, *Charakterisierung von Überschalldüsen zur Elektronenbeschleunigung*. Master thesis, Friedrich-Schiller-Universität Jena, 2010.
98. A. Gopal, S. Minardi and M. Tatarakis, Quantitative two-dimensional shadowgraphic method for high-sensitivity density measurement of under-critical laser plasmas. *Opt. Lett.* **32**, 1238-1240 (2007).
99. R. Benattar, C. Popovics and R. Sigel, Polarized-Light Interferometer for Laser Fusion Studies. *Rev. Sci. Instr.* **50**, 1583-1585 (1979).
100. K. A. Nugent, Interferogram Analysis Using an Accurate Fully-Automatic Algorithm. *Applied Optics* **24**, 3101-3105 (1985).
101. P. Tomassini, A. Giulietti, L. A. Gizzi, M. Galimberti, D. Giulietti, M. Borghesi and O. Willi, Analyzing laser plasma interferograms with a continuous wavelet transform ridge extraction technique: the method. *Applied Optics* **40**, 6561-6568 (2001).
102. P. Tomassini and A. Giulietti, A generalization of Abel inversion to non-axisymmetric density distribution. *Opt. Commun.* **199**, 143-148 (2001).
103. P. Panigrahi and K. Muralidhar. Laser Schlieren and Shadowgraph. *Schlieren and Shadowgraph Methods in Heat and Mass Transfer*: Springer New York; 2012. pp. 23-46.
104. M. Reuter, *Interferometric Probing of Laser-Generated Plasmas for Electron Acceleration*. Master thesis, Friedrich-Schiller-Universität Jena, 2011.
105. M. B. Schwab, A. Sävert, O. Jäckel, J. Polz, M. Schnell, T. Rinck, L. Veisz, M. Möller, P. Hansinger, G. G. Paulus and M. C. Kaluza, Few-cycle optical probe-pulse for



- investigation of relativistic laser-plasma interactions. *Applied Physics Letters* **103**, 191118 (2013).
106. E. S. Sarachik and G. T. Schappert, Classical Theory of the Scattering of Intense Laser Radiation by Free Electrons. *Physical Review D* **1**, 2738-2753 (1970).
  107. T. Matsuoka, C. McGuffey, P. G. Cummings, Y. Horovitz, F. Dollar, V. Chvykov, G. Kalintchenko, P. Rousseau, V. Yanovsky, S. S. Bulanov, A. G. R. Thomas, A. Maksimchuk and K. Krushelnick, Stimulated Raman Side Scattering in Laser Wakefield Acceleration. *Phys. Rev. Lett.* **105**, 034801 (2010).
  108. A. G. R. Thomas, S. P. D. Mangles, Z. Najmudin, M. C. Kaluza, C. D. Murphy and K. Krushelnick, Measurements of wave-breaking radiation from a laser-wakefield accelerator. *Phys. Rev. Lett.* **98**, 054802 (2007).
  109. S. Wilks, T. Katsouleas, J. M. Dawson, P. Chen and J. J. Su, Beam Loading in Plasma-Waves. *IEEE Transactions on Plasma Science* **15**, 210-217 (1987).
  110. M. Tzoufras, W. Lu, F. S. Tsung, C. Huang, W. B. Mori, T. Katsouleas, J. Vieira, R. A. Fonseca and L. O. Silva, Beam loading by electrons in nonlinear plasma wakes. *Phys. Plasmas* **16**, 056705 (2009).
  111. C. Rechatin, J. Faure, X. Davoine, O. Lundh, J. Lim, A. Ben-Ismaïl, F. Burgy, A. Tafzi, A. Lifschitz, E. Lefebvre and V. Malka, Characterization of the beam loading effects in a laser plasma accelerator. *New Journal of Physics* **12**, 045023 (2010).
  112. G. Pretzler, A. Kasper and K. J. Witte, Angular chirp and tilted light pulses in CPA lasers. *Applied Physics B* **70**, 1-9 (2000).
  113. M. C. Kaluza, S. P. D. Mangles, A. G. R. Thomas, Z. Najmudin, A. E. Dangor, C. D. Murphy, J. L. Collier, E. J. Divall, P. S. Foster, C. J. Hooker, A. J. Langley, J. Smith and K. Krushelnick, Observation of a Long-Wavelength Hosing Modulation of a High-Intensity Laser Pulse in Underdense Plasma. *Phys. Rev. Lett.* **105**, 095003 (2010).
  114. A. Popp, J. Vieira, J. Osterhoff, Z. Major, R. Horlein, M. Fuchs, R. Weingartner, T. P. Rowlands-Rees, M. Marti, R. A. Fonseca, S. F. Martins, L. O. Silva, S. M. Hooker, F. Krausz, F. Gruner and S. Karsch, All-Optical Steering of Laser-Wakefield-Accelerated Electron Beams. *Phys. Rev. Lett.* **105**, 215001 (2010).
  115. S. Y. Kalmykov, L. M. Gorbunov, P. Mora and G. Shvets, Relativistic Extension of the Accelerating-Focusing Phase in 3D Nonlinear Laser Wake. *AIP Conference Proceedings* **877**, 735-742 (2006).

116. E. Siminos, S. Skupin, A. Sävert, J. M. Cole, S. P. D. Mangles and M. C. Kaluza, Modeling ultrafast shadowgraphy in laser-plasma interaction experiments. *Plasma Physics and Controlled Fusion*, accepted (2016).
117. G. Genoud, M. S. Bloom, J. Vieira, M. Burza, Z. Najmudin, A. Persson, L. O. Silva, K. Svensson, C. G. Wahlstrom and S. P. D. Mangles, Increasing energy coupling into plasma waves by tailoring the laser radial focal spot distribution in a laser wakefield accelerator. *Phys. Plasmas* **20**, 064501 (2013).
118. S. Bulanov, N. Naumova, F. Pegoraro and J. Sakai, Particle injection into the wave acceleration phase due to nonlinear wake wave breaking. *Physical Review E* **58**, R5257 (1998).
119. S. Banerjee, N. D. Powers, V. Ramanathan, I. Ghebregziabher, K. J. Brown, C. M. Maharjan, S. Chen, A. Beck, E. Lefebvre, S. Y. Kalmykov, B. A. Shadwick and D. P. Umstadter, Generation of tunable, 100-800 MeV quasi-monoenergetic electron beams from a laser-wakefield accelerator in the blowout regime. *Phys. Plasmas* **19**, 056703 (2012).
120. A. Pak, K. A. Marsh, S. F. Martins, W. Lu, W. B. Mori and C. Joshi, Injection and Trapping of Tunnel-Ionized Electrons into Laser-Produced Wakes. *Phys. Rev. Lett.* **104**, 025003 (2010).
121. C. McGuffey, A. G. R. Thomas, W. Schumaker, T. Matsuoka, V. Chvykov, F. J. Dollar, G. Kalintchenko, V. Yanovsky, A. Maksimchuk, K. Krushelnick, V. Y. Bychenkov, I. V. Glazyrin and A. V. Karpeev, Ionization Induced Trapping in a Laser Wakefield Accelerator. *Phys. Rev. Lett.* **104**, 025004 (2010).
122. G. L. Yudin and M. Y. Ivanov, Nonadiabatic tunnel ionization: Looking inside a laser cycle. *Phys. Rev. A* **64**, 013409 (2001).
123. D. Ullman, *Optical Diagnostics for LWFA Experiments*. Master thesis, Friedrich-Schiller-Universität Jena, 2015.
124. D. W. Forslund, J. M. Kindel, W. B. Mori, C. Joshi and J. M. Dawson, Two-Dimensional Simulations of Single-Frequency and Beat-Wave Laser-Plasma Heating. *Phys. Rev. Lett.* **54**, 558-561 (1985).
125. K. C. Tzeng and W. B. Mori, Suppression of Electron Ponderomotive Blowout and Relativistic Self-Focusing by the Occurrence of Raman Scattering and Plasma Heating. *Phys. Rev. Lett.* **81**, 104-107 (1998).
126. D. Polli, D. Brida, S. Mukamel, G. Lanzani and G. Cerullo, Effective temporal resolution in pump-probe spectroscopy with strongly chirped pulses. *Phys. Rev. A* **82**, 053809 (2010).

127. NakagawaK, IwasakiA, OishiY, HorisakiR, TsukamotoA, NakamuraA, HirosawaK, LiaoH, UshidaT, GodaK, KannariF and SakumaI, Sequentially timed all-optical mapping photography (STAMP). *Nat Photon* **8**, 695-700 (2014).
128. D. Brida, C. Manzoni, G. Cirimi, M. Marangoni, S. Bonora, P. Villoresi, S. D. Silvestri and G. Cerullo, Few-optical-cycle pulses tunable from the visible to the mid-infrared by optical parametric amplifiers. *Journal of Optics* **12**, 013001 (2010).
129. M. Hemmer, M. Baudisch, A. Thai, A. Couairon and J. Biegert, Self-compression to sub-3-cycle duration of mid-infrared optical pulses in dielectrics. *Optics Express* **21**, 28095-28102 (2013).
130. M. C. Kaluza, H. P. Schlenvoigt, S. P. D. Mangles, A. G. R. Thomas, A. E. Dangor, H. Schwoerer, W. B. Mori, Z. Najmudin and K. M. Krushelnick, Measurement of Magnetic-Field Structures in a Laser-Wakefield Accelerator. *Phys. Rev. Lett.* **105**, (2010).
131. C. Ma, X. Xu, Y. Liu and L. V. Wang, Time-reversed adapted-perturbation (TRAP) optical focusing onto dynamic objects inside scattering media. *Nat Photon* **8**, 931-936 (2014).
132. J. Garcia-Sucerquia, W. B. Xu, S. K. Jericho, P. Klages, M. H. Jericho and H. J. Kreuzer, Digital in-line holographic microscopy. *Applied Optics* **45**, 836-850 (2006).

## Publications by the Author

(Articles are listed in reverse order of appearance.)

E. Siminos, S. Skupin, A. Sävert, J. M. Cole, S. P. D. Mangles and M. C. Kaluza. "Modeling ultrafast shadowgraphy in laser-plasma interaction experiments". *Plasma Physics and Controlled Fusion*, **58** 065004 (2016).

S. Keppler, A. Sävert, J. Körner, M. Hornung, H. Liebetrau, J. Hein and M. C. Kaluza. "The generation of amplified spontaneous emission in high-power CPA laser systems". *Laser & Photonics Reviews* **10**, 264-277 (2016).

M. Yeung, J. Bierbach, E. Eckner, S. Rykovanov, S. Kuschel, A. Sävert, M. Forster, C. Rödel, G. G. Paulus, S. Cousens, M. Coughlan, B. Dromey and M. Zepf. "Noncollinear Polarization Gating of Attosecond Pulse Trains in the Relativistic Regime". *Phys. Rev. Lett.* **115**, 193903 (2015).

A. Sävert, S. P. D. Mangles, M. Schnell, E. Siminos, J. M. Cole, M. Leier, M. Reuter, M. B. Schwab, M. Möller, K. Poder, O. Jäckel, G. G. Paulus, C. Spielmann, S. Skupin, Z. Najmudin and M. C. Kaluza. "Direct Observation of the Injection Dynamics of a Laser Wakefield Accelerator Using Few-Femtosecond Shadowgraphy". *Phys. Rev. Lett.* **115**, 055002 (2015).

C. Widmann, V. Afonso Rodríguez, A. Bernhard, M. C. Kaluza, S. Kuschel, A.-S. Müller, M. Nicolai, R. Rossmanith, M. B. Schwab, A. Sävert and W. Werner. "First Tests of a Beam Transport System from a Laser Wakefield Accelerator to a Transverse Gradient Undulator". *Proceedings of IPAC2015*, 216 (2015).

M. Schnell, A. Sävert, I. Uschmann, O. Jansen, M. C. Kaluza and C. Spielmann. "Characterization and application of hard x-ray betatron radiation generated by relativistic electrons from a laser-wakefield accelerator". *Journal of Plasma Physics* **81**, (2015).

M. Oppelt, M. Baumann, R. Bergmann, E. Beyreuther, K. Brüchner, J. Hartmann, L. Karsch, M. Krause, L. Laschinsky, E. Leßmann, M. Nicolai, M. Reuter, C. Richter, A. Sävert, M. Schnell, M. Schürer, J. Woithe, M. Kaluza and J. Pawelke. "Comparison study of in vivo dose response to laser-driven versus conventional electron beam". *Radiation and Environmental Biophysics*, 1-12 (2015).

A. Kessler, M. Hornung, S. Keppler, F. Schorcht, M. Hellwing, H. Liebetrau, J. Koerner, A. Sävert, M. Siebold, M. Schnepf, J. Hein and M. C. Kaluza. "16.6 J chirped femtosecond laser pulses from a diode-pumped Yb:CaF<sub>2</sub> amplifier". *Opt. Lett.* **39**, 1333-1336 (2014).

S. Keppler, M. Hornung, R. Bödefeld, A. Sävert, H. Liebetrau, J. Hein and M. C. Kaluza. "Full characterization of the amplified spontaneous emission from a diode-pumped high-power laser system". *Optics Express* **22**, 11228-11235 (2014).

M. Nicolai, A. Sävert, M. Reuter, M. Schnell, J. Polz, O. Jäckel, L. Karsch, M. Schurer, M. Oppelt, J. Pawelke and M. C. Kaluza. "Realizing a laser-driven electron source applicable for radiobiological tumor irradiation". *Appl. Phys. B* **116**, 643-651 (2014).

M. Hornung, S. Keppler, R. Bödefeld, A. Kessler, H. Liebetrau, J. Körner, M. Hellwing, F. Schorcht, O. Jäckel, A. Sävert, J. Polz, A. K. Arunachalam, J. Hein and M. C. Kaluza. "High-intensity, high-contrast laser pulses generated from the fully diode-pumped Yb:glass laser system POLARIS". *Opt. Lett.* **38**, 718-720 (2013).

M. Schnell, A. Sävert, I. Uschmann, M. Reuter, M. Nicolai, T. Kämpfer, B. Landgraf, O. Jäckel, O. Jansen, A. Pukhov, M. C. Kaluza and C. Spielmann. "Optical control of hard X-ray polarization by electron injection in a laser wakefield accelerator". *Nature Commun.* **4**, 2421 (2013).

M. B. Schwab, A. Sävert, O. Jäckel, J. Polz, M. Schnell, T. Rinck, L. Veisz, M. Möller, P. Hansinger, G. G. Paulus and M. C. Kaluza. "Few-cycle optical probe-pulse for investigation of relativistic laser-plasma interactions". *Applied Physics Letters* **103**, 191118 (2013).

M. Schürer, M. Baumann, E. Beyreuther, K. Bruechner, W. Enghardt, M. Kaluza, L. Karsch, L. Laschinsky, E. Lessmann, M. Nicolai, M. Oppelt, M. Reuter, C. Richter, A. Sävert, M. Schnell, J. Woithe and J. Pawelke. "Irradiation system for pre-clinical studies with laser accelerated electrons". *Biomedical Engineering-Biomedizinische Technik* **57**, (2012).

M. Schnell, A. Sävert, B. Landgraf, M. Reuter, M. Nicolai, O. Jäckel, C. Peth, T. Thiele, O. Jansen, A. Pukhov, O. Willi, M. C. Kaluza and C. Spielmann. "Deducing the electron-beam diameter in a laser-plasma accelerator using x-ray betatron radiation". *Phys. Rev. Lett.* **108**, 075001 (2012).

S. Keppler, R. Bödefeld, M. Hornung, A. Sävert, J. Hein and M. C. Kaluza. "Prepulse suppression in a multi-10-TW diode-pumped Yb:glass laser". *Appl. Phys. B* **104**, 11-16 (2011).

B. Landgraf, M. Schnell, A. Sävert, M. C. Kaluza and C. Spielmann. "High resolution 3D gas-jet characterization". *Rev. Sci. Instr.* **82**, (2011).

A. Buck, M. Nicolai, K. Schmid, C. M. S. Sears, A. Sävert, J. M. Mikhailova, F. Krausz, M. C. Kaluza and L. Veisz. "Real-time observation of laser-driven electron acceleration". *Nature Phys.* **7**, 543-548 (2011).

M. Hornung, R. Bödefeld, M. Siebold, A. Kessler, M. Schnepf, R. Wachs, A. Sävert, S. Podleska, S. Keppler, J. Hein and M. C. Kaluza. "Temporal pulse control of a multi-10 TW diode-pumped Yb:Glass laser". *Appl. Phys. B* **101**, 93-102 (2010).

C. Bellei, S. R. Nagel, S. Kar, A. Henig, S. Kneip, C. Palmer, A. Sävert, L. Willingale, D. Carroll, B. Dromey, J. S. Green, K. Markey, P. Simpson, R. J. Clarke, H. Lowe, D. Neely, C. Spindloe, M. Tolley, M. C. Kaluza, S. P. D. Mangles, P. McKenna, P. A. Norreys, J. Schreiber, M. Zepf, J. R. Davies, K. Krushelnick and Z. Najmudin. "Micron-scale fast electron filaments and recirculation determined from rear-side optical emission in high-intensity laser-solid interactions". *New Journal of Physics* **12**, (2010).

## Nomenclature

### Fundamental Constants

Symbol	Name	Quantity
$c$	Speed of light	299792458 m/s
$h$	Planck constant	$6.626 \cdot 10^{-34}$ J/s
$e$	Electron charge	$1.602 \cdot 10^{-19}$ C
$\epsilon_0$	Permittivity of free space	$8.854 \cdot 10^{-12}$ F/m
$m_e$	Electron rest mass	$9.109 \cdot 10^{-31}$ kg
$k_B$	Boltzmann factor	$1.381 \cdot 10^{-23}$ J/K

### Basic Symbols

Symbol	Name
$\mathbf{E}$	Electric field vector
$\mathbf{B}$	Magnetic field vector
$\mathbf{A}$	Vector potential
$\phi$	Scalar potential
$\mathbf{p}$	Momentum
$t$	Time
$r$	Spatial coordinate used in axial symmetry
$\mathbf{e}$	Unity vector
$\mathbf{v}$	Velocity vector
$\mathbf{F}$	Force vector
$\mathbf{k}$	Wave vector
$a_0$	Normalized vector potential
$\omega$	Angular frequency
$\lambda$	Wavelength
$E$	Energy
$I_L$	Laser intensity
$P$	Power
$\gamma$	Relativistic gamma factor
$n_e$	Density of the electrons
$T_e$	Electron temperature
$T_i$	Ion temperature
$\eta$	Refractive index
$f$	Focal length
$v_g$	Group velocity
$v_\phi$	Phase velocity
$w_0$	Laser spot size

# Appendix A

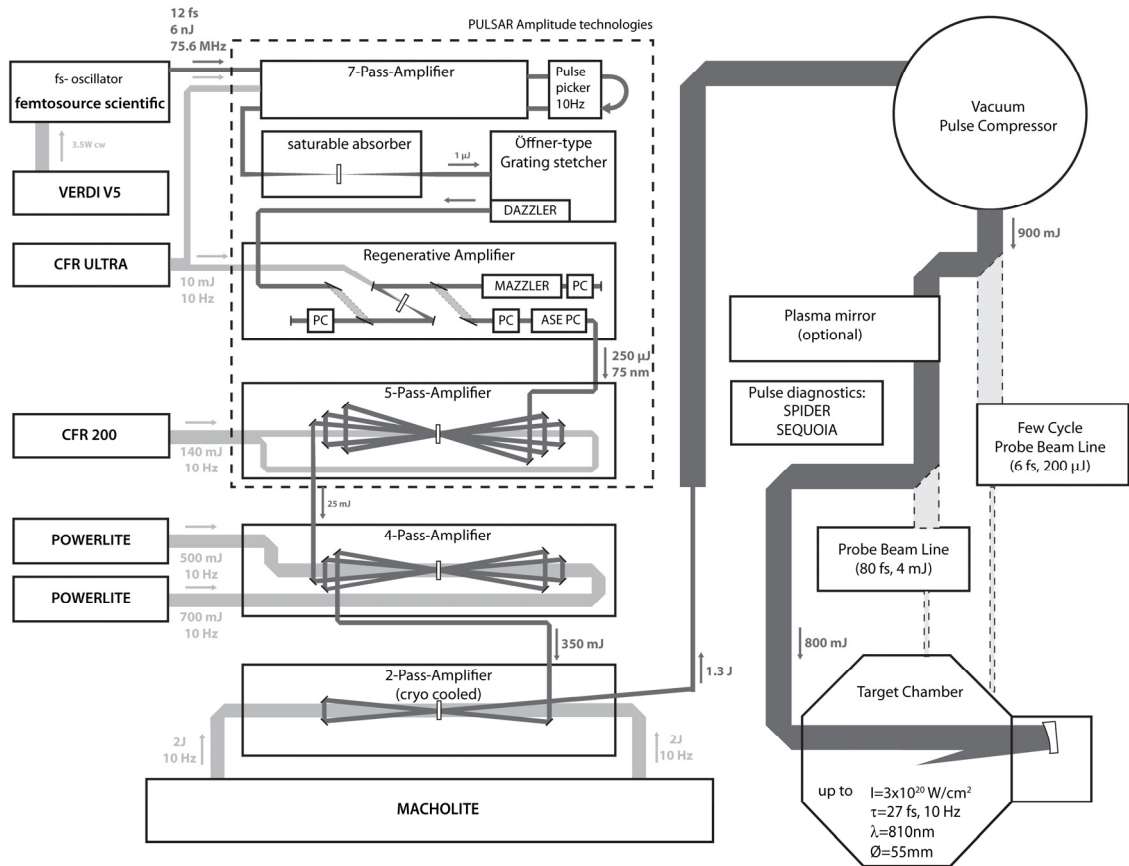
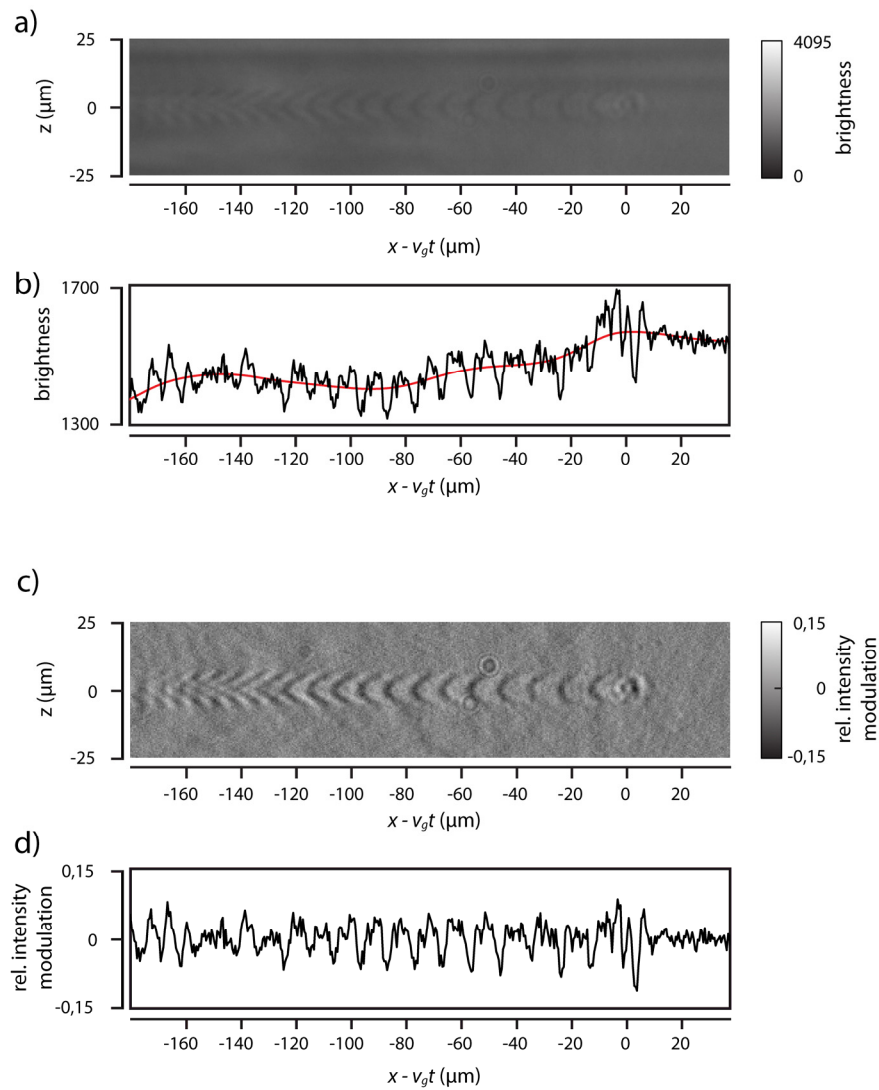


Figure A | JETi 40: The Jena Ti:sapphire laser system.



## Appendix B



**Figure B | Image post processing of the shadowgrams.** a) Raw data,  $I$ , from the CCD. b) Profile of a) along  $y = 0$  (black line) and low order spline fit  $I_0$  (red line). This was done for every horizontal line in the image. c) Calculation of the relative intensity modulation  $I_{norm} = (I - I_0)/I_0$ . d) Profile of c) along  $y = 0$ .

## Appendix C

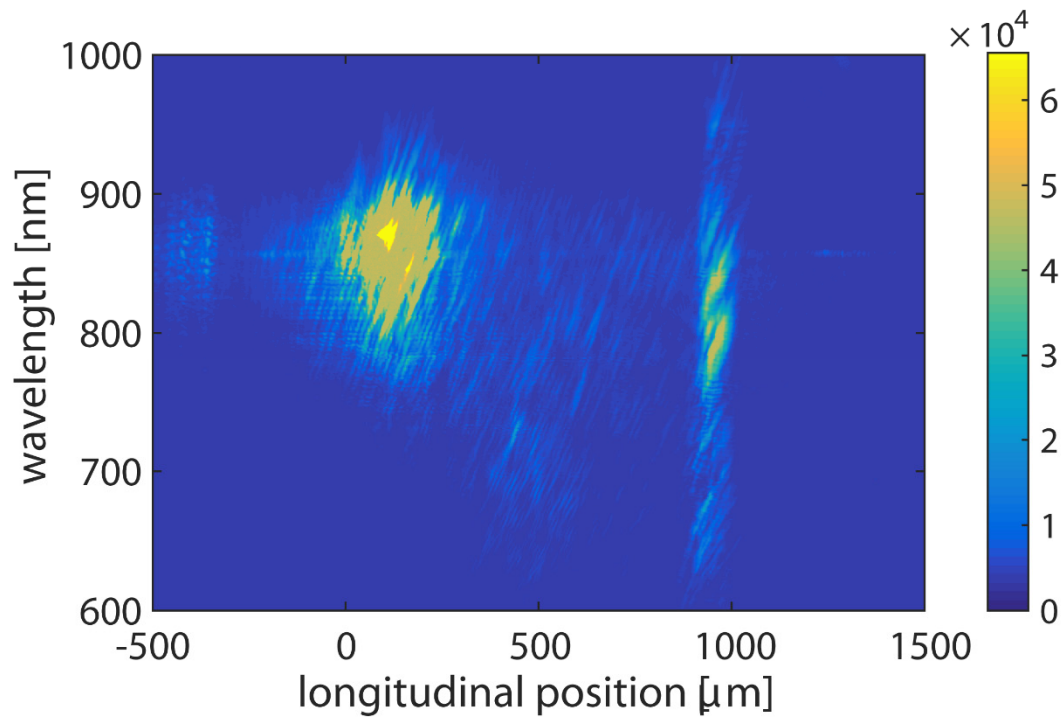


**Figure C | Scattered pump light and self-emission from the plasma along the propagation axis taken with an imaging spectrometer.** The laser propagates from left to right. The longitudinal position is referenced to the one in Chapter 4. (image courtesy of Kristjan Poder)

# Danksagung

Für das Gelingen dieser Doktorarbeit möchte ich mich bei allen beteiligten Kollegen und Mitarbeitern des Instituts für Optik und Quantenelektronik und des Helmholtz-Instituts Jena bedanken. Insbesondere seien nachfolgende Personen besonders hervorgehoben

Mein Betreuer Prof. Malte Kaluza der mir die Welt der Plasmabeschleunigung eröffnet hat und mich während der gesamten Zeit unterstützt hat. Seine Begeisterungsfähigkeit und Offenheit neue, riskante Sachen auszuprobieren und sein uneingeschränktes Vertrauen in mich auch während etwas schwierigeren Zeiten haben entscheidend zu den Ergebnissen beigetragen. Dabei waren aber auch seine Erfahrung und kritischer Blick auf waghalsige Theorien meinerseits sehr hilfreich und haben entscheidend zu einem umfassenden physikalischen Verständnis beigetragen.

Meinem langjährigen Kollegen Michael Schnell und seiner Ruhe und Besonnenheit aber auch Tatkraft im Labor bis früh in die Morgenstunden hinein. Damit waren die anspruchsvollen Experimente erst möglich. Vielen Dank für eine schöne Zeit am Institut und die Gespräche bei unserer Mittagsrunde abseits der Wissenschaft über die ganz alltäglichen Herausforderungen im Leben.

Meinen Kollegen Jens Polz, Matthew B. Schwab und Oliver Jäckel, die die waghalsige Idee einen few-cycle Probestrahl am JETi Laser einzubauen mit ins Leben riefen und diese dann auch umsetzten. Peter Hansinger und Max Möller, die mir gezeigt haben wie man few-cycle Pulse ganz selbstverständlich erzeugen kann und diese charakterisiert.

Stefan Skupin und insbesondere Evangelos Siminos, die dazu beigetragen haben, die unerwartet hohe Qualität der Schattenbilder zu erklären und intuitiven Vermutungen zu bestätigen. Es hat lange gebraucht bis wir zu der Einsicht kamen, dass nur eine 3D Simulationen mit eingebauten Probepuls und Abbildung alle beobachteten Strukturen und Effekte erklären kann.

Stuart P.D. Mangles und Zulfikar Najmudin, die an unzähligen Diskussionen zur Prägung unseres Verständnisses der Schattenbilder beteiligt waren. Sie haben sich dabei nicht einfach nur von deren Schönheit blenden lassen, sondern waren insbesondere an der Physik dahinter interessiert. Weiterhin Jason M. Cole und Kristjan Poder, die in nachfolgenden Kampagnen unser Verständnis verfeinert haben und mit Simulationen unterstützten.

Der Deutsche Forschungs Gemeinschaft (SFB TR18) und dem BMBF für die finanzielle Unterstützung der Doktorarbeit und die hervorragende Rahmenbedingungen auf nationaler wie auch auf internationaler Ebene um einen Austausch mit anderen Kollegen zu ermöglichen.

Burgard Beleites und Falk Ronneberger für den Betrieb des JETi Lasers aber auch Oliver Jäckel der in einer turbulenten Zeit dafür gesorgt hat, dass einen funktionierender Laser auch nach Feierabend zu Verfügung zu stand. Zusammen haben sie es geschafft den Laser mit Ruhe und Gelassenheit zu optimieren auch wenn von den Experimentatoren nur „Geht nicht!“ kommt. Weiterhin Wolfgang Ziegler der durch seine langjährige Erfahrung, Kreativität und Detailtreue die experimentellen Aufbauten entworfen und fertigen lassen hat.

Maria Leier, Maria Reuter, als langjährige tolerante Bürokollegen sowie Jens Polz; für die Zusammenarbeit, Unterstützung im Labor und bei der Durchführung der langen Experimentierkampagnen und darüber hinaus.

László Veisz für den entscheidenden Hinweise um den Probestrahl auch bei hohen Laserenergien erfolgreich einzusetzen. Gleichzeitig aber auch für die Möglichkeit am LWS20 am MPQ in Garching zusammen mit Maria Leier, Alexander Buck, Chris M.S. Sears, Karl Schmid eine aufregende Kampagne durchzuführen und einen ersten Einblick in die Welt der Plasmawellen zu erhalten.

Alec G.R. Thomas und Zhaohan He für erste Simulationen um dem Unterschied zwischen Helium und Wasserstoff auf die Spur zu kommen und einen Einblick in die Feinheiten von PIC Simulationen zu erhalten.

Paolo Tomassini für die Einführung in die Welt der Wavelet Analyse und der automatisierten Auswertung von Interferogrammen.

Joachim Hein, Marco Hornung, Sebastian Keppler, Alexander Kessler sowie auch allen anderen Kollegen aus meiner Arbeitsgruppe. Sie haben entscheidend zu meinem Wissen über Laser und Verstärker beigetragen. Erst durch die Wechselseitige Diskussion zwischen Laserentwicklern und Experimentatoren und die Neugierde einfach mal Sachen auszuprobieren war es möglich den POLARIS Laser in den Experimentiermodus zu bringen. Das gesamte Wissen konnte in gleichen Maße auch für den JETi40 genutzt werden

und hat ihn damit entscheidend verbessert.

Ragnar Bödefeld für die vielen wissenschaftlichen aber auch gesellschaftlichen Themen und Diskussionen ohne Zeitlimit.

Stephan Kuschel für die vielen anregenden physikalischen Diskussion und ebenso Christian Rödel für kontroverse, ausschweifende Diskussionen ohne Tabus auch abseits der Physik.

Prof. Matt Zepf für sein tiefes wissenschaftliches Grundverständnis und die Gabe, augenscheinlich komplizierte Sachverhalte herunter zu brechen und anschaulich zu erklären.

Den Werkstätten des IOQ, die auch nach Feierabend dringend benötigte Teile schnell und unbürokratisch gefertigt haben und so ebenfalls am Gelingen der Experimente beteiligt waren.

Matthew B. Schwab für das Korrekturlesen der vorliegenden Arbeit.

Insbesondere gilt mein Dank aber meiner Familie, der diese Arbeit gewidmet ist.

Meiner Mutter Heidrun Sävert, die mir das Studium ermöglicht hat und mich dabei bedingungslos unterstützt hat und ebenso auch meiner Schwester Antje.

Meiner Frau Maria und unseren beiden Kindern Finn und Mathilda. Ihr seid der Sonnenschein in meinem Leben und Quelle meiner Motivation. Ohne Euch hätte ich die Arbeit nicht geschafft.

## **Ehrenwörtliche Erklärung**

Ich erkläre hiermit ehrenwörtlich, dass ich die vorliegende Arbeit selbstständig und ohne unzulässige Hilfe Dritter und ohne Benutzung anderer als der angegebenen Hilfsmittel und Literatur angefertigt habe.

Die aus anderen Quellen direkt oder indirekt übernommenen Daten und Konzepte sind unter Angabe der Quelle gekennzeichnet. Weitere Personen waren nicht an der inhaltlichen-materiellen Erstellung der vorliegenden Arbeit beteiligt.

Insbesondere habe ich hierfür nicht die entgeltliche Hilfe von Vermittlungs- bzw. Beratungsdiensten (Promotionberater oder andere Personen) in Anspruch genommen. Niemand hat von mir unmittelbar oder mittelbar geldwerte Leistungen für die Arbeiten erhalten, die im Zusammenhang mit dem Inhalt der vorgelegten Dissertation stehen.

Die Arbeit wurde bisher weder im In- noch im Ausland in gleicher oder ähnlicher Form einer anderen Prüfungsbehörde vorgelegt. Die geltende Promotionsordnung der Physikalisch-Astronomischen Fakultät ist mir bekannt.

Ich versichere ehrenwörtlich, dass ich nach bestem Wissen die reine Wahrheit gesagt und nichts verschwiegen habe.

Jena, den 05.09.2016

Alexander Sävert